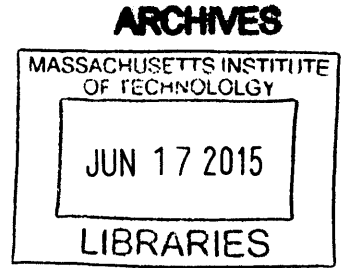# Materials Physics for Thermoelectric and Related Energetic Applications

By

Shuang Tang

S. M., Materials Science and Engineering (2012)
Massachusetts Institute of Technology

B. S., Physics (2009)
Fudan University, Shanghai, China

Submitted to the Department of Materials Science and Engineering
in Partial Fulfillment of the Requirements for the Degree of
Doctor of Philosophy in Materials Science and Engineering

at the
Massachusetts Institute of Technology
June 2015

Signature redacted

Signature of Author...
Department of Materials Science and Engineering

Signature redacted

Certified by...
Mildred S. Dresselhaus
Institute Professor
Signature redactedThesis Advisor

Accepted by...
Donald Sadoway
Chairman, Department Committee on Graduate Students

1

Materials Physics for Thermoelectric and Related Energetic Applications

By

Shuang Tang

Abstract

Thermoelectrics study the direct inter-conversion between heat flow and electrical power, which has a wide range of applications including power generation and refrigeration. The performance of thermoelectricity generation and the refrigeration is characterized by a dimensionless number called the Figure-of-Merit (ZT), defined as $ZT = \sigma S^2 T / \kappa$, where σ is the electrical conductivity, κ is the thermal conductivity, S is the Seebeck coefficient, and T is the absolute temperature. Before 1993, the upper-limit of ZT was barely 1. After the efforts of more than twenty years, the upper-limit of ZT has been pushed up to ~2. However, for the thermoelectric technology to be commercially attractive, the value of ZT and the cost of production have to be further improved.

Most of the ZT enhancing strategies that have been proposed since 1993 involve the changing and the controlling of the dimension of materials systems, the scattering mechanism(s) of carriers, the shape of the electronic band structure and the density of states, and the magnitude of the band gap. As further research is carried out, it is found that these strategies do not always work to enhance ZT. Even for a working materials system, the improvement margin of increasing ZT can be small. The balancing between σ and S^2 / κ has significantly limited the improvement margin for our ZT enhancing goal. Therefore, we have two problems to explore: (1) how can we deal with the strong correlation between σ and S^2 / κ, when trying to enhance ZT, and (2) how can we make the above mentioned strategies more convergent as we change the dimension of materials systems, the scattering mechanism(s) of carriers, the shape of electronic band structure, and the magnitude of the band gap?

This thesis aims to explore the solutions to these two major problems at the research frontier of thermoelectric ZT enhancement. The first problem is discussed by providing a new framework of pseudo-ZTs, where the electronic contribution (zt_e) and the lattice contribution (zt_L) to the overall ZT can be treated in a relatively separate manner. The second problem is discussed under this new framework of pseudo-ZTs, through four subsections: (i) scattering and system dimension; (ii) band structure; (iii) density of states; (iv) band gap.

The one-to-one correspondence relation between the carrier scattering mechanism(s) and the maximum Seebeck coefficient is further studied. A new tool for scattering mechanism(s) inference and for the Seebeck coefficient enhancement is provided. For the band structure and the band gap part, advanced band engineering methods are provided to study nanostructured narrow-gap materials, the Dirac cone materials, and the anisotropic materials, which are historically found to be good thermoelectric materials.

To further demonstrate the newly developed theories, this thesis has also illustrated the application of these models in some specific materials systems, including the graphene system, the transition metal dichalcogenides monolayer materials systems, the $Bi_{1-x}Sb_x$ alloys system, the $In_{1-x}Ga_xN$ alloys system, and the $(Bi_{1-y}Sb_y)_2(S_{1-x}Te_x)_3$ alloys system.

Thesis Supervisor: Mildred S. Dresselhaus
Title: Institute Professor of Electrical Engineering and Physics

Table of Contents

Acknowledgements

I came to MIT for the PhD program in 2009. Through all my years here, I have been struggled a lot. I thank my advisor Prof. Mildred Dressselhaus for taking me as a student. Working on thermoelectrics here with Millie is not an easy thing, and I have made it through under the help from many people. Every single person and every single moment during these years are meaningful and important for my life-long journey on this planet.

I thank the flexibility and independence that Millie has given to me for all my PhD years in her group, which has provides me with the chance to conceive research ideas, solve problems, find resources, write manuscripts and make publications by my own hands. These experiences have well equipped me for my future career and life.

I thank all the instructors of courses both in my undergraduate school and in my graduate school. The knowledge and skills I have learned in these courses from these instructors well prepared me for my PhD research. With very limited resource of equipment, I managed to make progress and publications just by pencils and scratch papers. I could not have done this without the education and training I obtained from my undergraduate and graduate years.

I also thank Dr. Harold Weinstock from the Air Force Office of Scientific Research, Prof. Joseph Heremans from the Ohio State University, Prof. Elena Rogacheva from the National Technical University "Kharkov Polytechnic Institute," and Prof. Gang Chen from the Mechanical Engineering Department of MIT for the funding management and collaborations with my advisor Prof. Mildred Dresselhaus and me, so that I could have enough funding support for my tuition and stipend to finish the PhD research here with Millie.

I thank Prof. Jeffrey Grossman, Prof. Silvija Gradecak, Prof. Jean-Paul Issi, Prof. Jean-Christopher Charlier, Prof. Donald Sadoway, Prof. Cyril Opeil, Dr. Albert Liao, Prof. Jianfang Wang, Prof. Jing Kong, Dr. Yu-Ming Lin, Prof. Oded Rabin, Prof. Qing Hao, Prof. Na Lu, Prof. Sheng Shen, Prof. Tengfei Luo, Prof. Chuang Deng, Prof. Shuo Chen, Dr. Thomas Hirschmann, Dr. Paulo Antonio Trindade Araujo, Prof. David Hsieh, and Prof. Liang Fu for the strong supports and the valuable discussions.

I also thank Dr. Yu Albert Bai and Mr. Minyue Charles Wang for the mental and life support of my PhD years.

This thesis is also to memorize my respective mentor Prof. Jiyao Chen who passed away in 2014.

Most importantly, I thank my parents and all my family members who have been giving me endless love and support all these years.

List of Figures

List of Tables

Chapter 1

Introduction

The energy crisis is an urgent issue on a global scope, economically, politically, environmentally, and scientifically. The essence of the energy issue is how to sustainably power our planet at the present and in the future, without introduction further severe damage to the natural environment and human society. The human society has been powered by the fossil energy from ancient time, including coal, natural gas, and oil. Even up to now, the contemporary industry still relies 86.4% on fossil energy. On the one hand, the fossil deposit will be run out sooner or later. On the other hand, the combustion of fossil fuels is releasing 34,000,000,000 tonnes of carbon dioxides [1], among other harmful gas pollutants, per year, causing irreversible environmental changes. Since it now seems impossible to stop consuming fossil fuels, thereby shutting down the 86.4% of the industry [2] and putting the human society back into darkness, an efficient approach is needed to enhance the energy usage efficiency that is compatible with both traditional and new energy generation approaches. Thermoelectrics is one of the most promising technologies that can keep in such a task [3-6].

Thermoelectrics is the subject that studies the inter-conversion between heat flow and electricity, which involves two aspects: power generation and refrigeration/cooling [7, 8]. When a thermoelectric system is exposed to a temperature gradient, a built-in voltage will be established between the hot side and the cold side, which results in usable electric power generation when connected to an external circuit. Oppositely, if a thermoelectric system is connected to an external power supply, heat flow will be generated by consuming the electricity energy, which results in refrigeration/cooling.

In traditional heat engine systems, about 70% of the energy is lost as waste heat to the environment on average. An estimated 1500-3000 trillion BTU/year of waste heat from industrial processes remain unrecovered in the United States [9]. In recent years, thermoelectric power generation has had renewed interest to partially convert this waste heat into electricity. Thermoelectric power generators have been developed to produce electricity from the waste heat in car exhaust gas [10], or from solar-radiation [9] heat as a cheap alternative to solar cells. Thermoelectric technology can be implemented for almost all thermal processes, such as combustion furnaces [10], vehicle and air craft engines [9], thermal fluids [11], nuclear reactors [12], and various sorts of factories [13], which will all play an important role in waste heat recovery. Under some special circumstances, high-temperature thermoelectric power generators provide an effective choice, e.g. for the nuclear reactors in space craft and in deep ocean submarines [12].

Thermoelectric refrigeration and cooling use solid state materials as media. With many attractive features such as low noise, compact size, easy installation and transport, low cost and low pollution, thermoelectric cooling become one of the most suitable approaches for electronic cooling, laser cooling, medical cooling, and temperature controlled clothing. Products for portable cooling in niche markets have already been put into commercial use, including USB beer/cola coolers, car-seat coolers [14, 15], and polymerase chain reaction instruments for DNA pieces amplification [16].

1.1 Thermoelectrics

To make a closed circuit, a thermoelectric device must have at least two legs, which are formed by P-type and N-type thermoelectric materials, respectively, as shown in Figure (1.1a). In the thermoelectric power generation device, the charge carriers at the hot side tend to have higher kinetic energy than the charge carriers at the cold side, which results in a net carrier flow. This

15

charge flow will be balanced by the built-in voltage [17]. The magnitude of the built-in voltage is proportional to the temperature gradient, as shown in Equation (1.1),

$$\Delta V = S\Delta T \tag{1.1}$$

where S is called the Seebeck coefficient, named after the Baltic German physicist Thomas Johann Seebeck. Macroscopically, the Seebeck coefficient means the induced thermoelectric voltage per unit temperature difference, which is also called the thermopower. Microscopically, the Seebeck coefficient means the entropy carried per unit charge during the transport process, which will be further explained by the Boltzmann Equations in Chapter 2.
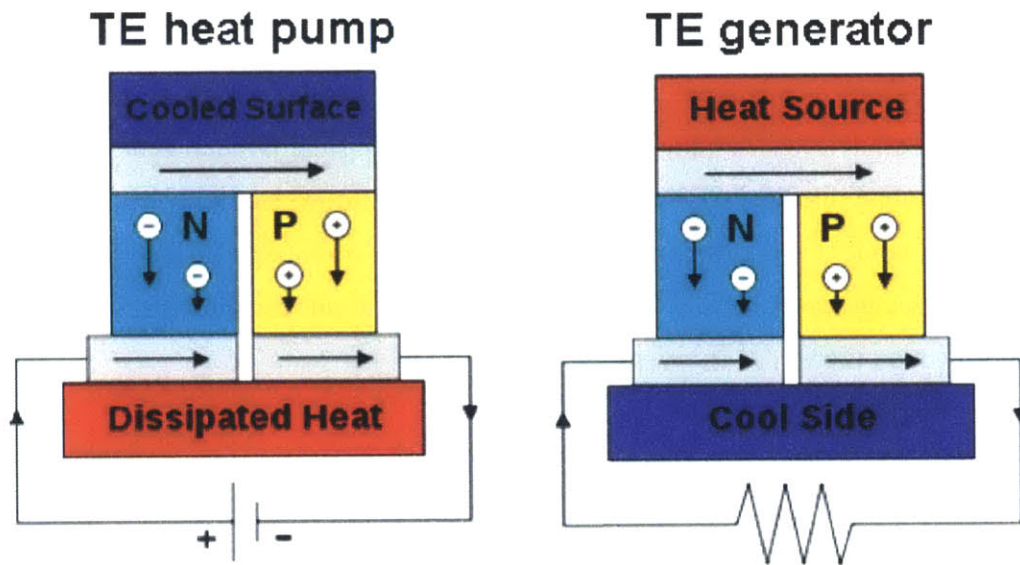
Figure 1.1: Scheme of **(a)** a thermoelectric power generation device and **(b)** a thermoelectric cooling device. The electrons and holes are indicated by the negative charge and positive charge signs. The arrow indicates the direction of current flow within the circuit. The P-type leg and the N-type leg are indicated and marked out in such P-N junction structures.

A thermoelectric cooling device also needs at least two legs for P-type and N-type thermoelectric materials, as shown in Figure (1.1 b). This P-N junction will work as a heat sink to perform the heat pumping task. The heat pumping rate is proportional to the electrical current flowing in the junction, as shown in Equation (1.2),

$$r = \left(\Pi_P - \Pi_N \right) I_{current} \tag{1.2}$$

where r is the heat pumped per unit time, $I_{current}$ is the electrical current, and Π_P and Π_N are the Peltier coefficients for the P-type and N-type legs, respectively, named after the French physicist Jean Charles Athanase Peltier. This phenomenon is called the Peltier effect. The Peltier effect can be seen as the reverse counterpart of the Seebeck effect. Thus, the Seebeck coefficient and the Peltier coefficient for a specific material can be related by Equation (1.3).

$$\Pi = TS \tag{1.3}$$

Further, the Seebeck coefficient of this specific material can usually vary as a function of temperature, which is called the Thomson effect.

1.2 Figure of Merit

The performance of a thermoelectric device, or of a specific thermoelectric material is characterized by a dimensionless number named the Figure-of-Merit (ZT), as defined in Equation (1.4) [17],

$$ZT = \frac{\sigma S^2 T}{\kappa} \tag{1.4}$$

where σ is the electrical conductivity, κ is the thermal conductivity, S is the Seebeck coefficient, and T is the absolute temperature. This definition could be understood intuitively. To have the thermoelectric device work more efficiently, we will prefer it to conduct more electricity, and to induce larger voltage, while to conduct less heat to keep the temperature gradient and thermal potential. The relation between the ZT and the power generation efficiency (ξ) of a thermoelectric system is shown in Equation (1.5),

$$\xi = \frac{T_{Hot} - T_{Cold}}{T_{Hot}} \frac{\sqrt{1+ZT}-1}{\sqrt{1+ZT}+\dfrac{T_{Cold}}{T_{Hot}}} \tag{1.5}$$

where T_{Hot} and T_{Cold} stand for the hot-side and cold-side temperatures, respectively. Further, σS^2 characterizes the power density per unit time of this energy conversion device, and is, therefore, called the power factor.

1.3 Scope and Organization of this Thesis

This thesis is organized in the way of providing solutions to the two major problems in the frontier research of thermoelectric ZT enhancement: (1) How can we conquer the strong correlation between electrical conductivity (σ), thermal conductivity (κ) and the Seebeck coefficient (S)? (2) Why have the strategies previously used by researchers regarding changing the system dimensions, the carrier scattering mechanism(s), the electronic band structure, the electronic density of states, and the energy band gap, sometimes worked but sometimes they do not work?

The first problem is discussed in this thesis work by providing a new framework of pseudo-ZTs, where the electronic contribution and the lattice contribution to ZT can be treated in a relatively separate manner. The second problem is discussed under this new framework of

pseudo-ZTs, through four subsections: (i) scattering and system dimension; (ii) band structure; (iii) density of states; (iv) band gap.

The carrier scattering mechanism(s) is (are) further studied. A new tool for scattering mechanism(s) inference and for the Seebeck coefficient enhancement is provided. For the band structure and the band gap part, an advanced band engineering method is provided to study nanostructured narrow-gap materials, the Dirac cone materials, and the anisotropic materials, which are historically found to be good thermoelectric materials. Discussions and future suggestions are provided in the final chapter.

Chapter 2

New Framework for Thermoelectric Theory

The bottle-neck for thermoelectric applications, both power generation and cooling, is to enhance the energy conversion efficiency, i.e. to enhance ZT. Tremendous efforts have been made since the Hicks-Dresselhaus model was proposed in 1993 [18], and these efforts have pushed the upper limit of ZT from ~1 to ~2. However, to realize large scale commercial use of thermoelectric technology, the cost and efficiency of thermoelectric materials need to be further improved significantly. To fulfill this task, a new framework for thermoelectric theory is provided in this chapter. This new framework of theory decomposes ZT into two pseudo-ZTs, where one pseudo-ZT measures the electronic contribution and the other scales the lattice contribution. By using this framework, deeper physics can be revealed, which gives important guidance for a more convergent way to develop materials science and engineering strategies to enhance ZT.

2.1 History of ZT Enhancement

Before the 1990s, the *ZT* of major thermoelectric materials was barely up to 1, as shown in Figure (2.1 a) [10].
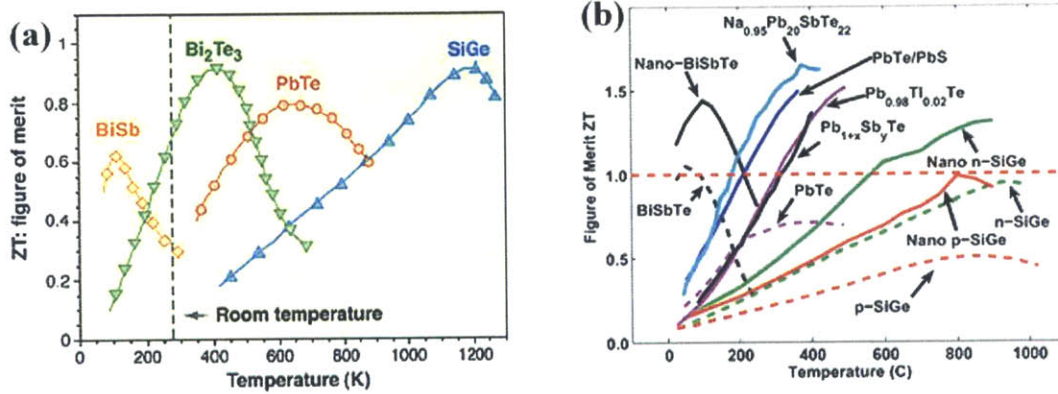
Figure 2.1: The achievement of highest *ZT* values of typical good thermoelectric materials up to 1993 (a) [10] and now (b) [19].

In 1993, Hicks and Dresselhaus proposed that by employing nanoscience and nanotechnology, it might be promising to have *ZT* much above 1 in low-dimensional materials systems, such as quantum wells and nanowires [18, 20]. Following this clue, researchers have made significant efforts to increase *ZT*. Mahan and Sofo pointed out that a sharp change in density of states near the Fermi energy may lead to a large Seebeck coefficient and an enhanced *ZT* [21]. Super-lattice structures and nanocomposite structures have also been used to further increase the Seebeck coefficient and to reduce the lattice thermal conductivity [22]. Heremans *et al.* managed to obtain high *ZT* values with PbTe materials by introducing resonant states into the band gap [23]. Later, Parker *et al.* suggested another approach using heavy doping to create a pipe-shaped Fermi surface for *ZT* enhancement [24]. Most of the *ZT* enhancing strategies that have been proposed since 1993 involve the changing and the controlling of the dimension of materials systems [18, 20], the scattering mechanism(s) of carriers [23], the shape of the electronic band structure [24]

and the density of states [21], and the band gap, which have pushed the upper limit of ZT to ~2, as shown in Figure (2.1 b).

2.2 Theory Basics for Modeling ZT

As shown in Equation (1.4), ZT can be calculated from all the transport properties, including the electrical conductivity (σ), the thermal conductivity (κ) and the Seebeck coefficient (S). Since thermoelectric systems are mostly used under low field conditions, the Boltzmann Transport Equations are widely used to model all these aforementioned transport properties. In this section, we review some of the most important theoretic basic concepts for describing such transport properties.

2.2.1 Band Structure

In solid state semiconducting materials, the energy (E) of allowed quantum states for electrons are functions of the lattice momentum ($\mathbf{k}$). The dispersion relation $E(\mathbf{k})$ controls the band structure [25]. Usually, the band structure is discussed within the first Brillouin zone, i.e. the first Wigner–Seitz cell in the reciprocal space. At absolute zero temperature ($T = 0$), all the electrons will be frozen within the valence band. The fully filled valence band will not contribute to the electronic transport. At a finite temperature above $T = 0$, a certain portion of the electrons at the top of the valence band will be thermally excited to the bottom of the conduction band, which leads to charge vacancies at the top of the valence band. A charge vacancy effectively possesses a positive charge within the background of the "electron sea", and is called a "hole". There is a forbidden energy range between the valence band and the conduction band, where no electrons or holes are allowed. This forbidden energy range is called the band gap. Only the carriers near the band gap, i.e. electrons at the bottom of the conduction band and holes at the top of the valence band contribute to the transport phenomena. The bottom of the conduction band and the top of valence band are called the band edges.

2.2.2 Effective Mass Theorem

In solid state physics, if we use $\Psi_n(\mathbf{r},t)$ to denote the nth wavefunction of electrons, where $\mathbf{r}$ is the coordinate of electrons in the real space and t is the real time, and we use $\psi_{n\mathbf{k}}(\mathbf{r})$ to denote the single color wavefunction [25]. In general, we have

$$\Psi_n(\mathbf{r},t) = \int \phi(\mathbf{r},\mathbf{k},t)\psi_{n\mathbf{k}}(\mathbf{r})d^3\mathbf{k}, \tag{2.1}$$

where $\phi(\mathbf{r},\mathbf{k},t)$ is the weight distribution of each singe color wavefunction in this wave-packet of electrons. However, if the electrons in solid state crystals are delocalized, i.e., the wavelength of electrons is much larger than the interatomic distance, the wave-packet of electron will be localized in the reciprocal space such that

$$\Psi_n(\mathbf{r},t) = \left[\int \phi(\mathbf{r},\mathbf{k},t)d^3\mathbf{k}\right]\psi_{n,\mathbf{k}_0}(\mathbf{r})$$

$$= \Phi_n(\mathbf{r},t)\psi_{n,\mathbf{k}_0}(\mathbf{r}), \tag{2.2}$$

where $\psi_{n,\mathbf{k}_0}(\mathbf{r})$ is the single color wavefunction at the average position $\mathbf{k}_0$ in the reciprocal space, and

$$\Phi_n(\mathbf{r},t) = \left[\int \phi(\mathbf{r},\mathbf{k},t)d^3\mathbf{k}\right] \tag{2.3}$$

is the envelope function for this wave-packet. Hence, the Schrödinger Equation can be effectively written as,

$$\left[E_n \left(\mathbf{k}_0 - i\nabla_{\mathbf{r}} \right) + V_{ext}(\mathbf{r}) \right] \Phi_n(\mathbf{r},t) = i\hbar \frac{\partial \Phi_n(\mathbf{r},t)}{\partial t},\qquad (2.4)$$

where E_n is the energy for the nth band. Equation (2.4) is the basic equation of Effective Mass Theory, which has many useful derivatives. An important one will be the $E(\mathbf{k})$ relation of parabolically dispersed carriers at the bottom of the conduction band or at the top of the valence band, as shown in Equation (2.5),

$$E(\mathbf{k}) = \frac{\hbar^2 \left(k_x - k_{edge,x} \right)^2}{2m_1^*} + \frac{\hbar^2 \left(k_y - k_{edge,y} \right)^2}{2m_2^*} + \frac{\hbar^2 \left(k_z - k_{edge,z} \right)^2}{2m_3^*}.\qquad (2.5)$$

where k_x, k_y and k_z are the three components of $\mathbf{k}$, while $k_{edge,x}$, $k_{edge,y}$ and $k_{edge,z}$ are the three components of the $\mathbf{k}$ value of the band edge ($\mathbf{k}_{edge}$), and m_1^*, m_2^*, m_3^* are the corresponding principal effective masses.

2.2.3 Boltzmann Transport Equation and the Relaxation Time Approximation

The Boltzmann Transport Equation deals with the transport of an ensemble of carriers [25]. The Occupancy Distribution Function $f(\mathbf{r},\mathbf{k},t)$ is used to describe this ensemble, which means the occupancy probability of a quantum state at position $\mathbf{r}$, lattice momentum $\mathbf{k}$ and time t. If we assume that the total number of carriers is conserved within a system, we have

$$\frac{\partial f}{\partial t} + \mathbf{F}_{ext} \cdot \nabla_{\mathbf{p}} f + \nabla_{\mathbf{p}} E \cdot \nabla_{\mathbf{r}} f = \frac{\partial f}{\partial t}\Big|_{scattering},\qquad (2.6)$$

where $\mathbf{F}_{ext}$ is the external force exerted on the carriers.

24

If the external electrical field is low and the scattering processes for the carriers are elastic, the scattering term on the right-side of Equation (2.6) can be described by an energy (E) dependent relaxation time function $\tau(E)$,

$$\frac{\partial f}{\partial t}\Big|_{scattering} = -\frac{f - f_0}{\tau(E)}, \tag{2.7}$$

where

$$f_0 = \frac{1}{\exp\left(\dfrac{E - E_f}{k_B T}\right) + 1} \tag{2.8}$$

is the Fermi-Dirac distribution function, E_f is the Fermi energy and k_B is the Boltzmann constant.

The transport properties can then be calculated using the Occupancy Distribution Function $f(\mathbf{r}, \mathbf{k}, t)$. The charge current density can be given by

$$J_{\text{Charge}}(\mathbf{r}, t) = -e \int f(\mathbf{r}, \mathbf{k}, t) \nabla_r E(\mathbf{k}) d^3 \mathbf{k}, \tag{2.9}$$

while the heat current density can be given by

$$J_{\text{Heat}}(\mathbf{r}, t) = \int f(\mathbf{r}, \mathbf{k}, t)(E - E_f) \nabla_r E(\mathbf{k}) d^3 \mathbf{k}. \tag{2.10}$$

Furthermore, at a steady state condition, $\partial f / \partial t = 0$ is satisfied, so we have

$J_{\text{Charge}}(\mathbf{r}, t) = J_{\text{Charge}}$ and $J_{\text{Heat}}(\mathbf{r}, t) = J_{\text{Heat}}$. By solving Equations (2.6), (2.7), (2.9) and

(2.10), we can get expressions for the electrical conductivity (σ), the Seebeck coefficient (S), and the electronic contribution to the thermal conductivity (κ_e),

$$\sigma = e^2 I_{[l=0]},$$ (2.11)

$$S = \frac{k_B}{e} \frac{I_{[l=1]}}{I_{[l=0]}},$$ (2.12)

$$\kappa_e = T k_B^2 \left(I_{[l=2]} - \frac{I_{[l=1]}^2}{I_{[l=0]}} \right),$$ (2.13)

where

$$I_{[l]} = \int \left(-\frac{\partial f_0}{\partial E} \right) \Xi(E)(\frac{E - E_f}{k_B T})^l dE$$ (2.14)

and

$$\Xi(E) = \sum_{\mathbf{k}'} \delta\left(E - E(\mathbf{k}') \right) \tau(E) vv.$$ (2.15)

Here the energy dependent function $\Xi(E)$ is called the Transport Distribution Function. For a general electron or hole pocket, the energy dependence of the Transport Distribution Function near the band edge can be written as,

$$\Xi(E) = \Xi_0 \left(\frac{E}{k_B T} \right)^{\eta}$$ (2.16)

where

26

$$\Xi_0 = g_e \cdot a_\eta \qquad (2.17)$$

in which g_e is the electronic geometrical factor, and a_η is the normalization factor. For calculation, we illustrate the use of the above formalism in a 3-dimensional (3D) parabolically dispersed band valley, which is described by Equation (2.5), for clarification. The density of states for such a band edge is

$$D(E) = \frac{\sqrt{m_1^* m_2^* m_3^*}}{\sqrt{2}\pi^2 \hbar^3} E^{\frac{1}{2}}, \qquad (2.18)$$

and the Scattering Relaxation Time Function is

$$\tau(E) = \tau_0 \left(\frac{E}{k_B T}\right)^{-j}, \qquad (2.19)$$

where the coefficient τ_0 depends on the scatting strength and the exponent j depends on the energy dependence of the specific scattering mechanism(s). Therefore, the Transport Distribution Function can be written as,

$$\Xi_i(E) = \frac{(m_1^* m_2^* m_3^*)^{\frac{1}{3}}}{m_i^*} \frac{\sqrt{2}\tau_0 (m_1^* m_2^* m_3^*)^{\frac{1}{6}}}{3\pi^2 \hbar^3 (k_B T)^{-j}} E^{\frac{3}{2}-j}, \qquad (2.20)$$

where the subscript i (=1, 2, or 3) is the indicator for the three different principal transport directions. In this case, the parameters in Equations (2.16) and (2.17) are related to

$$g_e = \frac{(m_1^* m_2^* m_3^*)^{\frac{1}{3}}}{m_i^*}, \qquad (2.21)$$

27

$$a_\eta = \frac{\sqrt{2}\tau_0 (m_1^* m_2^* m_3^*)^{\frac{1}{6}}}{3\pi^2 \hbar^3 (k_B T)^{-J}},$$ (2.22)

and

$$\eta = \frac{3}{2} - j.$$ (2.23)

2.2.4 Multi-Channel Transport

In the case where the transport of the whole system has contributions from more than one channel, the overall transport can be calculated by [17, 25],

$$\sigma = \sum_i \sigma_i,$$ (2.24)

$$S = \frac{\sum_i \sigma_i S_i}{\sum_i \sigma_i},$$ (2.25)

and

$$\kappa_e = \sum_i \kappa_{e,i} + T \sum_{i \neq j} \frac{\sigma_i \sigma_j}{\sigma_i + \sigma_j} \left(S_i - S_j \right)^2.$$ (2.26)

The second term on the right side of Equation (2.26) can increase the thermal conductivity greatly, especially for narrow-gap materials, and is responsible for the so-called bipolar effect.

28

2.3 Problems with *ZT* Enhancement

As mentioned before, there is still a distance for thermoelectric technology to become commercially used regarding its energy conversion efficiency. As further research is carried out, it is found that the above mentioned strategies do not always work to enhance *ZT*. Even for a working materials system, the improvement margin of increasing *ZT* can be small. This can be explained from the definition of *ZT* in Equation (1.4). To enhance *ZT* by controlling the electrical conductivity (σ), thermal conductivity (κ) and Seebeck coefficient (S) occurs with extreme difficulty. For one thing, the electrical conductivity (σ) is positively correlated with the thermal conductivity (κ), where the electronic contribution to the thermal conductivity (κ_e) can be approximated by the Wiedemann–Franz law as shown in Equation (2.1), where L is called the Lorentz Number. The Lorentz Number for a simple metal can be approximated by a free electron gas model as,

$$L = \frac{\pi^2}{3}\left(\frac{k_B}{e}\right)^2 = 2.44 \times 10^{-8} \ \mathrm{W\Omega K^{-2}},$$

where e is the elementary charge. For another thing, the electrical conductivity (σ) and the Seebeck coefficient (S) are usually negatively correlated as shown in Figure (2.2) [26].
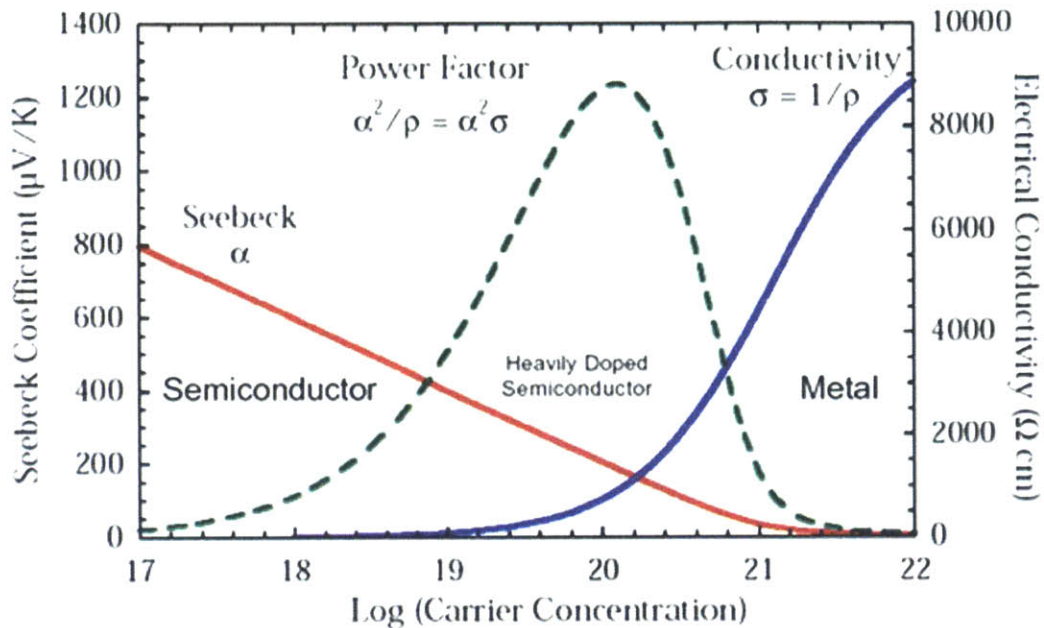
Figure 2.2: The negative correlations of the electrical conductivity and the Seebeck coefficient for a general materials system with different carrier concentrations [26].

Therefore, we can see that most of these ZT enhancing strategies now in use are balancing strategies between σ and S^2/κ. This can be understood by simple illustrations of the extreme cases. For example, a typical metal will have large electrical conductivity (σ), but will usually be compensated by the large thermal conductivity (κ) and the small Seebeck coefficient (S). As a second example, a conventional insulating plastic material will have a large Seebeck coefficient (S) and a small thermal conductivity, which will, however, be compensated by a very small electrical conductivity (σ). These two examples show that the balancing strategies are like playing a "seesaw balancing" game, and this is why the balancing game significantly limits the improvement margin for our ZT enhancing goal.

The above discussion identifies two problems that are crucial for the field of thermoelectrics: (1) how can we deal with the strong correlation between σ and S^2/κ, when

trying to enhance ZT, and (2) how can we make the above mentioned strategies more convergent as we change the dimension of materials systems, the scattering mechanism(s) of carriers, the shape of electronic band structure, and the magnitude of the band gap?

2.4 Solving the Problems by Proposing Pseudo-*ZT*s

My proposal for tackling this transport "balancing" problem as posed in Section 2.3 is to reformulate the definition of ZT into pseudo-ZTs as in Equation (2.27), where the strong correlations within the form of the multiplications in Equation (1.4) can be effectively avoided. The framework of the pseudo-ZTs is structured as [27],

$$\frac{1}{ZT} = \frac{1}{zt_e} + C \cdot \frac{1}{zt_L} \tag{2.27}$$

where

$$zt_e = \frac{1}{\dfrac{J_0^{[l]} J_2^{[l]}}{\left(J_1^{[l]}\right)^2} - 1}, \tag{2.28}$$

$$zt_L = \frac{\left(J_1^{[l]}\right)^2}{J_0^{[l]}}, \tag{2.29}$$

and

$$C = \frac{\kappa_L^{bulk}}{T} \cdot \frac{1}{\left(g_e / g_L\right) a_\eta k_B^{\,2}} \cdot \tag{2.30}$$

Here

$$J_r^{[l]} = \int\limits_{x=(E_m - E_f)/k_B T}^{\infty} \frac{\exp(x)}{\left(1 + \exp(x)\right)^2} \cdot \left(x - \frac{E_m - E_f}{k_B T}\right)^l \cdot x^r dx, \tag{2.31}$$

and

$$\kappa_L = g_L \cdot \kappa_L^{bulk}, \tag{2.32}$$

where E_m is the electron or hole carrier energy at the band edge. l=0, 1 or 2. κ_L is the lattice

thermal conductivity for a specific material, κ_L^{bulk} is the lattice thermal conductivity for the

corresponding bulk material, and g_L is the lattice geometrical factor, as an example, for a 3D

bulk crystal material, $g_L = 1$, while g_e and a_η are as defined in Equation (2.16)-(2.23).

In Equation (2.27)-(2.32), we see that the pseudo-ZT term zt_e only measures the

electronic influence to the total ZT, while the pseudo-ZT term zt_L only scales the lattice

influence to the total ZT. We see further that the lattice influence is calibrated by the

geometrically normalized lattice thermal conductivity C, which is proportional to the bulk

crystal lattice thermal conductivity and inversely proportional to the absolute temperature, i.e.

$$C \propto \frac{\kappa_L^{bulk}}{T} . \tag{2.33}$$

Under the framework of Equation (2.27), the multiplication relation between the three transport

properties in Equation (1.4) is changed to the addition relation of two transport related terms.

This step largely relaxes the correlation between terms that we need to consider in our more

convergent approach toward optimizing the total ZT. This will be seen clearly in the following sections, where deeper physics can be revealed relative to our goal of thermoelectric ZT enhancement.

2.5 How Scattering and Dimension Affect ZT

Many efforts have been made to enhance ZT by changing the carrier scattering mechanism(s) or changing the dimension of materials systems, e.g. by synthesizing a specific material into two-dimensional thin films or one-dimensional nanowires. While the improvement of ZT has been achieved in some materials systems, it is puzzling that the methods of changing the scattering mechanism(s) or the efforts of lowering the dimensionality do not always work for all systems. In some materials systems, low-dimensional materials even have lower ZT than their bulk materials counterparts. We here try to answer how to deal with this puzzle and we then propose a divide-and-conquer strategy on how to enhance ZT by controlling the carrier scattering mechanism(s) or changing the dimension of materials systems [27].

In Figure (2.3), it is shown how the two pseudo-ZTs change with the carrier concentration for systems of different dimensions.
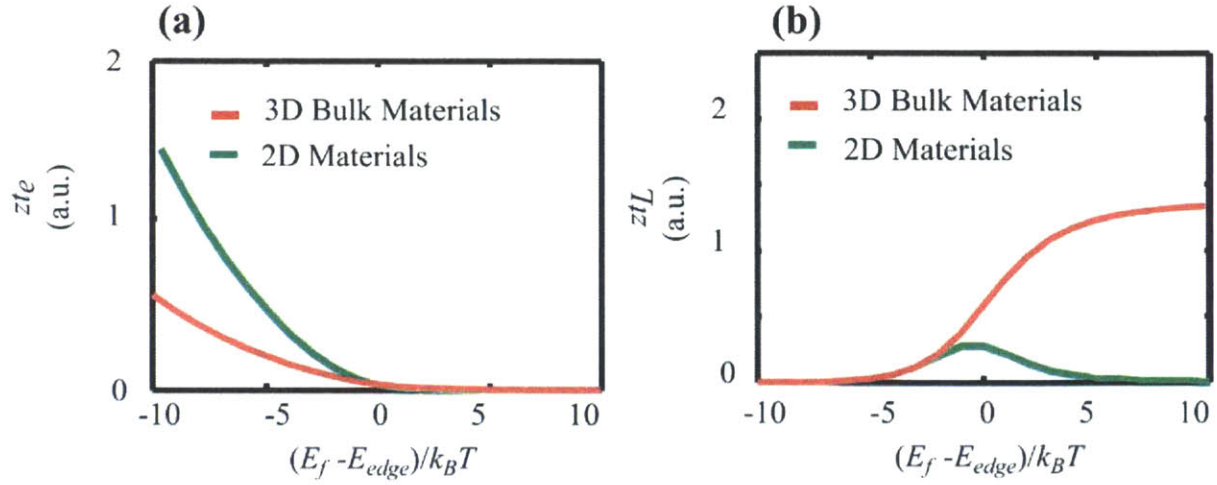
Figure 2.3: Illustration of how changing the dimension of a materials system can change the two pseudo-ZTs, zt_e and zt_L, in opposite directions. The red curve represents a three-dimensional parabolic band valley, and the green curve represents a two-dimensional parabolic band valley. To make a fair comparison, it is assumed that this three-dimensional band valley and this two-dimensional band valley have the same effective mass, and the same constant carrier scattering relaxation time along the different directions. For the zt_e part, the lower dimension system has a higher pseudo-*ZT*; for the zt_L part, the lower dimension system has a lower pseudo-*ZT*. Therefore, changing the dimension of a materials system, e.g. by making the materials into nano-form, will change zt_e and zt_L in opposite directions. This also tells us that for low carrier concentrations, it may be an advantage to use low dimensional materials rather than 3D bulk materials, while for the high carrier concentrations as defined in this thesis, 3D bulk materials are more promising for thermoelectrics. With this introduction, we now develop these ideas further.

For the purpose of illustration, a three-dimensional (red curve) parabolic band system and a two-dimensional (green curve) parabolic band system are chosen, where the constant relaxation time scattering is dominant in both cases. It is clear that while the low-dimensional system has higher zt_e than the three-dimensional system, as shown in Figure (2.3 a), it also has lower zt_L compared to the bulk case, as shown in Figure (2.3 b). I have calculated the cases of other

scattering mechanism(s) and dimensions, which all show that the changing of dimension of a materials system will change the two pseudo-ZTs in opposite directions.

I further calculated the influence of changing the scattering mechanism(s) on the two pseudo-ZTs, as shown in Figure (2.4). For the purpose of illustration, we here show a three-dimensional parabolic band system where the acoustic phonon
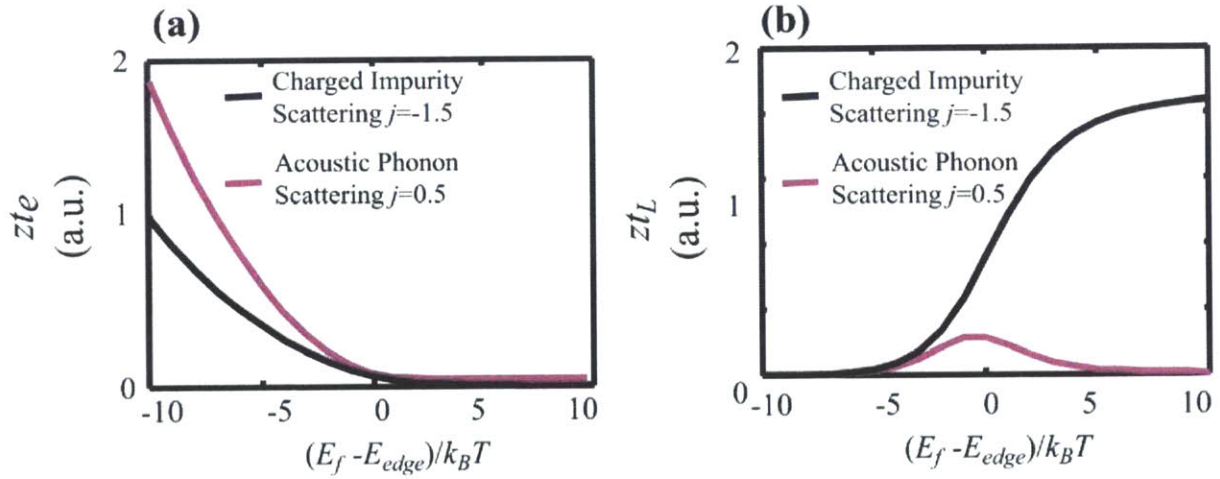
Figure 2.4: Illustration of how changing the carrier scattering mechanism(s) of a transport system can change the two pseudo-ZTs, zt_e and zt_L, in opposite directions. The black curve represents a case where the charged impurity scattering mechanism is dominant, and the purple curve represents a case where the acoustic phonon scattering mechanism is dominant. To make a fair comparison, it is assumed that both of these two system have a three-dimensional parabolic band valley. For the zt_e part, the acoustic phonon scattering with lower scattering order ($j = -0.5$) has higher pseudo-ZT; for the zt_L part, the charged impurity scattering with higher scattering order ($j = 1.5$) has lower pseudo-ZT. Therefore, changing the scattering mechanism(s) of a transport system, e.g. by adding foreign ionized impurities, will also change zt_e and zt_L, in opposite directions.

scattering is dominant (purple curve), and another three-dimensional parabolic band system where the ionized impurity scattering is dominant (black curve). We still see clearly that while

the acoustic phonon scattering system has higher zt_e than the ionized impurity scattering system, as shown in Figure (2.4 a), it also has lower zt_L compared to the ionized impurity scattering, as shown in Figure (2.4 b). We have calculated the cases of other scattering mechanism(s) and dimensions, which all show that the changing of scattering mechanism(s) of carriers will also change the two pseudo-ZTs in opposite directions.

Figure (2.3) and (2.4) have answered the question why the methods of changing dimension or scattering to enhance ZT sometimes work, but sometimes do not work: they change zt_e and zt_L in opposite directions. Therefore, we accordingly propose a divide-and-conquer strategy, instead of a blind trial strategy. Before we consider changing the dimension of scattering, we should first examine the geometrically normalized lattice thermal conductivity $C \propto \kappa_L^{bulk} / T$. If C is small, the total ZT is dominated by zt_e according to Equation (2.27). In this case, we should try to increase the scattering order (j) in Equation (2.19) by e.g. adding charged impurities, and we should also try to decrease the dimension of the materials system by utilizing nanostructured materials, e.g. thin films, nanowires, etc. If C is large, the total ZT is dominated by zt_L according to Equation (2.27). In this case, we should try to decrease the scattering order (j) by e.g. reducing the concentration of charged impurities, and we should keep the materials system in bulk form. If C is moderate, zt_e and zt_L will be comparable to each other. Accordingly we suggest that the strategies regarding changing scattering mechanism(s) or changing materials system dimension will not improve ZT in a notable way, due to the balancing of loss and gain between zt_e and zt_L. The relation between scattering mechanism(s) and thermoelectric behaviors will be further discussed in Chapter 3.

2.6 How Band Asymmetry Affects ZT

It will be helpful to study what are the common properties of the band structures for the traditional good thermoelectric materials, e.g. bismuth antimony, lead telluride, and bismuth selenide. These materials are always related to narrow-band-gap semiconductors, Dirac cone materials, and topological insulators. Further, we see that these materials usually have better P-type thermoelectric behavior than N-type. Based on the aforementioned phenomena, we make a conjecture that the good thermoelectric performance, especially for the P-type cases, originates from the large asymmetry of the carrier effective masses between electrons and holes. To verify this conjecture, we now examine how this band asymmetry ratio affects the pseudo-ZTs of zt_e and zt_L for such systems. We define the band asymmetry ratio as the ratio between the radii of curvature for the electron dispersion and the hole dispersion, i.e.

$$\beta = \frac{1}{\left(\dfrac{\partial^2 E}{\partial k^2}\right)\bigg|_{\text{Electrons}}} \bigg/ \frac{1}{\left(\dfrac{\partial^2 E}{\partial k^2}\right)\bigg|_{\text{Holes}}}, \tag{2.34}$$

which in the case of parabolic bands can be simplified to be the ratio of the effective masses, i.e.

$$\beta = \frac{m^*\big|_{\text{Electrons}}}{m^*\big|_{\text{Holes}}}. \tag{2.35}$$

Without loss of generality we assume a system at temperature T to have a band gap of $E_g = k_B T$. We also assume that the scattering mechanism(s) for the electrons and the holes are the same, so that the comparison can be focused on the band asymmetry. The pseudo-ZTs are calculated as a function of band asymmetry

ratio β, as shown in Figure (2.5) [27, 28].

(a)

maximum zt_e (a.u.)

Band Asymmetry β

— Charged Impurity
    Scattering j=-1.5

— Acoustic Phonon
    Scattering j=0.5

(b)

maximum zt_L (a.u.)

Band Asymmetry β

— Charged Impurity
    Scattering j=-1.5

— Acoustic Phonon
    Scattering j=0.5
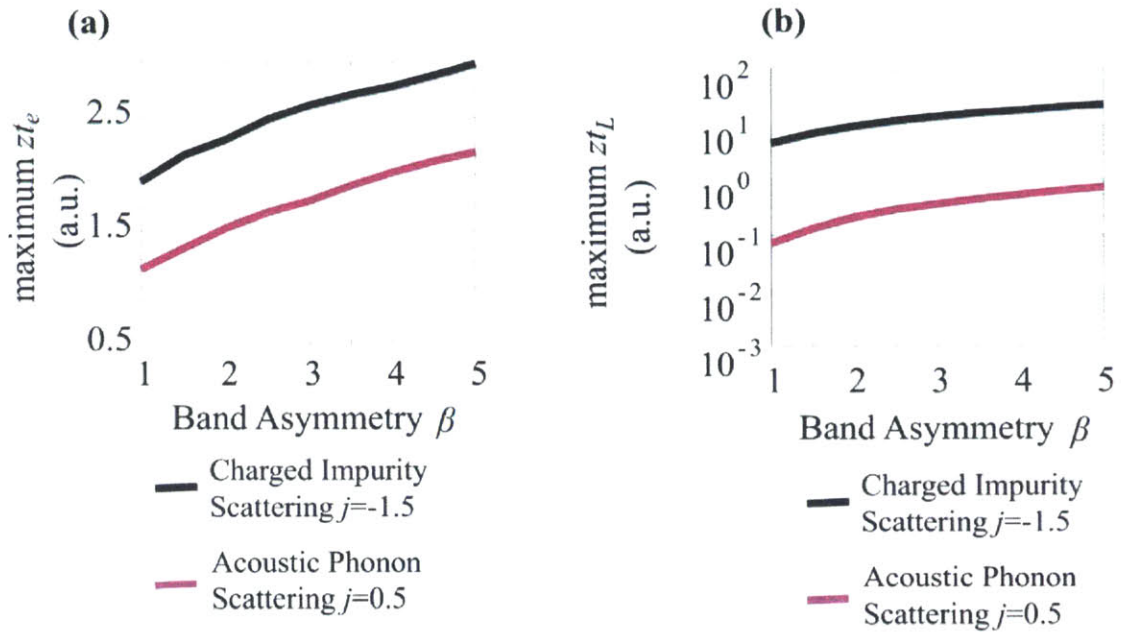
Figure 2.5: Illustration of how an increase of band asymmetry ratio β between the conduction band and the valence band can increase the two pseudo-ZTs, zt_e and zt_L, in the same direction. The black curve represents a case where the charged impurity scattering mechanism is dominant, and the purple curve represents a case where the acoustic phonon scattering mechanism is dominant. To make a fair comparison, it is assumed that both of these two systems have a three-dimensional parabolic band valley. Unlike the change of scattering mechanism(s) or the change of the system dimension, the increase of band asymmetry ratio β will increase both zt_e and zt_L together, regardless of the scattering mechanism(s) or the system dimension.

We see that unlike the case of the system dimension in Figure (2.3) or the scattering mechanism(s) in Figure (2.4), the band asymmetry ratio β in Figure (2.5) changes both the zt_e and zt_L in the same direction. The three-dimensional systems that have parabolic bands and charged impurity scattering (black curve), or acoustic phonon scattering (red curve) are shown here. The cases of other scattering mechanism(s) and system dimensions have also been calculated, which have shown the same tendency. This tells us that although, changing the

scattering or dimension may even sometimes result in reduced ZT, choosing large band asymmetry materials may always enhance the maximum values of ZT.

This is consistent not only with the good thermoelectric performance of narrow-band-gap semiconductors, Dirac cone and topological insulator related materials, where the electron carriers are effectively much lighter than the heavy hole carriers, but also with the nanocomposite approach, where the induced network of nanoscale grain boundaries forms a screening system for the holes, and effectively making the band asymmetry ratio β larger.

2.7 How Band Gap Affects ZT

As mentioned above, the traditional well behaved thermoelectric materials are mainly narrow-band-gap semiconductors or semimetals. This naturally raises a question for us: how about wide-band-gap materials? The traditional viewpoint has been that wide-band-gap materials have small carrier concentrations, and therefore have poor thermoelectric performance. However, from Figure (2.2) we can see that, good thermoelectric performance does not necessarily depend on large carrier concentrations. Actually, a large carrier concentration may only imply a large electrical conductivity (σ) in Equation (1.4), but as we explained in the previous sections, the large electrical conductivity (σ) is always accompanied by a reduced Seebeck coefficient (S) and an increased thermal conductivity (κ) as shown in Figure (2.1), which reduces the thermoelectric ZT as a whole.

In order to have a birds-eye picture of how the band gap affects the whole thermoelectric ZT, I calculated the pseudo-ZTs versus band gap relation as shown in Figure (2.6).

(a)

(b)
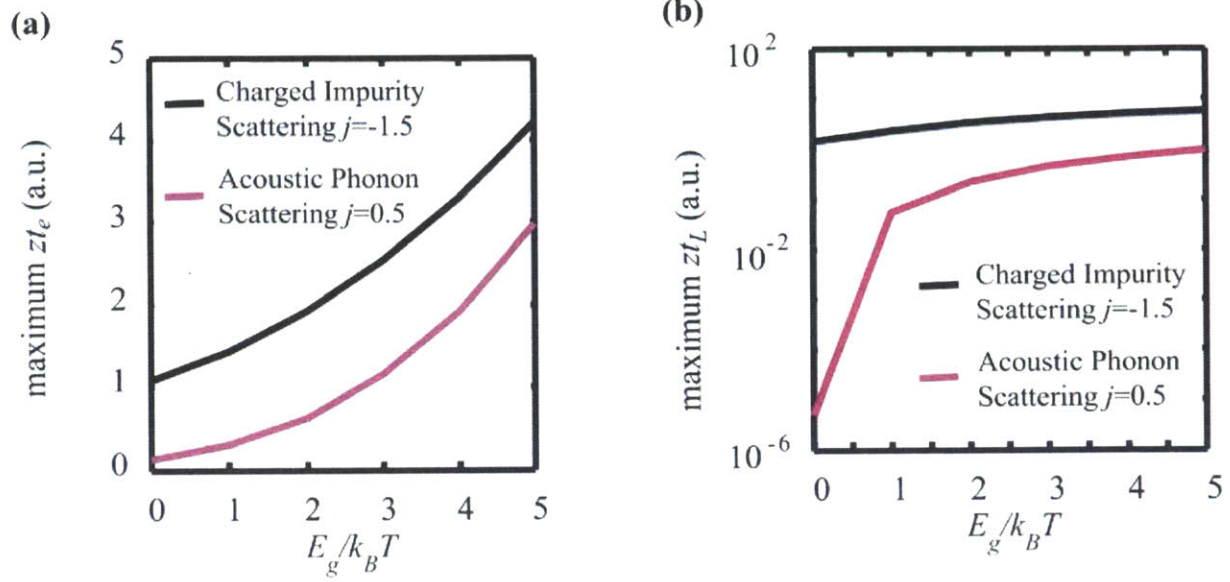
Figure 2.6: Illustration of how an increase in the band gap between the conduction band and the valence band can increase the two pseudo-ZTs, zt_e and zt_L, in the same direction. The black curve represents a case where the charged impurity scattering mechanism is dominant, and the purple curve represents a case where the acoustic phonon scattering mechanism is dominant. To make a fair comparison, it is assumed that both of these two systems have a three-dimensional parabolic band valley. Unlike the change of the scattering mechanism(s) or the change of system dimensions, an increase of the band gap will increase both zt_e and zt_L together, regardless of the scattering mechanism(s) or the system dimensions, as mentioned in the text.

The three-dimensional systems of parabolic bands with charged impurity scattering (black curve), and with acoustic phonon scattering (red curve) are shown in Figure 2.6. The cases of other scattering mechanism(s) and system dimensions have also been calculated, and they also have shown the same tendency. We see that the band gap will increase both zt_e and zt_L, although the tendency of increase is stronger in zt_e than in zt_L. Different from the traditional

40

view, we see that a wide band gap is not necessarily harmful for enhancing the thermoelectric *ZT*.

The real problem for utilizing wide band gap materials for thermoelectric applications is how to control the Fermi level by doping. I suggest for future research directions to use nanostructures and amorphous structures for increasing the thermal stability of dopings. Further, the typical large lattice thermal conductivity of wide-band-gap semiconductors is also a large concern. This concern can also be reduced by the nanostructure approach e.g. nanocomposites structures, polycrystalline structures and amorphous structures, which can largely reduce the mean free path of phonons.

2.8 Demonstration in Specific Materials

In the previous sections, I have provided the general mathematical descriptions to show how the framework of pseudo-*ZT*s can be used to see the new physics of *ZT* enhancement. In this section, we illustrate this method of pseudo-*ZT* in some specific systems.

2.8.1 Demonstration in Metal Dichalcogenide Monolayer Materials Systems

We first demonstrate the pseudo-*ZT* framework in metal dichalcogenide monolayer systems. This class of materials system is currently attracting intensive research attention. Because of the single-layer structure, the Fermi level of a metal dichalcogenide monolayer can be changed not only by doping, but also by adatoms absorption [29] and gating voltage [30], which gives us more opportunities to study the largest possible *ZT*. This class of materials system might not be the best thermoelectric materials, but as long as our purpose here is to demonstrate the idea that using the framework of pseudo-*ZT*s, the trend of *ZT* changes can be seen more clearly than using the traditional transport properties, the metal dichalcogenide monolayer materials system is a good example [29-41].

zt_L (a.u)
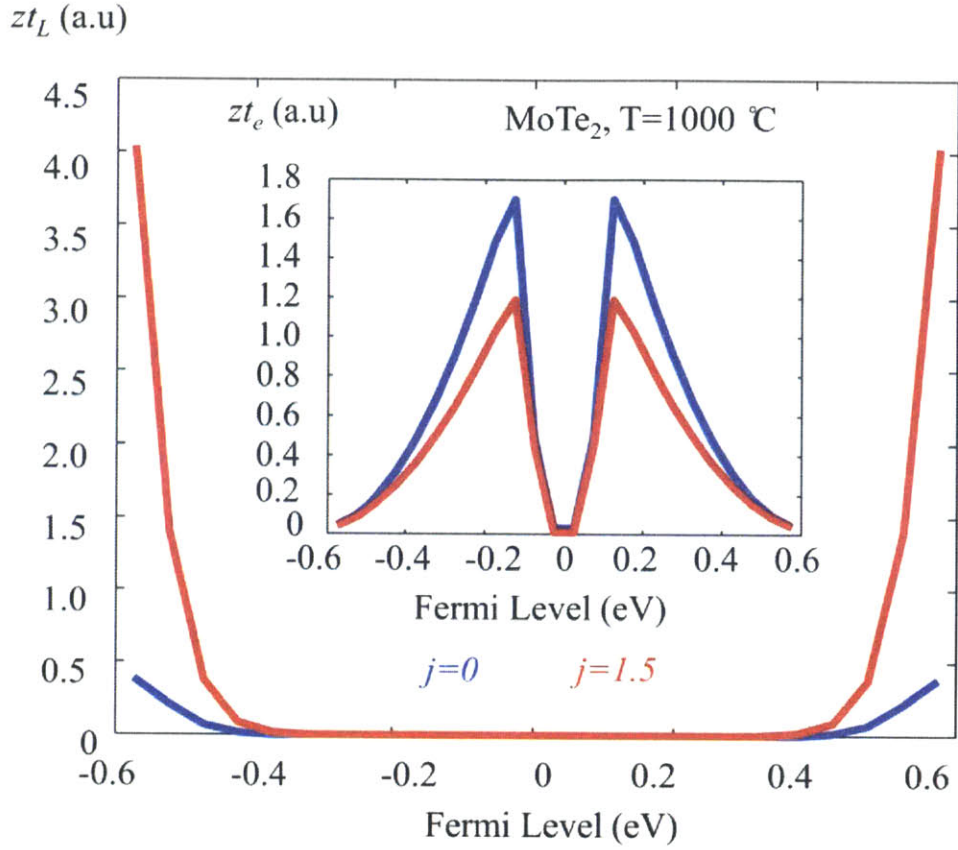
Figure 2.7: The demonstration of how changing the scattering order j will change zt_e and zt_L in different directions. This demonstration is calculated based on the properties of MoTe$_2$ monolayers at a temperature of 1000 °C [29-41]. The blue curves stand for the pseudo-ZTs when the scattering order (j) in the relaxation time function $\tau = \tau_0 \left(E / k_B T \right)^j$ is 0. The red curves stand for the case where the scattering order (j) is 1.5. We see that at different values of Fermi level, when j increases, the zt_e value decreases, and the zt_L value increases. This is consistent with the predictions we have in the general physical model discussed in Section 2.5.
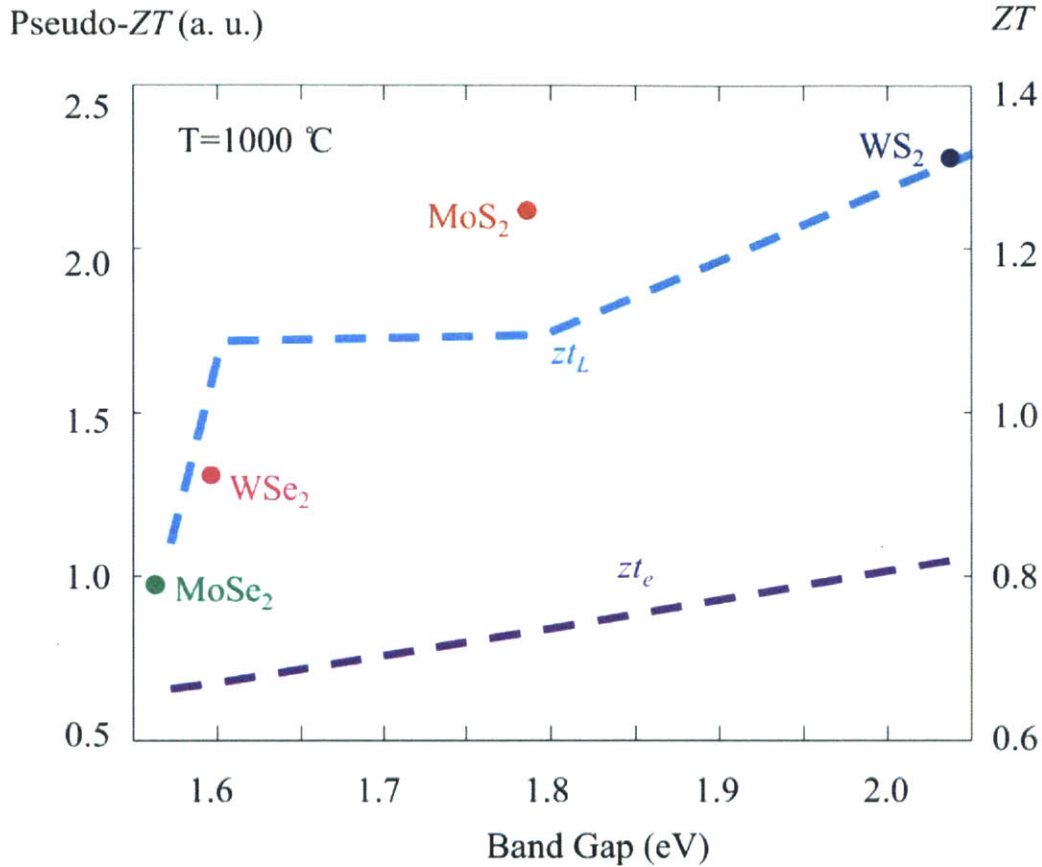
Figure 2.8: The demonstration of how the band gap increases both of the pseudo-*ZT*s. The dashed lines are the calculated pseudo-*ZT*s for the metal dichalcogenide monolayer materials with different values of band gap: zt_e (violet) and zt_L (light blue) [29-41]. We see that unlike the changing of scattering order shown in **Figure 2.7**, choosing larger band gap within the same class of materials is increasing both zt_e and zt_L. This leads to the increase of the overall *ZT*, which is calculated and marked by the dots with different colors. This trend would not be clearly seen if we calculate the traditional transport properties of the electrical conductivity, the Seebeck coefficient and the thermal conductivity.

We see from Figure 2.7 that the change of scattering order j will change the two pseudo-*ZT*s in different directions, which is consistent with the mathematical discussion in Section 2.5. We also see from Figure 2.8 how pseudo-*ZT*s and *ZT*

changes when we choose the metal dichalcogenides monolayer materials with different values of band gap. Both zt_e and zt_L increase when the mononlayer material with larger value of band gap is chosen, and therefore, larger values of ZT can be achieved. This is consistent with the mathematical prediction we discussed in Section 2.7.

2.8.2 Demonstration in Traditional Semiconducting Alloy Materials Systems

Here we also demonstrate the use of the pseudo-ZT framework in traditional semiconducting alloys, including $(Bi_{1-y}Sb_y)_2(S_{1-x}Te_x)_3$ film materials [42, 43], and $In_{1-x}Ga_xN$ bulk materials [44-47]. Both of these materials systems are traditional studied, so the various parameters can be extracted from the literatures, which is very helpful for our demonstration purpose.

(b)

(c)

(d)
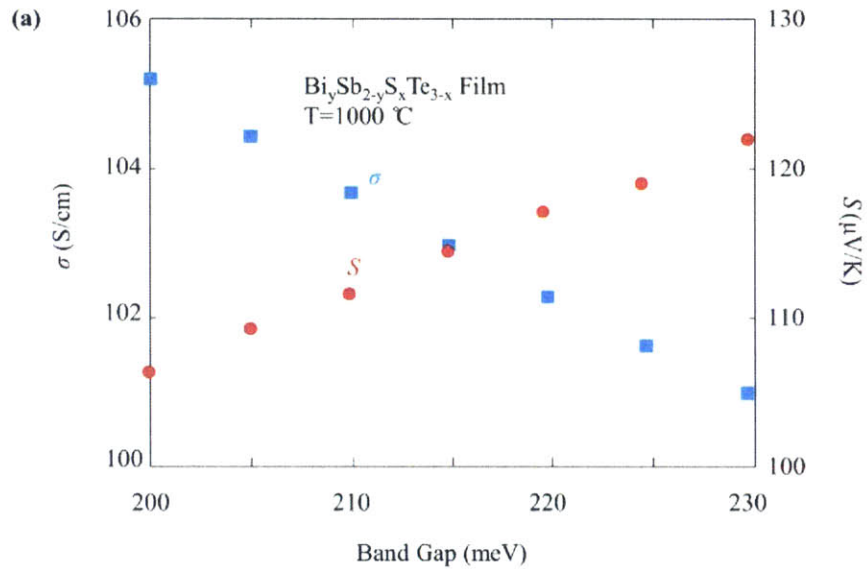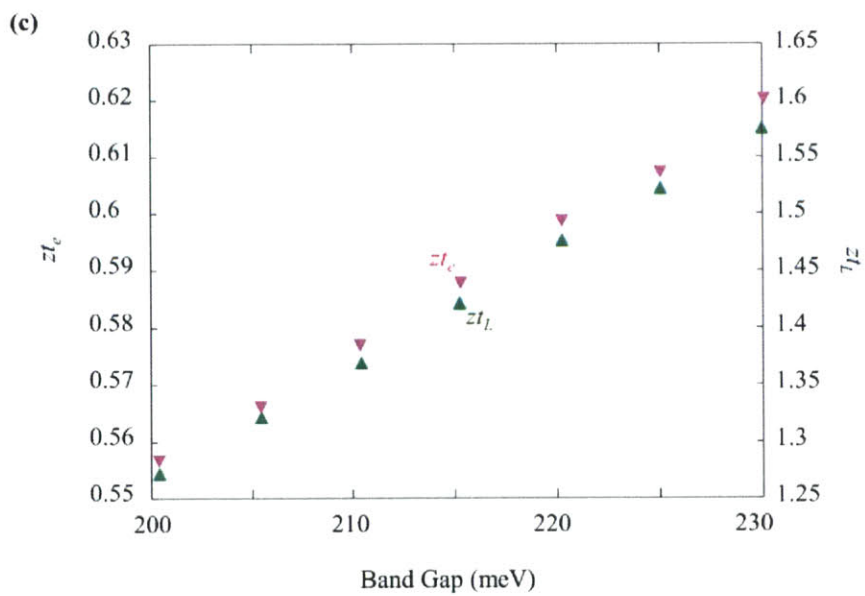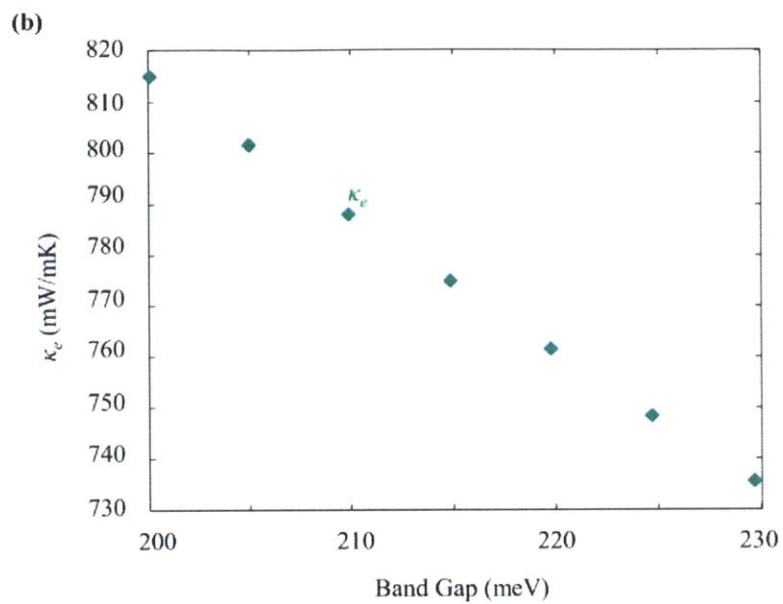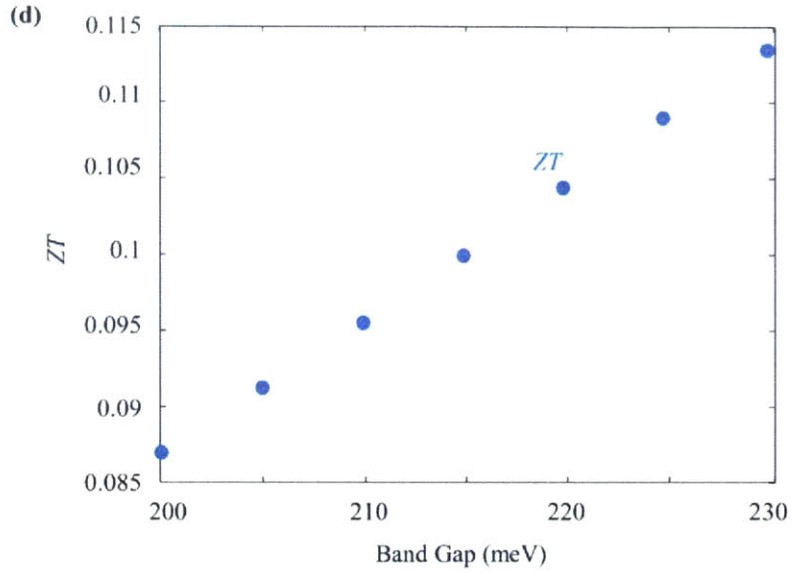
Figure 2.9: The *ZT* values of $(Bi_{1-y}Sb_y)_2(S_{1-x}Te_x)_3$ film materials [42, 43]. The stoichiometry and film thickness are changed to tune the band gap of the alloy materials. The max values of *ZT* near the band edge increases with band gap, as predicted by the model we discussed in Section 2.7.
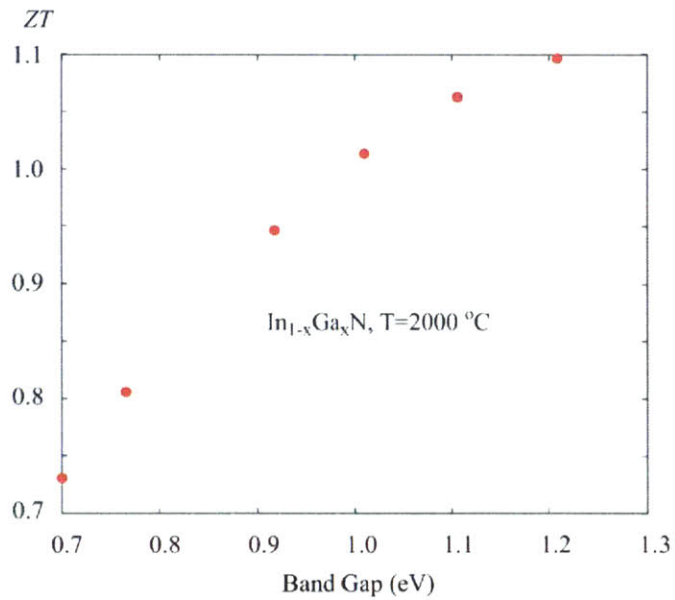
Chapter 3

New Scattering Inference and Seebeck Coefficient Enhancement

In a materials system, the transport of energy, entropy and electricity are made through the carriers, i.e. electrons and holes. The carriers are scattered by various scattering centers during the transport process, as shown in Figure 3.1. The different carrier scattering mechanisms ultimately determine the transport and thermoelectric performance. Therefore, it is very important to have an inference tool to examine the specific scattering mechanism(s) within a specific semiconducting system that we are interested in.

This Chapter is reprinted/adapted from the published work: [a] S. Tang and M. Dresselhaus, "Anisotropic transport for parabolic, non-parabolic, and linear bands of different dimensions", *Applied Physics Letters*, **105**, 033907 (2014). [b] S. Tang and M. Dresselhaus, "New Method to Detect the Transport Scattering Mechanisms of Graphene Carriers", *arXiv*, **1410**.4907, (2014).

decrease the system dimension, e.g. by introducing more charged impurity scattering centers and utilizing nanostructures. However, if the value of κ_L^{Bulk}/T is large, and the total ZT is dominated by zt_L, then we should try to decrease the scattering order and increase the system dimension, e.g. by reducing the concentration of foreign impurities and keeping the materials in the bulk form. If κ_L^{Bulk}/T is moderate, we should anticipate that the strategies of changing materials system dimension or scattering mechanism(s) will not significantly help in enhancing the total ZT.

The influence of band asymmetry on the total ZT is also clearly shown under this new framework of pseudo-ZTs. We have seen that increasing the band asymmetry will increase both zt_e and zt_L. This explains why the traditional well-behaved thermoelectric materials are mostly related to narrow-band-gap semiconductors, and Dirac cone or topological insulator related materials. This is because such materials typically have light electrons and heavy holes which results in a large band asymmetry ratio.

Further, the influence of the magnitude of the band gap to the total ZT is here investigated from a birds-eye picture. In contrast to the traditional low expectation on wide-band-gap materials, we found that a wide-band-gap is not necessarily harmful to enhancing ZT. In such cases, increasing the band gap will increase both zt_e and zt_L, though the increase in zt_L will be smaller than the increase in zt_e, and few detailed studies of this case have yet been carried out. In this way, new research opportunities have been identified and are likely to have some impact on how thermoelectric materials are optimized in the future.

The use of the framework of pseudo-ZT to see the new physics of enhancing ZT is demonstrated in some specific materials systems, including the various metal dichalcogenide monolayer materials, the $(Bi_{1-y}Sb_y)_2(S_{1-x}Te_x)_3$ film alloy materials and the $In_{1-x}Ga_xN$ bulk alloy materials.

than the correlations between the electrical conductivity, the thermal conductivity and the Seebeck coefficient, but the correlations is not totally avoid. For example, the geometrically normalized lattice thermal conductivity C, as we defined in Equation (2.30), will be positively correlated with the band-gap. This is due to the fact that wide gap materials usually have large inter-atomic distances, which leads to small spring constants under the first order approximation. The small inter-atomic spring constants will then lead to small values of sound velocity, and result in large values of lattice thermal conductivities that will jeopardize the overall ZT.

2.10 Chapter Summary

In this chapter, I reformulated the expression for ZT into Equation (2.27), so that we only need to deal with two pseudo-ZTs, zt_e and zt_L, which are much less correlated with one another. This was done in order to avoid tackling with the multiplication relation between the electrical conductivity (σ), the thermal conductivity (κ) and the Seebeck coefficient (S) in the expression of thermoelectric ZT defined in Equation (1.4). The definition of ZT in Equation (1.4) is a natural way to understand what ZT is, but not an easy way to understand how to enhance ZT. In contrary, the reformulation of ZT in Equation (2.27) is not a natural way to understand what ZT really means, but is a much easier way to understand how to enhance ZT, where zt_e only measures the electronic influence, and zt_L only scales the lattice influence.

Under this new framework of pseudo-ZTs, we are able to answer the puzzle of why the strategies of changing carrier scattering mechanism(s) and making materials into a nano-form do not always work. It is because the changing of carrier scattering mechanism(s) and materials system dimension will change the two pseudo-ZTs, zt_e and zt_L, in opposite directions. Therefore, I developed a divide-and-conquer strategy. Before we start trying any approaches regarding the change of scattering or dimension, we need to first look at the geometrically normalized lattice thermal conductivity C defined in Equation (2.3), i.e. look at the bulk crystal lattice conductivity κ_L^{Bulk} and the working temperature T. If the value of κ_L^{Bulk}/T is small, the total ZT is dominated by zt_e. In this case, we should try to increase the scattering order and to

Figure 2.10: The ZT values of $In_{1-x}Ga_xN$ bulk materials [44-47]. When the gallium composition is changed from 0-0.1 to tune the band gap of the alloy materials, ZT increases with band gap, as predicted by the model we discussed in Section 2.7.

From Figures 2.9 (a) and (b), we see that when we increase the band gap of the $(Bi_{1-y}Sb_y)$ $_2(S_{1-x}Te_x)_3$ film materials, the electrical conductivity and electronic thermal conductivity decreases, while the Seebeck coefficient increases, which is just the "balancing game" again. This "balancing game" makes it difficult to see how the increase of band gap will benefit ZT. However, if we look at Figure 2.9 (c), we will see that both of the pseudo-ZTs increases with the band gap, which implies that the overall ZT will increase when we increase the band gap. Such a trend of increasing ZT is shown in Figure 2.9 (d). Therefore, Figure 2.9 has demonstrated that the framework of pseudo-ZTs can provide us with a more convenient way to discuss how to enhance ZT. The similar results are shown in Figure 2.10 as well for the $In_{1-x}Ga_xN$ bulk materials, where we see that the overall ZT increases with the band gap when the gallium composition is changed slightly to tune the band gap.

2.9 Discussions

We have developed the framework of pseudo-ZTs for the purpose of selecting and improving thermoelectric materials candidates more efficiently. Suppose we have a pool of materials candidates for potential thermoelectric applications. Before this new framework, if we want to know which materials candidates are the most promising ones for thermoelectric applications, we have to calculate the electrical conductivities, the thermal conductivities and the Seebeck coefficients for all these materials candidates, to obtain their ZT values. However, using this new tool, we can just focus on the ones with high band asymmetry ratio and large band-gap-to-temperature ratio, based on the results in Section 2.6-2.8. Then we can use the divide-and-conquer strategy we developed in Section 2.5 to select out the most promising ones. Then we can focus on only study these most promising materials candidates. This will save us a lot of time on calculations and experiments. However, there are still some limits of this pseudo-ZT framework, too. As we discussed in Section 2.4, the correlation between the two pseudo-ZTs is much less
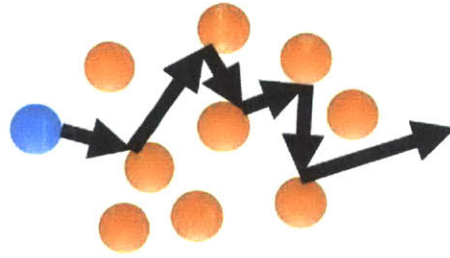
Scatterings in Transport Processes

● Scattering Center   ● Carrier

Carriers of Charges: Electrical Conductivity (σ)
Carriers of Heat: Thermal Conductivity (κ)
Carriers of Entropy: Seebeck Coefficient (S)

Figure 3.1: The Scheme of how the carriers of charge, heat and entropy are scattered by various scattering centers in a materials system. The scattering process is usually energy sensitive. The carriers with higher energy tends to be less scattered. The less scattering the carriers encounter, the more transport will occur. As the carriers carry electrical charge, heat and entropy, which leads to the macroscopic transport phenomena of electrical conductivity, thermal conductivity, and the Seebeck coefficient, respectively.

3.1 Introduction to Scattering Mechanism(s)

There are many different scattering mechanism(s) in different materials systems under different temperature conditions. Generally, a specific scattering mechanism at a certain temperature can be described by the carrier energy dependent scattering relaxation function [17, 25, 48],

$$\tau = \tau_0 \left(\frac{E}{k_B T} \right)^j, \qquad (3.1)$$

51

where τ is the relaxation time that is deduced by inversing the ensemble scattering rate $\left\langle \tau^{-1} \right\rangle$.

Here τ_0 is the scattering time coefficient, and its inverse $\left\langle \tau_0^{-1} \right\rangle$ denotes the scattering strength, which varies with materials system and temperature. E is the energy of carriers, where we have calibrated the energy at each band edge to be 0. j is the scattering order, which determines how sensitive the scattering time is to energy. In most cases, the carriers with higher energy E get scattered less, and thus, are transported more. The scattering order j is determined by the specific scattering mechanism(s), as discussed below.

3.1.1 Acoustic Phonon Scattering

When acoustic phonons are propagating in the lattice, the vibrations will cause the atoms to deviate from their original balancing points, which then lead to local lattice potential deformation. A lattice potential deformation is a deviation from the perfect periodicity for the electrons, and will effectively scatter the Bloch electrons, which is called the acoustic phonon scattering. We know that transverse phonons do not induce volume changes, so only longitudinal branches of acoustic phonons will scatter electrons. Under the small perturbation assumption, it is expected that the volume due to longitudinal acoustic change is proportional to the divergence of the displacement of these phonons, i.e. [48]

$$\Delta V_{AC} = D_{AC} \nabla \cdot \vec{u}, \tag{3.2}$$

where ΔV_{AC} is the volume change caused by the acoustic phonon, $\vec{u}$ is the displacement of the phonon, and D_{AC} is called the acoustic deformation potential. The scattering rate function under a specific acoustic deformation potential D_{AC} can be written as,

$$\frac{1}{\tau(E)} = \frac{\pi D_{AC}^2 k_B T}{\rho v_s^2 \hbar} D(E), \tag{3.3}$$

where ρ is the mass density of the lattice, v_s is the sound velocity, and $D(E)$ is the density of electronic states as a function of the carrier energy E.

3.1.2 Non-Polar Optical Phonon Scattering

Besides the acoustic phonons, where each unit cell moves as a whole, optical phonons can also scatter electrons, where each single atom in a unit cell can move at a given time in a different phase. Therefore, under the perturbation theory, the volume change should be directly proportional to the displacement of the phonon, rather than to the divergence of the displacement of the phonon, i.e. [49]

$$\Delta V_{OP} = D_{OP} \nabla \cdot \vec{u}, \qquad (3.4)$$

where ΔV_{OP} is the volume change caused by the optical phonon, $\vec{u}$ is the displacement of the phonon, and D_{OP} is called the optical deformation potential. Under high temperature conditions, the scattering rate function for non-polar optical phonon scattering can be given by,

$$\frac{1}{\tau(E)} = \frac{\pi^3 \hbar \sqrt{k_B T}}{\rho a^2} \left(\frac{E_0}{\hbar \omega_{OP}} \right)^2 D(E), \qquad (3.5)$$

where a is the lattice constant and ω_{OP} is the optical phonon frequency under the Einstein model.

3.1.3 Polar Optical Phonon Scattering

If the bonds between atoms within a unit cell are ionic, the longitudinal optical phonons will be polarized. The carrier scattering induced by this type of phonon is called the polar optical phonon scattering, which is the dominant scattering mechanism at high temperature in some ionic

semiconductors, like GaAs and InSb. The scattering rate function for polar optical phonon scattering is given by [49],

$$\frac{1}{\tau(E)} = \frac{2k_B T e^2}{\hbar^2 v}(\varepsilon_\infty^{-1} - \varepsilon_0^{-1}),$$ (3.6)

where ε_ω is the dielectric constant at frequency ω, and v is the carrier velocity.

3.1.4 Charged Impurity Scattering

If the carriers are scattered by the charged impurities, the carrier scattering time function can be given by [50],

$$\frac{1}{\tau(E)} = \frac{\pi}{8\hbar k^4}\left(\frac{4\pi Z e^2}{\varepsilon}\right)^2 N_D D(E),$$ (3.7)

where k is the lattice momentum, Z is the number of charge units per impurity center, ε is the static permeability and N_D is the concentration of charged impurities.

3.1.5 Piezoelectric Scattering

For piezoelectric scattering, the scattering rate function is given by [51],

$$\frac{1}{\tau(E)} = \frac{\pi \hbar k_B T}{\rho v_p^2 m}\left(\frac{e_{14} e}{2\varepsilon_0}\right)^2 D(E),$$ (3.8)

where v_p is a directionally averaged sound velocity, e_{14} is the piezoelectric constant, e is the elementary charge, and ε_0 is the vacuum dielectric constant [51].

3.2 Previous Scattering Inference Methods

One scattering mechanism(s) inference method popularly used is the electrical conductivity fitting method. The electrical conductivity (σ) and carrier concentration (N) are measured, and thereafter the average scattering time is estimated through [25]

$$\overline{\tau} = \frac{m^* \sigma}{Ne^2},$$

(3.9)

where m^* is the effective mass of the major carrier. This method is widely used because it is easy to understand and simple to carry out. However, this method only gives us an estimate of the average value of scattering time $\overline{\tau}$, but no information about the carrier energy dependence of the scattering time is given. Further, this method assumes that there is only one kind of carrier with an effective mass m^* that is contributing to the transport, which is not a typical case for most thermoelectric materials systems.

Another popularly used scattering time measurement is photon-carrier scattering measurement, for which we would shine laser beam onto a materials sample and we would measure the scattering time of carriers scattered by photons [52]. This method is a direct measurement of the scattering time, but it only measures the photon-carrier scattering time. Since the scattering rate function and its energy dependence can differ from mechanism to mechanism significantly. This method can therefore barely be used as a scattering mechanism inference tool.

3.3 Relating the Seebeck Coefficient to Scattering

I have found that the scattering order j in Equation (3.1) forms a one-to-one correspondence with the maximum value of the Seebeck coefficient for a specific electronic band structure. For example, without loss of generality, let us now consider a three-dimensional system where the effective mass of holes is, for example, 5 times larger than the effective mass of electrons. Let us further assume that the band gap is $E_g = 10k_B T$. The maximum values of the Seebeck coefficient for both N-type and P-type doping with different scattering mechanisms (different scattering orders) are shown in Figure 3.2 [53].
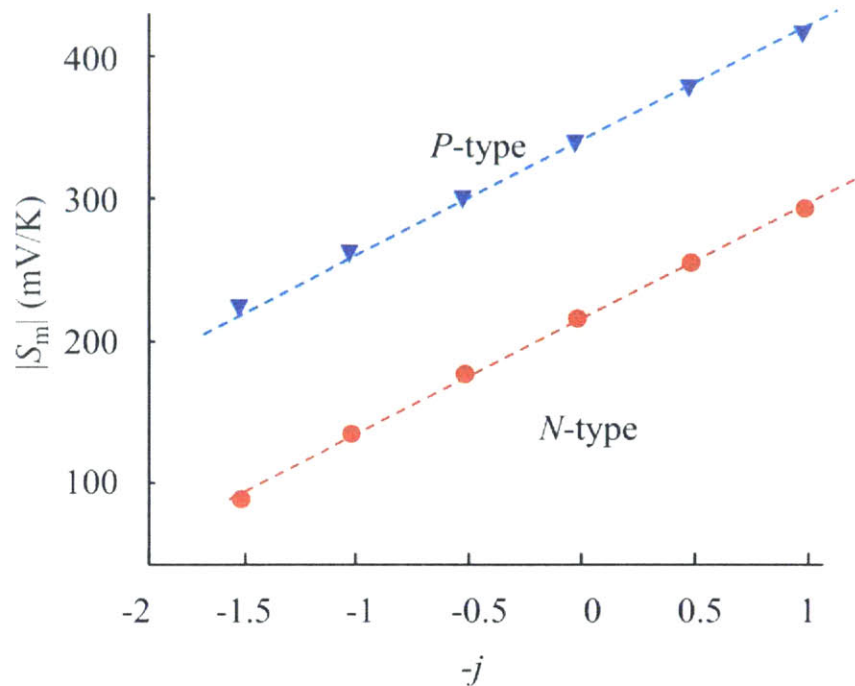
Figure 3.2: How the maximum values of the Seebeck coefficient, for both P-type and N-type materials, change in an almost linear manner with the scattering order j. Without loss of generality, here we illustrate a three-dimensional two-band system where the effective mass of holes is 5 times larger than the effective mass of electrons. The band gap is assumed to be

$E_g = 10k_B T$. Other materials systems have the similar relation between the maximum Seebeck coefficient and scattering order j.

It is clearly seen that though the Seebeck coefficient is determined by many factors, the maximum value of Seebeck coefficient is only a function of the scattering order j, which is almost a linear relation, when the band structure is given.

To prove this mathematically, we can examine this using the Boltzmann Equation. From Eq. (2.12) and (2.16) we know that the Seebeck coefficient for a single band valley is,

$$S\left(E_f\right) = \frac{1}{eT}\left(\frac{\int_0^\infty (\frac{E}{k_B T})^{2.5+j}\left(-\frac{\partial f}{\partial E}\right)_{E_f} dE}{\int_0^\infty (\frac{E}{k_B T})^{1.5+j}\left(-\frac{\partial f}{\partial E}\right)_{E_f} dE} - E_f \right) \tag{3.10}$$

In order to obtain the relation between the Seebeck coefficient S and the scattering order j, we first make a hypothesis that j for a specific band valley can be tuned artificially through certain ways, so we can take the derivative as,

$$\frac{\delta S\left(E_f\right)}{\delta j} = \frac{1}{eT}\left[(j+1) - j\left\{ \frac{\int_0^\infty E^{j+2.5}\left(-\frac{\partial f}{\partial E}\right)_{E_f} dE \int_0^\infty E^{j-0.5}\left(-\frac{\partial f}{\partial E}\right)_{E_f} dE}{(\int_0^\infty E^{j+1.5}\left(-\frac{\partial f}{\partial E}\right)_{E_f} dE)^2} \right\} \right] \tag{3.11}$$

It is not difficult to see that at the maximum value of the Seebeck coefficient

$$\frac{\delta S\left(E_f\right)}{\delta E_f} \to 0 \tag{3.12}$$

and

$$\frac{\int_0^\infty E^{j+2.5}\left(-\frac{\partial f}{\partial E}\right)_{E_f} dE \int_0^\infty E^{j-0.5}\left(-\frac{\partial f}{\partial E}\right)_{E_f} dE}{(\int_0^\infty E^{j+1.5}\left(-\frac{\partial f}{\partial E}\right)_{E_f} dE)^2} \to 1, \tag{3.13}$$

so

$$\frac{\delta S_{\max}\left(E_f\right)}{\delta j} \approx \frac{1}{eT} \tag{3.14}$$

Thus, we can see that the maximum Seebeck coefficient have a linear relation of j,

$$S_{\max} \approx \frac{j}{eT} + S_{\max,j=0} \tag{3.15}$$

Therefore, we have proved both physically and mathematically that the maximum values of Seebeck coefficient and the scattering order has a linear relation, and form a one-to-one correspondence.

3.4 New Scattering Inference Method

To infer a scattering mechanism based on Equation (3.1), there are two parameters that we need to know: the scattering strength $1/\tau_0$ and the scattering order j. Since we discovered in Section 3.3 that the scattering order can be inferred from the maximum values of Seebeck coefficient, and we also know that the scattering strength can be interpreted from the electrical conductivity measurement, these will provide us with a new scattering mechanism inference method.

First, we measure the maximum values of the Seebeck coefficient along with the electrical conductivity. Second, we use the measured data to extract the scattering strength $1/\tau_0$ and scattering order j, which we can then recover the scattering time function as in Equation (3.1). Finally, since the scattering time function is determined by the specific scattering mechanism(s) as discussed in Section 3.1, the scattering mechanism(s) can be revealed. The whole procedure is shown in Figure 3.3 [53].
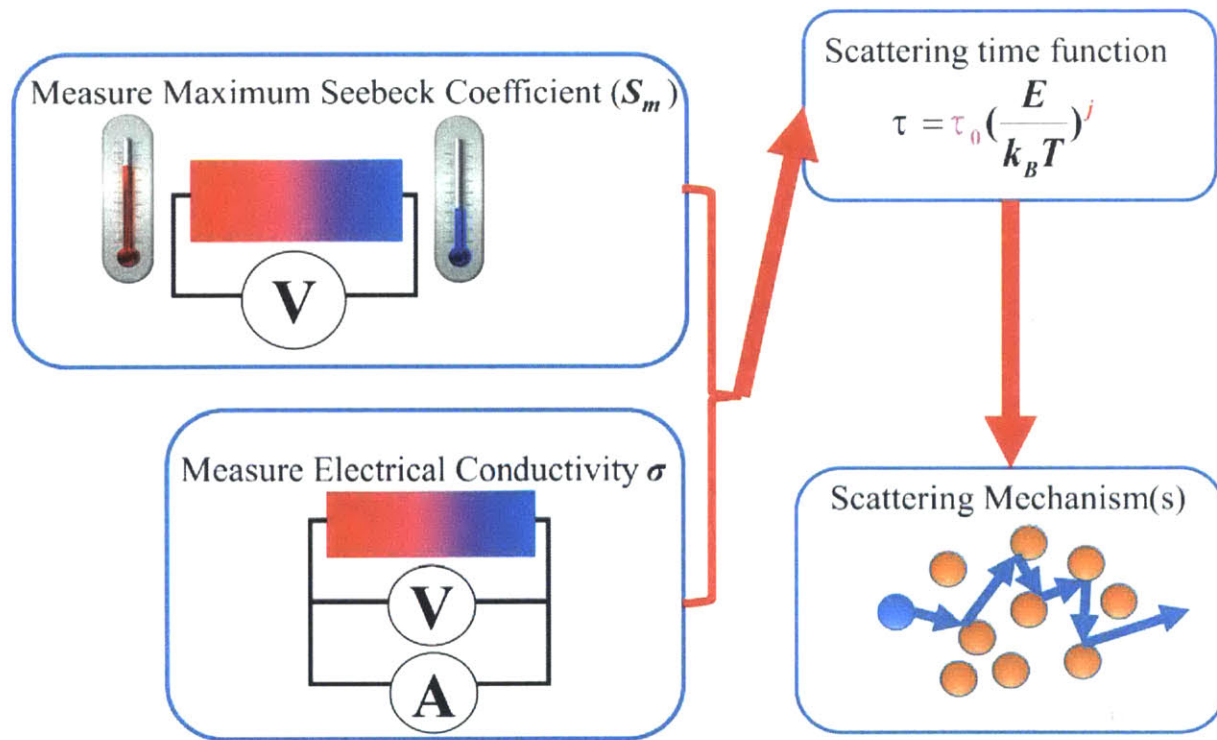
Figure 3.3: Scheme of the newly proposed method of scattering mechanism(s) inference.

3.5 Application in Graphene

In reality, the band structures of typical thermoelectric materials are very complicated, so it is reasonable to first test this new methodology on a materials system with a simple band structure, which is also easy in carrying out the electrical conductivity and the Seebeck coefficient measurements.

One suitable materials system for such an example is graphene. Graphene is a single layer of carbon atoms as shown in Figure 3.4. Therefore, the electronic band structure of graphene is also two-dimensional. Near the Fermi level, the bottom of the conduction band and the top of the valence band touch each other at the K point and the K' points in the first Brillouin zone. The energy band form two isotropic linearly dispersed bands, i.e. Dirac cones, as shown in Figure 3.4[54, 55].
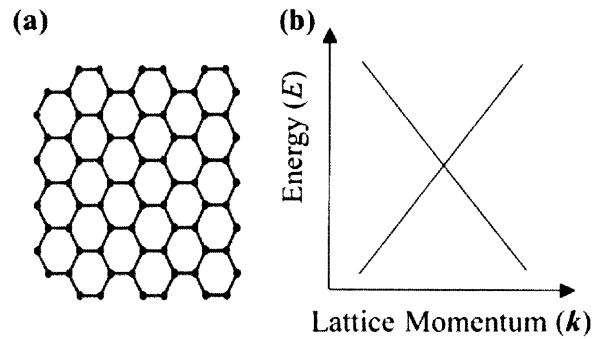
Figure 3.4: Scheme of the atomic structure (left) and the electronic band structure (right) of graphene, a single layer of carbon atoms.

The values of the maximum Seebeck coefficient at different temperatures for graphene have been measured by Zuev *et al.* [56] through a gated thermoelectric device by changing the Fermi level, and these results are summarized in Table 3.1.

Table 3.1: Measured Maximum Seebeck Coefficient for the Dirac Cone Carriers in Graphene [56]

Temperature (K)	300	150	80	40
Experimental Maximum *P*-type Seebeck coefficient (μV/K)	92.52	57.94	33.64	14.95
Experimental Maximum *N*-type Seebeck coefficient (μV/K)	-59.81	-39.25	-24.30	-10.28

Based on the data in Table 3.1, we are able to extract the scattering order j and the scattering time asymmetry ratio between the electrons and the holes $\tau_0^{Electron} / \tau_0^{Hole}$ at different temperatures, as shown in Figure 3.5 [53].
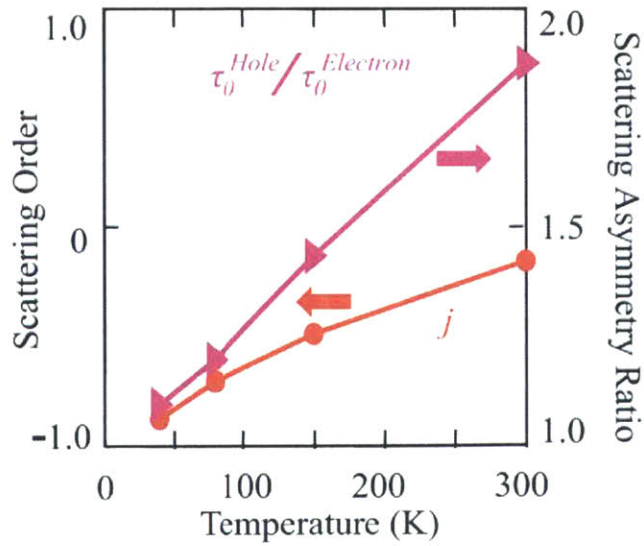
Figure 3.5: The results of the scattering order j for graphene carriers, and the scattering time asymmetry ratio $\tau_0^{Electron} / \tau_0^{Hole}$ as a function of temperature. The experimental measurement has been carried out by Zuev *et al.* [56] on a graphene sample sitting on a silicon dioxide substrate. It can be seen that as the temperature increases from the cryogenic range to the room temperature range, the scattering order (red curve) increases from $\sim$ -1 to $\sim$0, and the scattering time asymmetry ratio (red curve) increases from $\sim$1 to $\sim$2.

We see that the scattering order j changes significantly with temperature, which implies that the carrier scattering mechanism is very temperature sensitive. At the low temperature end, $j \rightarrow -1$, which implies that $\tau^{-1} \propto D(E)$. This means that in the cryogenic temperature range the scattering due to acoustic phonons and the scattering due to the roughness of the surface are the dominant scattering mechanisms for the carriers. When temperature increases, $j \rightarrow 0$, which implies that the ripple scattering of the surface and the charged center scattering become as important as the acoustic phonon scattering at room temperature. Another important trend we see from Figure 3.5 is that the asymmetry ratio of scattering strength $\tau_0^{Electron} / \tau_0^{Hole}$ increases with temperature, and the conduction band and the valence band are close to symmetric at a cryogenic temperature as low as 40 K. These results are summarized in Table 3.2.

Table 3.2: Graphene Carrier Scattering Properties at Low and Room Temperature

T	Scattering	Asymmetry
low	surface roughness, acoustic phonon, ...	low

room	thermal ripples, charged impurities become important	high

To further verify this model, I calculated the electrical conductivity and compared it with experimental measured values, as shown in Figure 3.6 [53, 56].
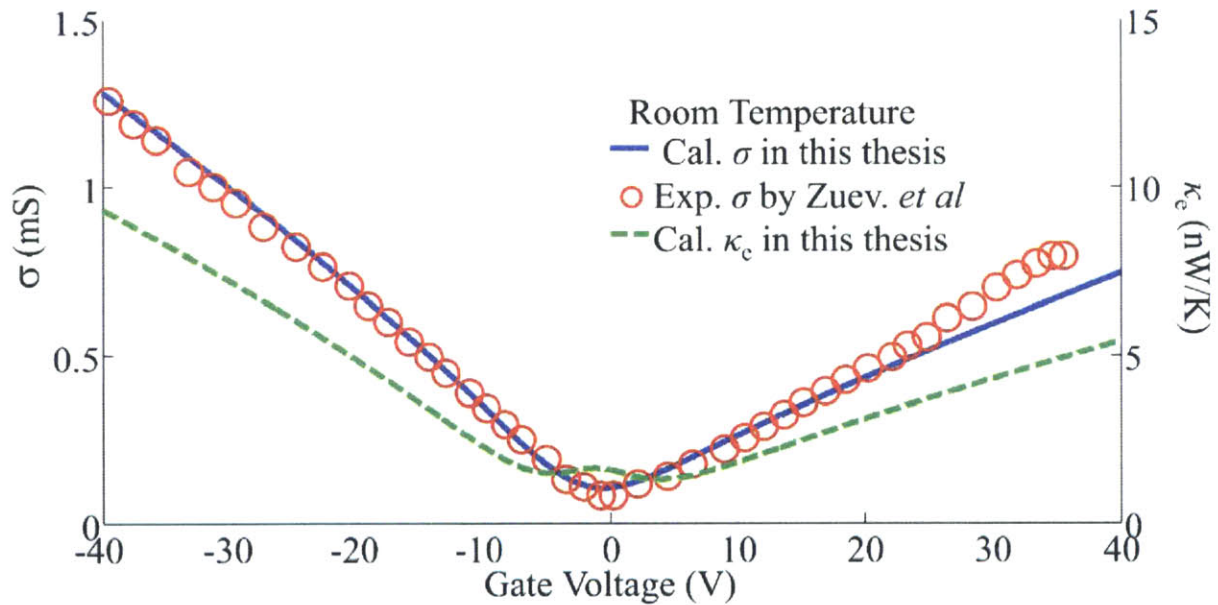
Figure 3.6: The calculated electrical conductivity (blue solid line) for graphene associated with two isotropic Dirac cones at 300 K is compared with the experimental measured values (red circles), which exhibit very good consistency. The associated electronic thermal conductivity is also calculated (green dashed line), and is consistent with the empirical estimation [57].

The calculated electrical conductivity (blue solid line) based on this model and the experimentally measured electrical conductivity (red circles) are compared for the room temperature experimental conditions. The consistency of the calculated data and measured data has been shown in Figure 3.6. Further, the electronic contribution to the thermal conductivity of graphene (green dashed line) is also calculated.

3.6 Seebeck Coefficient Enhancement

From the results in Section 3.3 and 3.4, we can see that though the Seebeck coefficient is related to the scattering strength, carrier concentration, and other conditions at a certain temperature, the possible maximum values of the Seebeck coefficient for both N-type and P-type materials are mainly decided by the scattering order, and hence the scattering mechanism(s), for a given electronic band structure. This has adjusted our thoughts on how to enhance the power density of a thermoelectric materials system by maximizing the Seebeck coefficient, i.e. by changing into higher order scattering mechanism(s). For example, we expect to see an enhanced maximum Seebeck coefficient by introducing more charged scattering centers to an acoustic phonon scattering dominated system, or by reducing neutral impurity scattering centers to avoid such low order scattering mechanism.

3.7 Demonstration in Other Materials Systems

Besides the graphene system, the metal dichalcogenide monolayer materials system is another class of materials that are interesting to researchers currently. The similar experiments carried out on the graphene system can be carried in the metal dichalcogenide monolayer materials systems as well, including the gate voltage [29], the surface functionalization [30], and the adatoms absorption[31-41].

64

From Figure 3.7 we see that the maximum values Seebeck coefficient still changes with the scattering order j in the various metal dichalcoginide monolayer materials systems [29-41]. This is consistent with the mathematical predictions we made for a general electronic band in Equations (3.11)-(3.14). This one-to-one correspondence relation between the maximum Seebeck coefficient and the scattering order can be used as a diagnostic tool for carrier scattering mechanism(s).
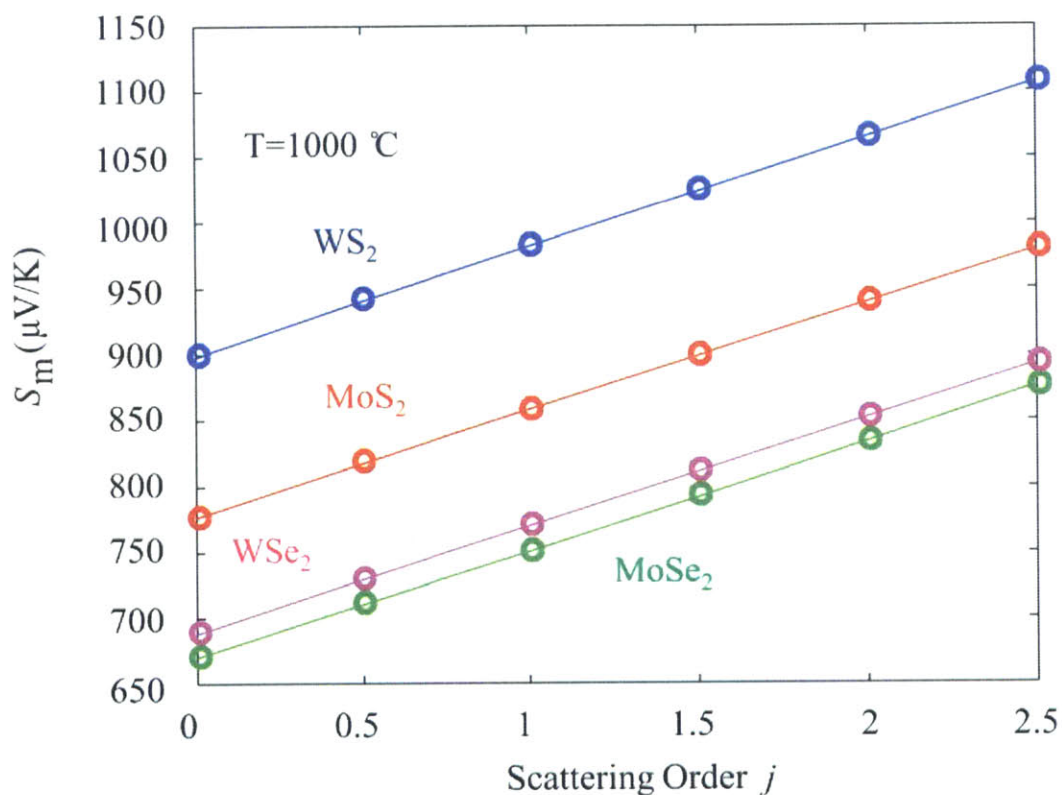
Figure 3.7: How the maximum values of the Seebeck coefficient changes in an almost linear manner with the scattering order j in the various metal dichalcoginide monolayer materials systems [29-41].

3.8 Chapter Summary

In this chapter, it is found that when the electronic band structure is given, the maximum Seebeck coefficient for a materials system, both P-type and N-type, forms a one-to-one correspondence with the scattering order, described by Equation (3.1). This result has provided us with a scattering mechanism inference tool, as well as a Seebeck coefficient enhancement strategy. This new method is tested and verified in graphene, which is a system with a simple linearly dispersed band structure. The mathematically predicted results in Section 3.3-3.5 are also demonstrated in the metal dichalcoginide monolayer materials systems as well. Therefore, it is significantly promising that this method will also work for more complicated thermoelectric materials systems.

Chapter 4

New Model for Nano-Narrow-Gap Materials

Narrow-gap materials refer to semiconducting materials with a band gap E_g that is comparable to the range of its operation temperature T, i.e. $E_g \sim k_B T$. Most of the traditional good-performance thermoelectric materials fall into this materials class, e.g. bismuth antimony alloys ($Bi_{1-x}Sb_x$), lead telluride (PbTe), bismuth telluride (Bi_2Te_3), bismuth selenide (Bi_2Se_3), and lead selenide (PbSe) [17].

4.1 Introduction to Nano-Narrow-Gap Materials

Besides the application in thermoelectric power generation and refrigeration, especially for low temperature cooling, narrow-gap materials are also widely used for infrared photonic devices,

---

This Chapter is reprinted/adapted from the published work: [a] S. Tang and M. Dresselhaus, "Phase diagrams of BiSb thin films with different growth orientations", *Physical Review B*, **86**, 075436 (2012). [b] S. Tang and M. Dresselhaus, "Electronic phases, band gaps, and band overlaps of bismuth antimony nanowires", *Physical Review B*, **89**, 045424 (2014).

terahertz electronics and photon absorbers [58-60]. By introducing nanoscience and nanotechnology, we have more parameters available for controlling the electronic and photonic properties in nanostructured narrow-gap materials, including thin films, nanowires, nanoedges, and nano-composites.

The modeling of the electronic band structure for nano-narrow gap materials has been always a challenge. On the one hand, in a narrow gap system, the conduction band and the valence band are strongly coupled to each other; on the other hand, in a nanoscale confined system, the band gap will be changed due to the quantum confinement effect, which is determined by the band gap and the band shape near the band-edges. Thus, in such a nanoscale narrow-gap system, the band gap, the dispersion, the carrier effective mass and the quantum confinement effect are intertwined. Though the effective mass theorem and the $k \cdot p$ theory can give a simple estimation of the band structure, the accuracy of the effective mass and band gap determination is usually not sufficiently accurate. For accurate results, first principles calculations can be carried out, which, however, require very large memory and computational power when it comes to nanoscale alloy systems that need to contain hundreds or thousands of atoms within each unit cell. Thus, a new approach that is more accurate than the effective mass theorem and more efficient than the first principle calculations needs to be developed.

4.2 New Method to Model the Band Structure

In this thesis, I mainly studied the nanomaterials of bismuth antimony ($Bi_{1-x}Sb_x$) alloys, which is a very important materials system for low temperature thermoelectric applications. We will illustrate here a new method to model the band structure of nano-narrow-gap materials in nanostructured $Bi_{1-x}Sb_x$ alloys.

We recall that $Bi_{1-x}Sb_x$ alloys have a rhombohedral lattice structure with two atoms in each unit cell, where the trigonal axis with C_3 symmetry, the binary axis with C_2 symmetry, and the bi-sectrix axis with C_1 symmetry that is perpendicular to the trigonal-binary plane, form a natural Cartesian coordinate system. The bisectrix axis and the trigonal axis form a mirror plane that bisects the whole rhombohedral lattice, as shown in Figure 4.1 (a) [58-61].
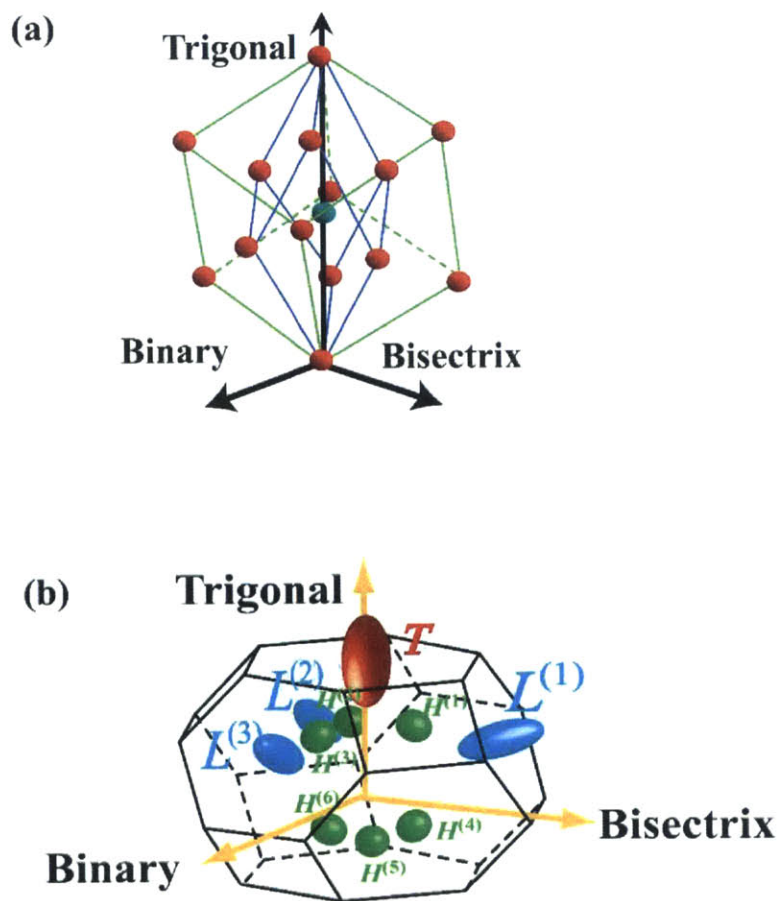
Figure 4.1: Structure of $Bi_{1-x}Sb_x$. (a) shows the rhombohedral lattice structure of bulk bismuth, bulk antimony and their alloys $Bi_{1-x}Sb_x$. There are two atoms in each unit cell. The C_3 symmetry trigonal axis, the C_2 symmetry binary axis and the C_1 symmetry bisectrix axis form a Cartesian coordinate system in three-dimensional space. The trigonal-bisectrix plane forms a

mirror symmetry plane. (b) shows different carrier-pockets in the first Brillouin zone of bulk $Bi_{1-x}Sb_x$.

In the first Brillouin zone of bulk $Bi_{1-x}Sb_x$, there are one T point, three degenerate L points (labeled as $L^{(i)}$, i =1,2,3) and six degenerate H points (labeled as $H^{(i')}$, i' =1,2...6), as shown in Figure 4.1(b). The bottom of the conduction band is located at the three L points. The top of the valence band can be located at the T point, the three L points or the six H points, depending on the antimony composition x. Figure 4.2 shows how the band-edges for different carrier-pockets change with antimony composition x in bulk $Bi_{1-x}Sb_x$ alloys, which leads to different phases: a semi-metal phase, an indirect-semiconductor phase and a direct-semiconductor phase. In the cryogenic temperature range below 77 K, the electronic band structure does not change notably with temperature.
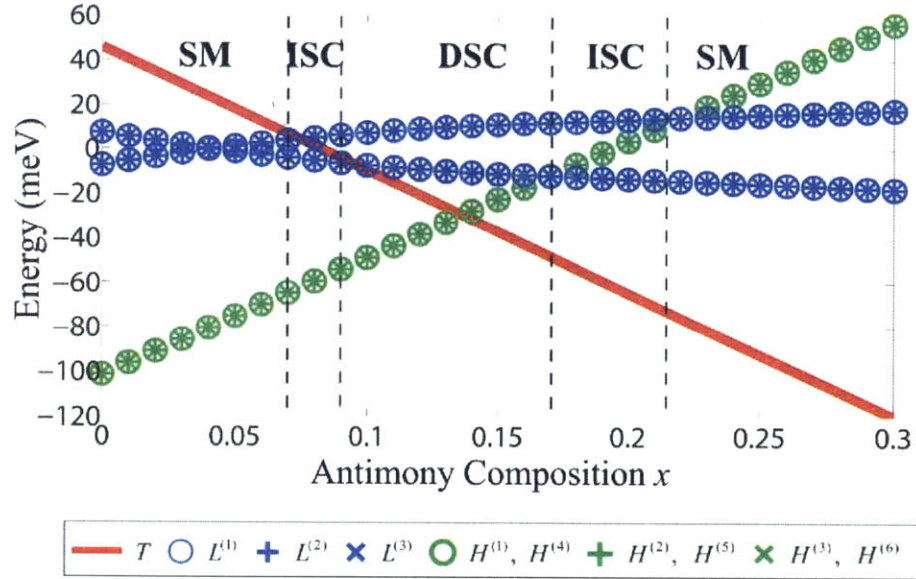
Figure 4.2: Band-edge energies at different carrier-pockets vs. antimony composition x for bulk $Bi_{1-x}Sb_x$. The semi-metal (SM) phase regions, the indirect-semiconductor (ISC) phase regions

and the direct semiconductor (DSC) phase region are labeled. The symbols for the various bands are indicated by the colors and symbols in the bar below the plot [58-62].

In a nanosystem, e.g. a thin film system, there is an electron carrier-pocket as well as a hole carrier-pocket at each of the $L^{(i)}$ points. The $L^{(i)}$-point conduction band-edge and valence band-edge energies are close to one another, and therefore these bands are strongly coupled to each other, so that the dispersion relations are non-parabolic or perhaps even linear if Dirac cones are formed. The normal-to-the-film components of the inverse-effective-mass tensor $\alpha^L_{\perp[Film]}$ and the $L^{(i)}$-point band gap $E^L_{g[Film]}$ depend on the film thickness, and $\alpha^L_{\perp[Film]}$ and $E^L_{g[Film]}$ are mutually coupled terms, which are both unknown. To calculate the $L^{(i)}$-point band-edge shift, we start from the traditional $k \cdot p$ model [63, 64]

$$\mathbf{p} \cdot \boldsymbol{\alpha}^L \cdot \mathbf{p} = E(\mathbf{k})\left(1 + \frac{E(\mathbf{k})}{E^L_g}\right) \tag{4.1}$$

where $\boldsymbol{\alpha}^L$ is the L-point inverse-effective-mass-tensor. Generally, the relation between $\boldsymbol{\alpha}^L$ and E^L_g around an L point is described as [65, 66]

$$\boldsymbol{\alpha}^L = \frac{2}{\hbar^2}\nabla^2 E(\mathbf{k}) = \frac{1}{m_0}\mathbf{I} \pm \frac{1}{m_0^2}\frac{2}{E^L_g}\mathbf{p}^2, \tag{4.2}$$

under the $k \cdot p$ regime, where $\mathbf{I}$ is the identity matrix and m_0 is the free electron mass. Further, under first order perturbation, the relation between the inverse-effective mass tensor and the band gap, has been shown to be [65-68]

$$\boldsymbol{\alpha}^L_{[Film]}\left(Bi_{1-x}Sb_x\right) = \frac{E^L_{g[Bulk]}\left(Bi\right)}{E^L_{g[Film]}\left(Bi_{1-x}Sb_x\right)} \cdot \left(\boldsymbol{\alpha}^L_{[Bulk]}\left(Bi\right) - \frac{1}{m_0}\mathbf{I}\right) + \frac{1}{m_0}\mathbf{I}, \tag{4.3}$$

71

both theoretically and experimentally in previous literature. Lastly, the band gap change due to the quantum confinement is usually described by the square well model [25],

$$\Delta E^L_g = \frac{\pi^2 \hbar^2 \alpha^L_{\perp[Film]}}{l^2_\perp}.$$ (4.4)

We now iterate Equation (4.1)-(4.4) dynamically, and use the band gap and effective mass of bulk bismuth as the initial conditions, to get the ultimate converged results for $Bi_{1-x}Sb_x$ films, The detailed flow chart for this dynamical-iteration model is shown in Figure 4.3 [69-71].
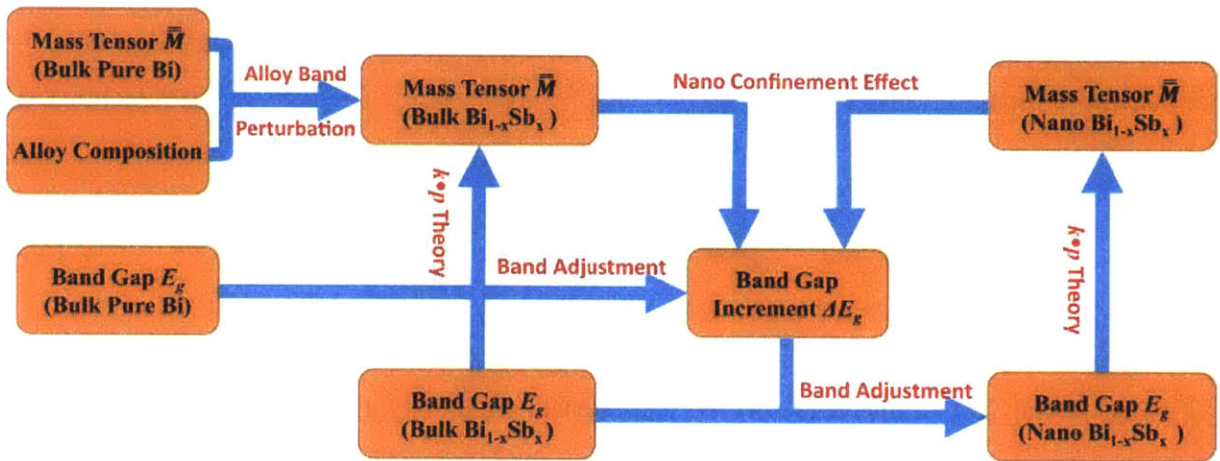
Figure 4.3: Scheme of the flow chart of how the band structure of nano-$Bi_{1-x}Sb_x$ is calculated through dynamically adjusting the band gap, band shape and quantum confinement. Here the effective mass tensor $\overline{\overline{M}}$ is the inverse of the aforementioned α^L

4.3 Bi$_{1-x}$Sb$_x$ Thin Films

The electronic band structure properties of $Bi_{1-x}Sb_x$ thin films are studied under the newly developed model. Due to the anisotropy of $Bi_{1-x}Sb_x$ thin films, the growth orientation has a remarkably strong influence on the symmetry properties of the various carrier pockets that will be created in these thin films and the electronic band structure, which will in turn affect the band structure. The symmetry properties of the carrier pockets and their influence on the band structure are illustrated in Figure 4.4, for three typical growth orientations [69, 71].

Trigonal Oriented Growth   Bisectrix Oriented Growth   Binary Oriented Growth

(a)   (b)   (c)

(d)   (e)   (f)

Antimony Composition x

Energy (meV)

Legend: T $\bigcirc$ $L^{(1)}$ $+$ $L^{(2)}$ $\times$ $L^{(3)}$ $\bigcirc$ $H^{(1)}, H^{(4)}$ $+$ $H^{(2)}, H^{(5)}$ $\times$ $H^{(3)}, H^{(6)}$
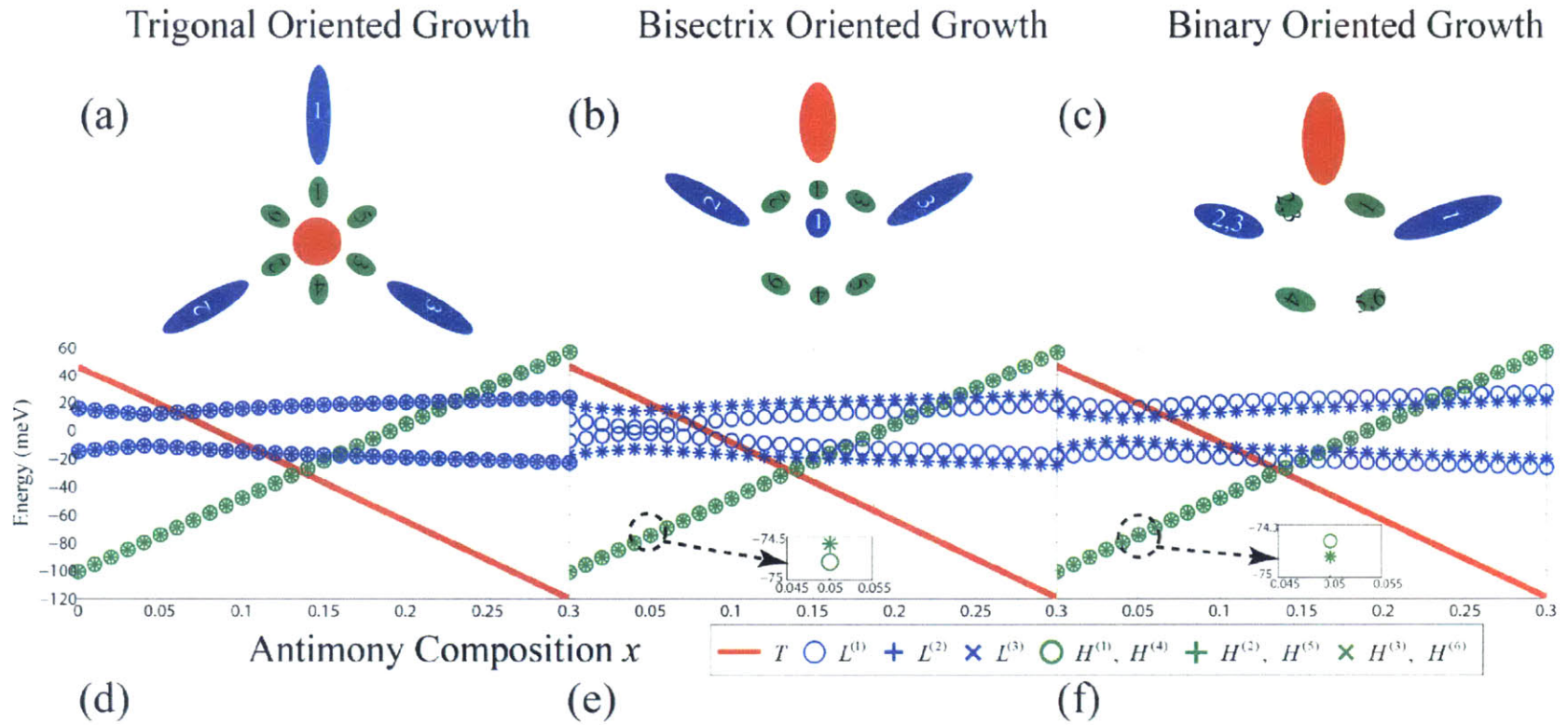
Figure 4.4: Schemes of the symmetry properties of the T-point (red), L-point (blue) and H-point (green) carrier pocket projections onto the film plane for $Bi_{1-x}Sb_x$ thin films for the (a) trigonal, (b) bisectrix and (c) binary growth orientations. How such symmetry properties affect the relation of band-edge energy as a function of Sb composition is illustrated for 100 nm thick $Bi_{1-x}Sb_x$ thin films of (d) trigonal, (e) bisectrix and (f) binary growth orientations.

Figures 4.4 (a)-(c) show the carrier pockets of $Bi_{1-x}Sb_x$ thin films obtained by projecting the T point, the three L points and the six H points onto the film plane for different growth orientations. These figures, as illustrated in Fig. 4.4 (d)–(f), also show the symmetry properties of these projected carrier pockets, where the 100 nm thick films are chosen as examples.

The case of the thin films oriented along the trigonal axis is shown in Figures 4.4(a) and (d), where the C_3 symmetry of the three L-point carrier-pocket projections is retained, and where the C_6 symmetry and the inversion symmetry of the six H-point carrier-pocket projections are also retained. Thus, the bottom (top) of the conduction (valence) band is degenerate in energy at $L^{(1)}$, $L^{(2)}$, and $L^{(3)}$, and so is the top of the valence band at $H^{(1)}$, $H^{(2)}$, $H^{(3)}$, $H^{(4)}$, $H^{(5)}$, and $H^{(6)}$.

The case of the thin films oriented along the bisectrix axis is shown in Figures 4.4 (b) and (e). The $L^{(2)}$-, the $H^{(2)}$-, and the $H^{(5)}$- point projections all have mirror symmetry with respect to the $L^{(3)}$-, the $H^{(3)}$-, and the $H^{(6)}$- point projections, respectively. The inversion symmetry of the H points is still retained in Figures 4.4 (b) and (e). Figure 4.4 (e) shows that the bottom (top) of the conduction (valence) band at the $L^{(2)}$-point and the $L^{(3)}$-point projections are degenerate in energy, but are higher (lower) in energy than the $L^{(1)}$-point projection. The inversion symmetry ensures that the $H^{(i)}$ point is still degenerate in energy with respect to the $H^{(i'+3)}$ points ($i' = 1, 2,$ or 3).

The case of the binary oriented thin film is shown in Figure 4.4 (c) and (f). The $L^{(2)}$-point projection and the $L^{(3)}$-point projection overlap, and are different from the $L^{(1)}$-point projection. The inversion symmetry of the H points is still retained. Meanwhile, the $H^{(2)}$- ($H^{(4)}$-) point carrier-pocket projections and the $H^{(3)}$- ($H^{(5)}$-) point carrier-pocket projections overlap with each

other and are different from the $H^{(1)}$- ($H^{(6)}$-) point carrier-pocket projections. The inversion symmetry ensures that the $H^{(i')}$ point is degenerate in energy with the $H^{(i'+3)}$ point ($i' = 1, 2,$ or 3).

The electronic phase diagram as a function of film thickness l and of antimony composition x for the $Bi_{1-x}Sb_x$ thin-film system grown normal to the trigonal, bisectrix and binary axes are shown in Figure 4.5 (a), (b) and (c), respectively.

(a) Trigonal Oriented Growth (b) Bisectrix Oriented Growth (c) Binary Oriented Growth

Film Thickness l (nm)

Antimony Composition x

(d) (e) (f)

Band Gap or Band Overlap (meV)
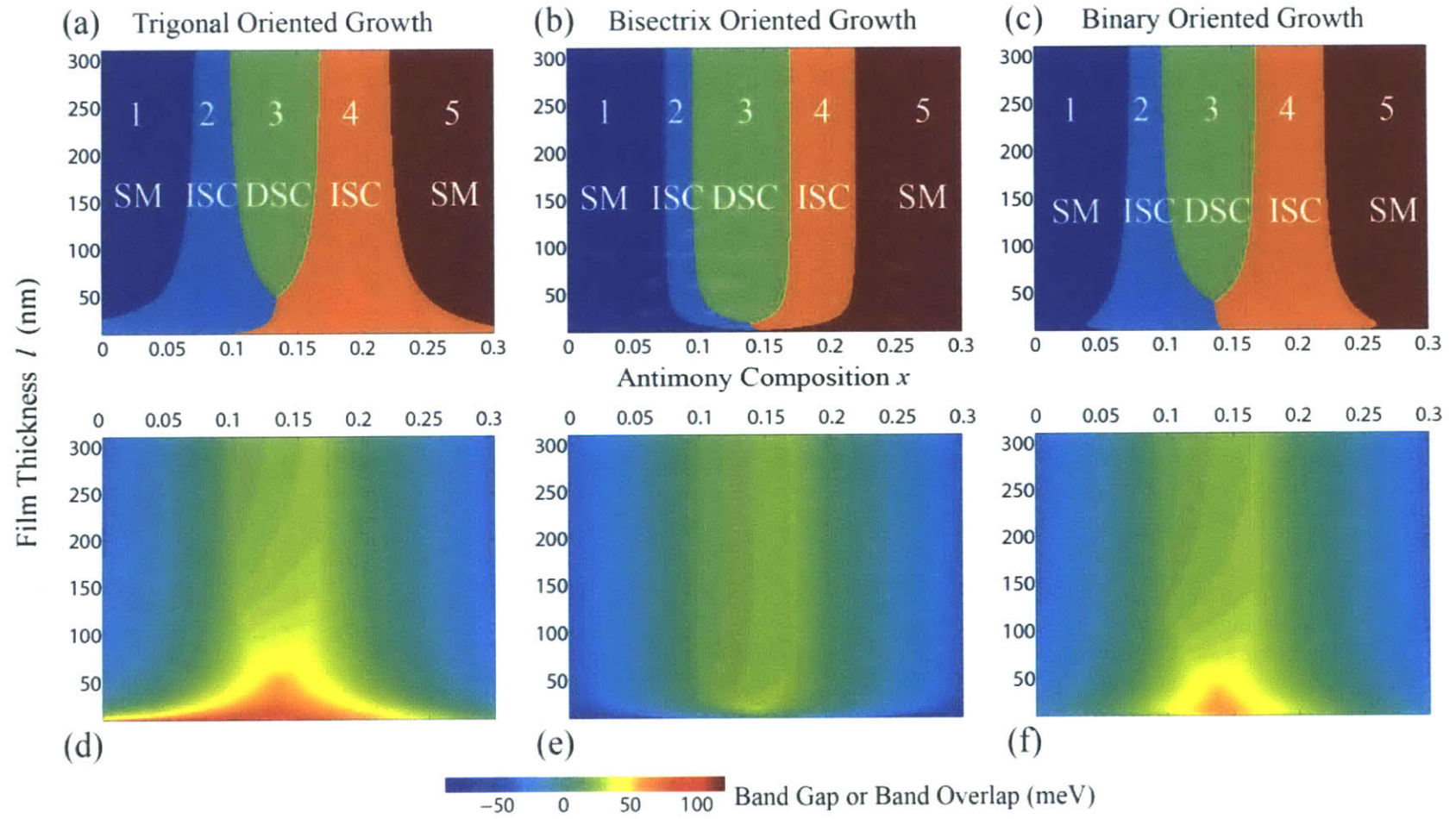
Figure 4.5: Phase diagrams for the $Bi_{1-x}Sb_x$ thin-film systems grown normal to (a) the trigonal axis, (b) the bisectrix axis, and (c) the binary axis, as a function of antimony composition x and film thickness l. The band gap/overlap map shown in (d), (e), and (f), are corresponding to (a), (b), and (c), respectively. A positive value stands for a band gap, a negative value stands for a band overlap, and a zero value stands for a gapless state [69, 71].

Region 1 and Region 5 are the semimetal phases, Region 2 and Region 4 are the indirect-gap semiconductor phases, and Region 3 is the direct-gap semiconductor phase. The top of the valence band is located at the T point for Region 1 and for Region 2, at the H points for Region 4 and Region 5, and at the L points for Region 3. The overall band-gap (positive) or band overlap (negative) as a function of film thickness and Sb composition is shown in Figure 4.5 (d)-(f).

These results for the maps of the electronic phases, and the band gap/overlap magnitudes have provided the guidance for the synthesis of interesting $Bi_{1-x}Sb_x$ thin films. The differences between the model and the experiments are of urgent interest. Based on the progress of the understanding of this class of materials, future research should be focused on how to engineer $Bi_{1-x}Sb_x$ thin films for specific functional applications. For cryogenic thermoelectrics, the controllability of the mini-band-gap at the L point and of the quasi-Dirac cones can provide new thoughts about how to increase the Seebeck coefficient, while maintaining the ultra-high mobility of the Dirac carriers or quasi-Dirac carriers in the $Bi_{1-x}Sb_x$ system, which could give a remarkable increase to both the overall performance of thermoelectric generators and their super-cooling in the cryogenic range. Furthermore, the thirteen carrier pockets can be arranged in much more ways in thin films $Bi_{1-x}Sb_x$ than in bulk $Bi_{1-x}Sb_x$, so that the carrier concentration can be engineered with more flexibility.

4.4 $Bi_{1-x}Sb_x$ Nanowires

The electronic band structure properties of $Bi_{1-x}Sb_x$ nanowires are also studied under the newly developed model [70, 71]. Figure 4.6 illustrates the electronic phase diagrams and band

gap/overlap of $Bi_{1-x}Sb_x$ nanowires with d=100 nm, as a function of growth orientation and stoichiometry. The illustrations are made for the growth orientation within the binary plane, the trigonal plane and the bisectrix plane, in Figure 4.6 (a), (b) and (c), respectively. The semimetal (SM) phase regions, indirect semiconductor (ISC) phase regions and the direct semiconductor (DSC) phase regions are marked for each orientation. The Sb composition x is denoted by the radius of the circles in Figure 4.6. With a 100 nm wire width, it can be seen that the electronic phase starts from a semimetal, where the top of the valence band edge is located at the T point, at x=0. As the Sb composition increases, phase changes occur. Explicitly, the electronic phase changes from a semimetal to an indirect semiconductor with the top of the valence band edge located at the T point, too. At around x=0.15, the top of the valence band edge become located at an L point, and the electronic phase becomes a direct semiconductor. For yet higher Sb concentration x, the top of the valence band edge is shifted to an H point, and the band gap of the semiconductor phase becomes indirect again. When x is further increased, the electronic phase finally is changed back to a semimetal, only with the top of the valence band edge located at an H point.

This is seen more clearly in the maps of the band gap/overlap as a function of growth orientation and Sb composition, in the corresponding subfigures below, i.e. in Figure 4.6 (d), (e) and (f), for the binary plane, the trigonal plane and the bisectrix plane, respectively. A negative value stands for a band overlap, while a positive value stands for a band gap. A zero value denotes the gapless state. At Sb composition x=0, the band overlap exhibits a negative value corresponding to the semimetal phase. As x is increased, the magnitude of the band overlap starts to decrease, and then becomes zero, beyond which the band overlap disappears and the nanowire exhibits a band gap with a positive value, and the band gap increases with increasing Sb composition x. At around x=0.15, the band gap starts to decrease with increasing Sb composition x, until the band gap reaches zero. At yet a higher Sb composition x, a band overlap with a negative value appears again, indicating the onset of a semimetallic phase at the relatively Sb rich side of the phase diagram.

The anisotropic properties of bulk bismuth antimony phases are reflected in the symmetry properties of the electronic phase diagrams and the band gap/overlap diagrams, when the growth orientation lies in different crystallographic planes, or normal to different crystallographic directions. The diagrams of Figure 4.6 (a), (b) and (c) have similar profiles, but are actually different in their detailed shapes at each phase boundary, if they are examined more closely. The binary crystalline plane has inversion symmetry but not mirror symmetry. The inversion symmetry is reflected in Figure 4.6 (a) and (d). However, at this specific wire width (100 nm), the contrast associated with the anisotropy is not strong, and the non-existence of mirror symmetry is not obvious. We discuss below how quantum confinement helps to enhance the contrast of the anisotropy in the electronic phase diagrams and the band gap/overlap diagrams, and also how quantum confinement causes the mirror symmetry to disappear for the diagrams associated with the binary crystalline plane. When all six H-point hole-pockets, all six L-point half-hole-pockets and all six L-point half-electron-pockets are projected onto the trigoanl plane, a six-fold symmetry is formed, which is a higher symmetry than the three-fold symmetry of the trigonal axis in the bulk materials. This is reflected in the electronic phase diagram of Figure 4.6 (b), and in the band gap/overlap phase diagram of Figure 4.6 (e). In Figure 4.6 (b), the shape of each phase boundary is actually a mixture of a circle and hexagon. To see this, it requires a very careful reading of the diagram, and it might be not obvious. However, this circle and hexagon are much more clear in the band gap/overlap diagram in Figure 4.6 (e), where the shapes of six-petal flowers can best be seen at the edge of the inner yellow DSC (direct semiconductor phase) region. The diagrams of the bisectrix crystalline plane have both mirror symmetry about the binary axis, and mirror symmetry about the trigonal axis, which are accompanied by inversion symmetry. These symmetry properties are seen in Figure 4.6 (c), and are more obviously seen in Figure 4.6 (f).

Figure 4.6: The electronic phase diagrams (a)-(c), and the band gap/overlap diagrams (d)-(f) of $Bi_{1-x}Sb_x$ nanowires of 100 nm wire width, as shown for various wire growth orientations and Sb compositions x. The illustrations are made for the binary (a) and (d), trigonal (b) and (e), as well as and bisectrix (c) and (f) crystalline planes. In each diagram, the direction stands for growth orientation, and the length of radius for a point stands for the Sb composition x, which lines up with the origin of each circularly shaped diagram, so that the binary direction in (a) for example denotes the direction normal to the trigonal and bisectrix directions shown for the square sample faces. At the origin, the value of x is 0, and at the outmost point, the value of x is 0.30, as scaled in the legend. The regions with the semimetal phase (SM), indirect semiconductor phase (ISC) and direct semiconductor phase (DSC) are marked out in (a)-(c) and in the legend. In the legend of the phase regions, the top of the valence band edge is located at the T point for the upper regions of the semimetal (Region 1) and indirect semiconductor phases (Region 2), and is located at the H points for the lower regions of the indirect semiconductor phase (Region 4) and semimetal phase (Region 5). Both the top of the valence band edge and the bottom of the conduction band edge are located at the L points for the direct semiconductor phase (Region 3).

In the diagrams of the band gap/overlap, a positive value stands for a band gap, while a negative value stands for a band overlap. A zero value stands for a gapless state [70, 71].

Now we illustrate the electronic phase diagrams and band gap/overlap diagrams of $Bi_{1-x}Sb_x$ nanowires with a much stronger quantum confinement effect, occurring in nanowires with a small width, explicitly for a nanowire with a width of 10 nm. The small width nanowires show more clearly how the quantum confinement effect influences the symmetry properties and the electronic phases of the nanowires comparatively. The electronic phase diagrams and band gap/overlap of $Bi_{1-x}Sb_x$ nanowires with d=10 nm, as a function of growth orientation and stoichiometry, are illustrated in Figure 4.7. The changes in the electronic phase diagrams are more obvious in Figure 4.7 than in Figure 4.6. First, the direct semiconductor phase regions have disappeared in all of the three cases (a), (b) and (c). The semimetal phase region (dark blue), where the top of the valence band edge is located at the T point, has significantly shrunk to a tiny size in both Figure 4.7 (a) and (c), and has disappeared in Figure 4.7 (b). The semimetal phase region where the top of the valence band edge is located at an H point (light blue) has shrunk as well, in all the three cases, but still is present. The dominant phase regions become the indirect semiconductor phases, which have both expanded remarkably in Figure 4.7 (a), (b) and (c). Such information is very important for the design of electronic devices using $Bi_{1-x}Sb_x$ nanowires. The much stronger quantum confinement effect in 10 nm wide nanowires makes the contrast for the anisotropy of all the diagrams much more obvious. The existence of inversion symmetry and the absence of mirror symmetry is shown clearly in Figure 4.7 (a) and (d). In Fig. 3 (b), it is clearer that the shapes of the boundaries of the electronic phase regions are mixtures of a circle and a hexagon, and is more hexagonal than in Figure 4.6 (b). The outlines of six-petal flowers in Figure 4.7 (e) are also much easier to observe than in Figure 4.7 (e). Furthermore, the mirror symmetry about the binary axis, the mirror symmetry about the trigonal axis, and the associated inversion symmetry of the orientation-stoichiometry phase diagram of the trigonal-binary crystallographic plane normal to the bisectrix is further clarified in Figure 4.7 (c) and (f).

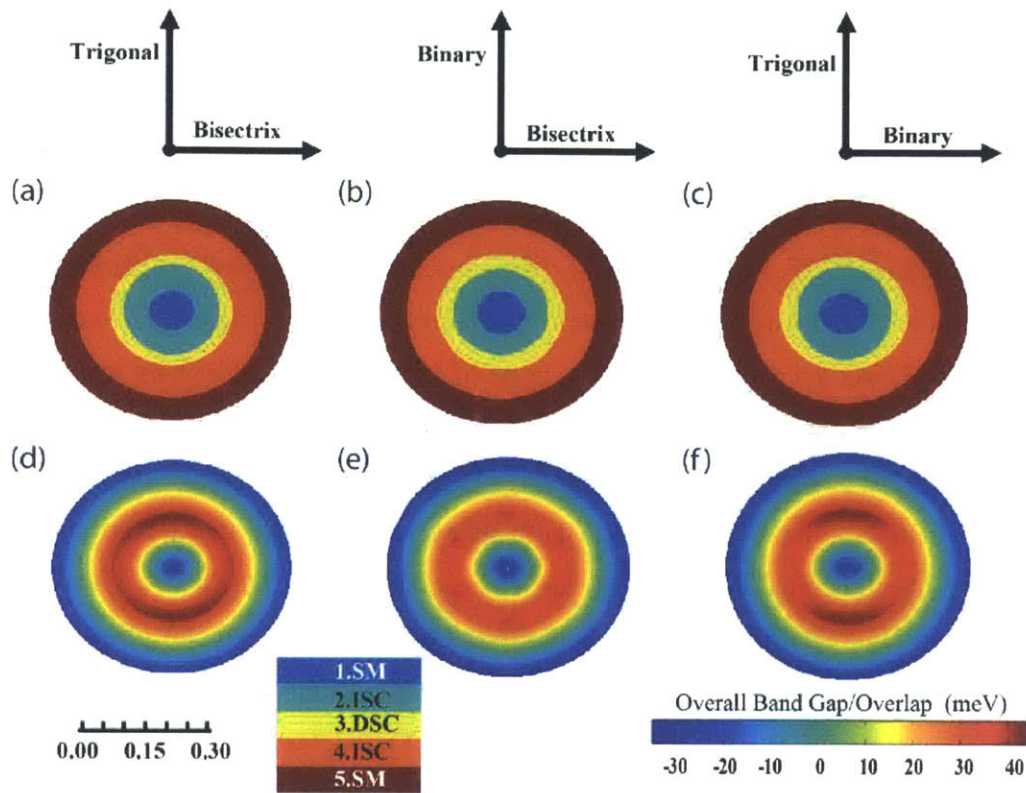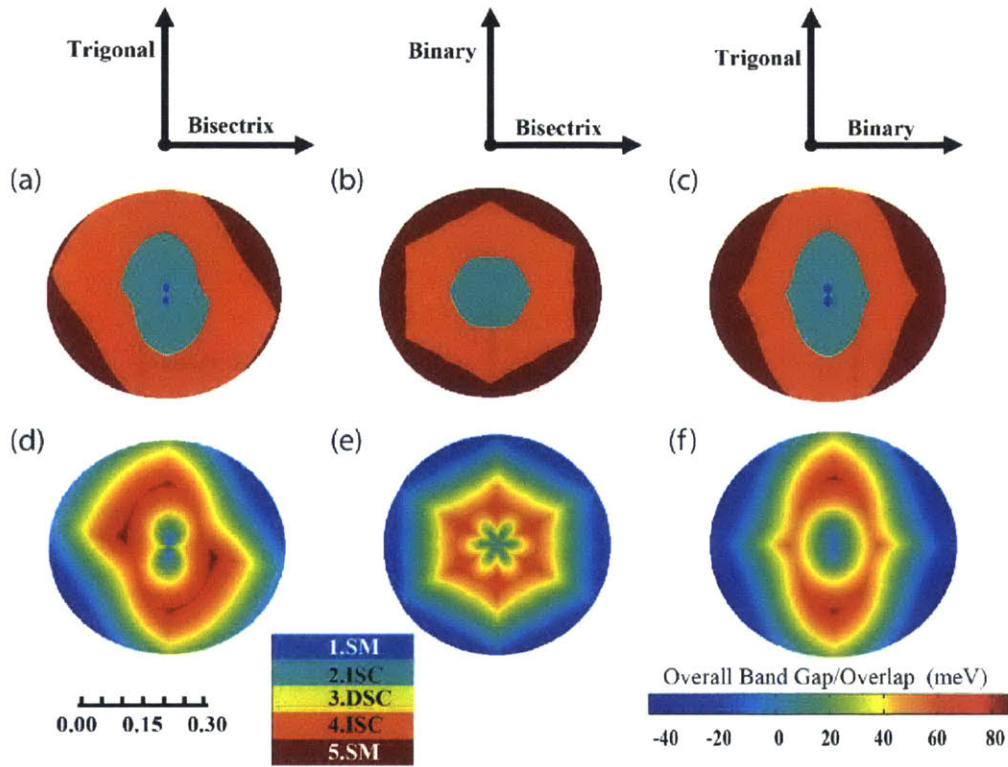**Figure 4.7:** The electronic phase diagrams (a)-(c), and the band gap/overlap diagrams (d)-(f) of $Bi_{1-x}Sb_x$ nanowires of 10 nm wire width, as a function of wire growth orientation and Sb composition x. All the notations and legends are the same as those defined in Figure 4.6.

The above discussions show that $Bi_{1-x}Sb_x$ nanowires of larger wire width show a much richer variation of electronic phases, but the contrast of anisotropy for different growth orientation is less obvious, while for the $Bi_{1-x}Sb_x$ nanowires of larger wire width, the richness of the variation of electronic phases is reduced, but the contrast of the anisotropy for different growth orientations is much enhanced. In order to show how the electronic and symmetry properties change with wire width and growth orientation, I have calculated the band gap/overlap diagrams as a function of wire width and growth orientation for both a small value of Sb composition of ($x=0.05$) and medium value of Sb composition ($x=0.13$), as shown in Figure 4.8.

The case of larger values of Sb compositions turn out to be similar with the case of small values, only the location of the top of the valence band edges for the semimetal phases and for the indirect semiconductor phases are at the H points for the median value of $x=0.13$, instead of at the T point which applies to ($x=0.05$). In order to make the values of band gap/overlap comparable in one plot, we choose to use a logarithm scale, and in order to avoid the divergent values of the band shift when the wire width gets close to 0, we choose to ignore the cases where the wire width is smaller than $10^{0.5} \approx 3$ nm.
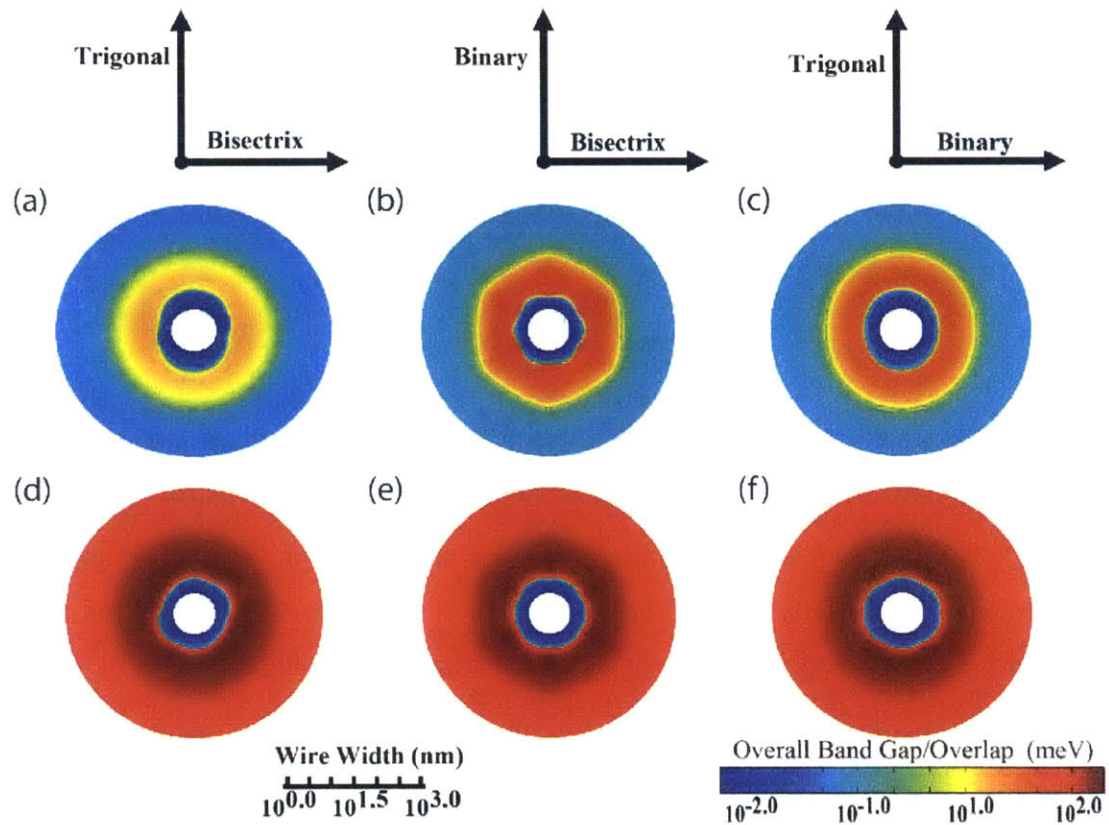
Figure 4.8: The band gap/overlap diagrams of $Bi_{1-x}Sb_x$ nanowires of small Sb composition ($x=0.05$) (a)-(c) and medium Sb composition ($x=0.13$) (d)-(f), as a function of wire growth orientation and wire width. All the notations and legends are the same as those defined in Figure 4.6 (d)-(f), except that the length of the radius in Figure 4.8 stands for the wire width scaled lografithmically, which lines up with the origin of each circularly shaped diagram.
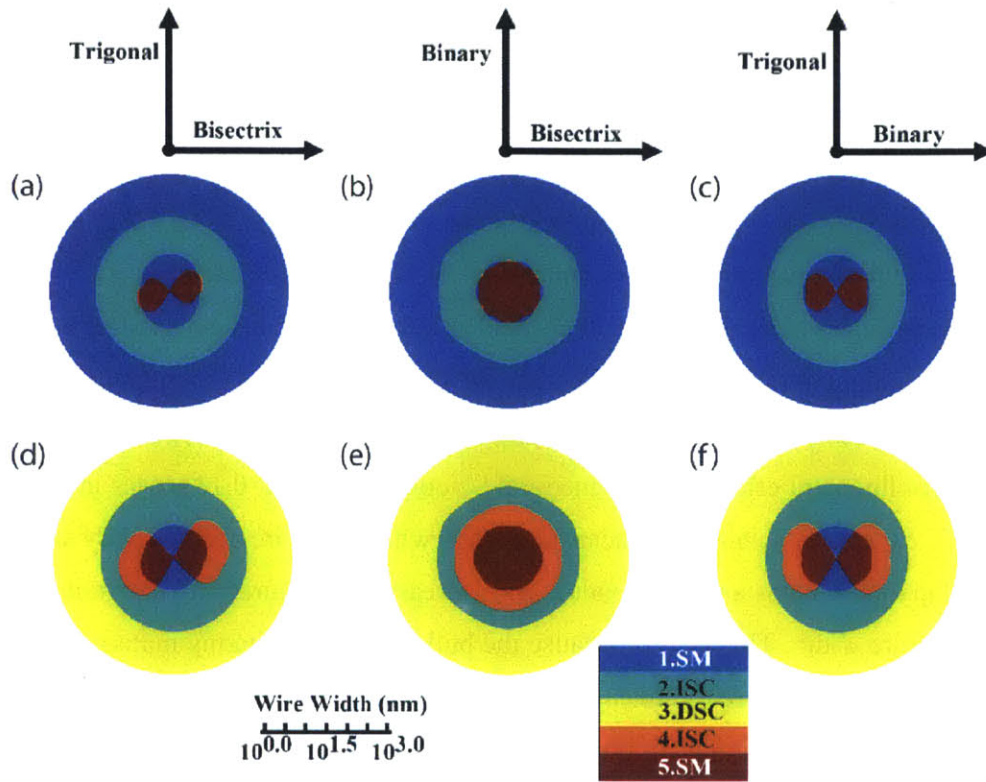
Figure 4.9: The electronic phase diagrams of $Bi_{1-x}Sb_x$ nanowires of small Sb composition ($x=0.05$) (a)-(c) and medium Sb composition ($x=0.13$) (d)-(f), as a function of wire growth orientation and wire width. All the notations and legends are the same with those defined in Figure 4.6 (a)-(c), except for that the length of the radius in Figure 4.8 stands for the wire width scaled lograrithmically.

For the small Sb composition ($x=0.05$) cases in Figure 4.8 (a), (b) and (c), we see that there are mainly three regimes for each diagram: the inner semimetal regime when the wire width is small, the semiconductor regime when wire width is medium, and the outer semimetal regime when wire width is large. The outer semimetal regime is easy to understand, because the bulk bismuth antimony material at this Sb composition is in the semimetal phase region, with the top of the valence band edge located at the T point, as shown in Fig. 4.2. The quantum confinement effect has induced an increase of the direct band gap region around the L points, and leads to a semiconductor phase at the medium wire width regime. That is also why the band overlap increases and saturates at a certain value with increasing wire width.

However, the mechanism governing the inner semimetal regime is different. In our model, the components of the inverse-effective-mass tensor and the direct band gap at an L point are negatively correlated. When the width of a nanowire is large, the non-trivial quantum confinement effect of an L point is shifting a band edge appears more quickly as the width decreases than does the trivial quantum confinement effect near an H or a T point. However, when the width of a nanowire is very small, the direct band gap at an L point is large enough to induce a significant reduction of the inter-band coupling, which changes the non-parabolic dispersions at the L point into parabolic dispersions with larger mass components. For this situation, the valence band edges at the T point and at the H points may, in contrast, have a larger quantum confinement effect. For the medium Sb composition (x=0.13) cases in Figure 4.8 (d), (e) and (f), except for a small area near the center, where the wire width is very small, each band gap/overlap diagram has a positive value, and increases and saturates to a certain value with increasing wire width. This is also because the bulk bismuth-antimony material with this Sb composition is in the indirect semiconductor phase region, as shown in Figure 4.2 (c). The corresponding phase diagrams as a function of wire width and growth orientation, for the small and medium Sb composition cases (x=0.05 and x=0.13) are shown in Figure 4.9, which further solidifies the analysis above.

4.5 Comparison between Theory and Experiments

We here compare the theoretically predicted band gap values with the experimental results by Morelli et al [72] with molecular beam epitaxy $Bi_{1-x}Sb_x$ thin films, as shown in Figure 4.10.
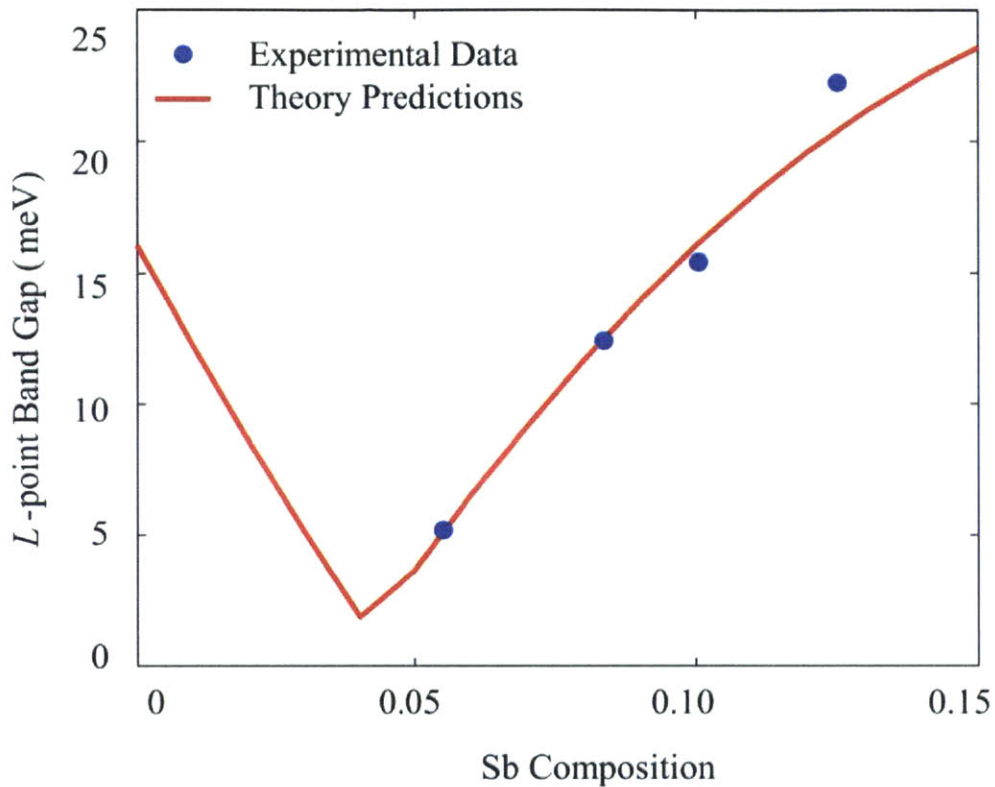
Figure 4.10: The values of band gap of single crystal $Bi_{1-x}Sb_x$ thin films (with 1000 nm thickness) are compared between the experimental data by Morelli et.al [72] and the theoretical predictions in this thesis.

It is seen that for $Bi_{1-x}Sb_x$ thin films (1000 nm thickness) with different values of Sb composition, the experimental results are consistent with the theoretical predictions with the model developed in this chapter. As the band gap of single crystal $Bi_{1-x}Sb_x$ thin films are barely measured, more experimental data might be needed to further verify the model.

4.6 Chapter Summary

This chapter has discussed the challenge in modeling the band structure of nanostructured narrow-band-gap materials. A dynamic iterative method is developed, which is more accurate than the use of effective mass theorem and the $k \cdot p$ theory, and is also more time efficient than

the first principle calculations. The applications of this newly developed method are here illustrated in bismuth antimony thin films and nanowires.

Chapter 5

Construction of Various Dirac Cone Materials

Dirac cone materials have recently attracted considerable attention. In an electronic band structure, if the dispersion relation $E(\mathbf{k})$ can be described by a linear function as $E(\mathbf{k}) = \mathbf{v} \cdot \hbar\mathbf{k}$, where $\mathbf{v}$ is the velocity, and $\mathbf{k}$ is the lattice momentum, the point where $E \rightarrow 0$ is called a Dirac point. A Dirac cone is a two-dimensional (2D) Dirac point. Dirac cone materials are interesting in electronic device design, quantum electrodynamics and desktop relativistic particle experiments. A single-, bi- or tri-Dirac cone system has one, two or three different Dirac cones degenerate in $E(\mathbf{k})$ in the first Brillouin zone, e.g. graphene is a bi-Dirac-cone system; the HgTe quantum well structure and the surface of topological insulator can be single-Dirac-cone systems. In this present work, we have investigated the $Bi_{1-x}Sb_x$ thin film system, and found that it could be a very promising candidate for synthesizing different kinds of Dirac-cone materials.

5.1 Introduction to Dirac Cone Materials

A few examples of single-Dirac-cones have been reported recently. Isotropic single-Dirac-cones have been observed in the surface states of bulk topological insulators [73] and HgTe quantum wells [74]. However, properties such as the anisotropy of these single-Dirac-cones are fixed and difficult to vary. Since Dirac-cone materials are considered as promising materials for the next generation of the electronic industry, constructing Dirac-cone-materials which are controllable in both anisotropy and fermion group velocity is very important, especially when various Dirac-cone materials can be constructed out of the same material. For this goal, we have investigated the $Bi_{1-x}Sb_x$ thin film system, and found that it could be a very promising candidate for synthesizing different kinds of Dirac-cone materials.

In this chapter, we show how to obtain single-, bi- and tri-Dirac-cone $Bi_{1-x}Sb_x$ thin films, and how to construct Dirac cones with different degrees of anisotropy. We also point out the possibility of constructing semi-Dirac cones in $Bi_{1-x}Sb_x$ thin films, where the $E(\mathbf{k})$ is parabolically dispersed along one direction and linearly dispersed along the other direction.

5.2 Construction of Various Types of Dirac Cone Materials

5.2.1 Construction of Dirac Cone Materials with Different Numbers of Scattering Valleys

If there is (are) one, two, or three Dirac cone(s) in the first Brillouin zone, we call the system a single-, bi-, or tri-Dirac cone material. We propose that single-, bi- and tri-Dirac-cone materials can be constructed from $Bi_{1-x}Sb_x$ thin films, by choosing proper synthesis conditions to control the relative symmetries of the three L points, as shown in Figure 5.1 [75].

Bi$_{0.96}$Sb$_{0.04}$ Thin Film, Thickness=100 nm
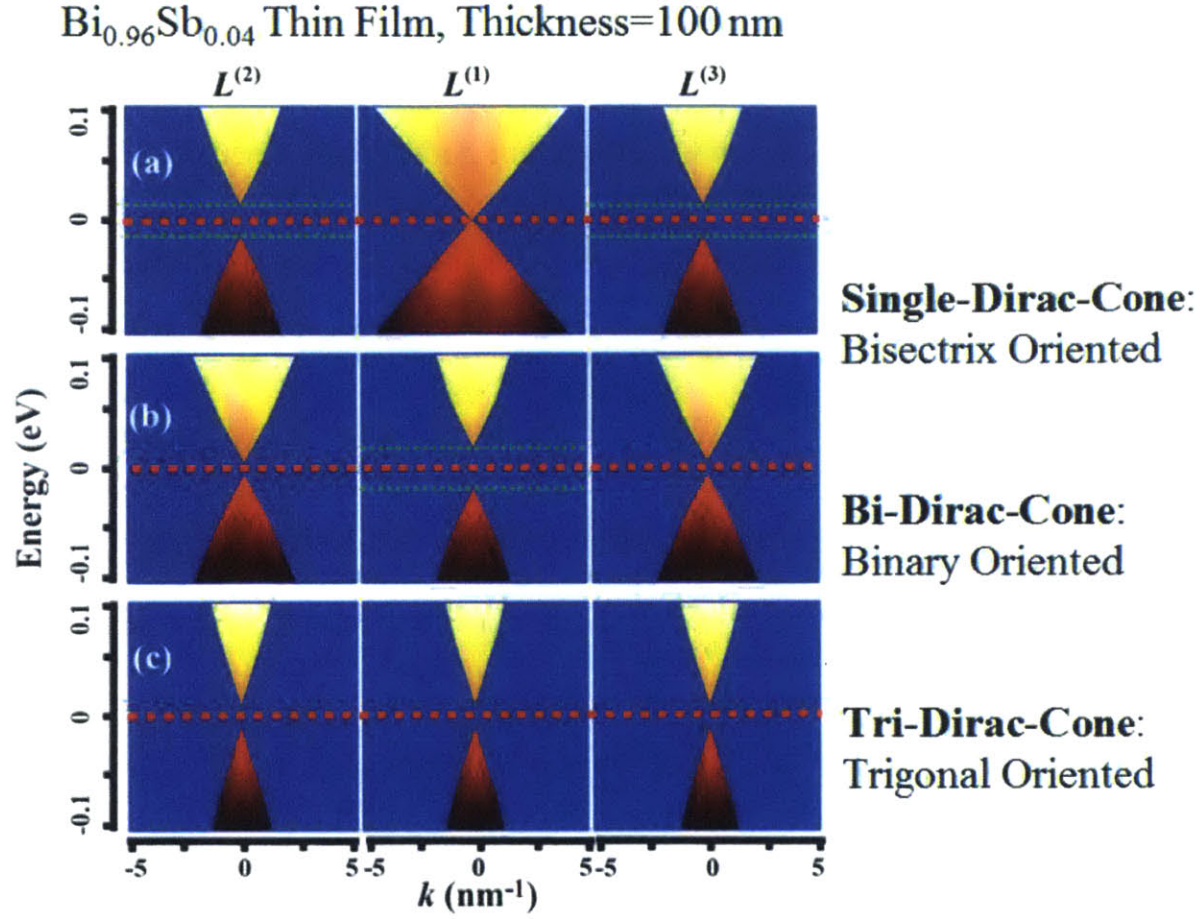
Figure 5.1: An illustration of (a) single-, (b) bi- and (c) tri-Dirac-cone Bi$_{1-x}$Sb$_x$ thin films grown along the (a) bisectrix, (b) binary and (c) trigonal axes, respectively. For the cross-sectional view of each cone, $\mathbf{k}_\parallel$ is chosen such that $\nabla_{\mathbf{k}_\parallel} E(\mathbf{k}_\parallel)$ has its minimum along that direction of $\mathbf{k}_\parallel$. The illustration is based on the example of Bi$_{1-x}$Sb$_x$ thin films with $l = 100$ nm, $x = 0.04$, $P = 1$ atm and $T \leqslant 77$ K, under which the L points of bulk Bi$_{1-x}$Sb$_x$ have a zero-gap. The scenario is similar for other conditions. In (a), a single-Dirac-cone is formed at the $L^{(1)}$ point, while the $L^{(2)}$- and $L^{(3)}$- point bandgaps are opened up. In (b), two degenerate quasi-Dirac cones are formed at the $L^{(2)}$ and $L^{(3)}$ points, while the $L^{(1)}$-point band-gap is much larger, which leads to a bi-quasi-Dirac-cone material. The band-gap at the $L^{(2)}$ and $L^{(3)}$ points can be less than 1 meV if a sample of $l = 200$ nm is chosen, which leads to exact Dirac cones. In (c), the

$L^{(1)}$-, $L^{(2)}$- and $L^{(3)}$-point band-gaps are all the same, and the three quasi-Dirac cones are degenerate in energy.

5.2.2 Construction of Dirac Cone with Different Anisotropic Degree

To characterize the anisotropy of a single Dirac cone, we define an anisotropy coefficient

$$\gamma = \frac{\mathbf{v}_{max}}{\mathbf{v}_{min}}, \tag{5.1}$$

where $\mathbf{v}_{max}$ and $\mathbf{v}_{min}$ are the maximum and minimum in-film carrier group velocities for a Dirac cone that are defined as

$$\mathbf{v}\left(\mathbf{k}_{\parallel}\right) = \frac{1}{\hbar}\nabla_{\mathbf{k}_{\parallel}}E\left(\mathbf{k}_{\parallel}\right). \tag{5.2}$$

Dirac cone with different anisotropic degree can also be constructed in the $Bi_{1-x}Sb_x$ thin films system by choosing proper synthesis conditions, as illustrated in Figure 5.2 [76].

Bi$_{0.96}$Sb$_{0.04}$ Bisectrix Oriented Growth
Film Thickness = 300 nm

Bi$_{0.96}$Sb$_{0.04}$ [60$\bar{6}$1] Oriented Growth
Film Thickness = 300 nm
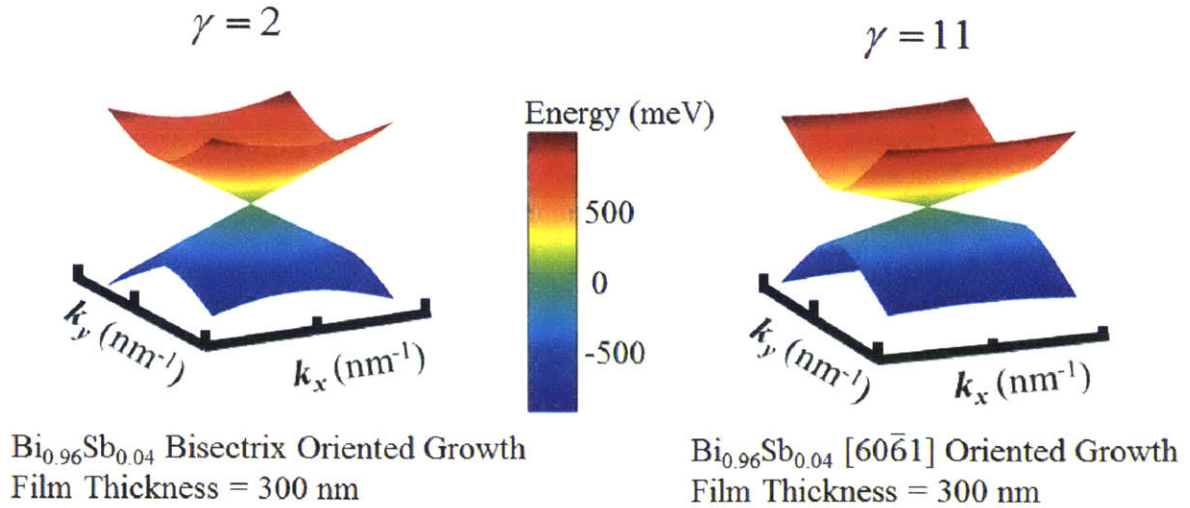
Figure 5.2: Example of Dirac cones at the L point with different anisotropy degree when proper synthesis conditions are chosen, respectively.

5.2.3 Control the Mini-Gap of Quasi-Dirac Cone

When a mini-band-gap is opened up in a Dirac cone for tuning the transport properties, it is called a quasi-Dirac cone. Quasi-Dirac cones are very important for low-temperature thermoelectrics. Quasi-Dirac cones can also be constructed based on the $Bi_{1-x}Sb_x$ thin films system, by controlling the synthesis conditions, as illustrated in Figure 5.3 [75].

Bisectrix Oriented Thin Film
Mini-Gap vs. Alloy Composition & Film Thickness
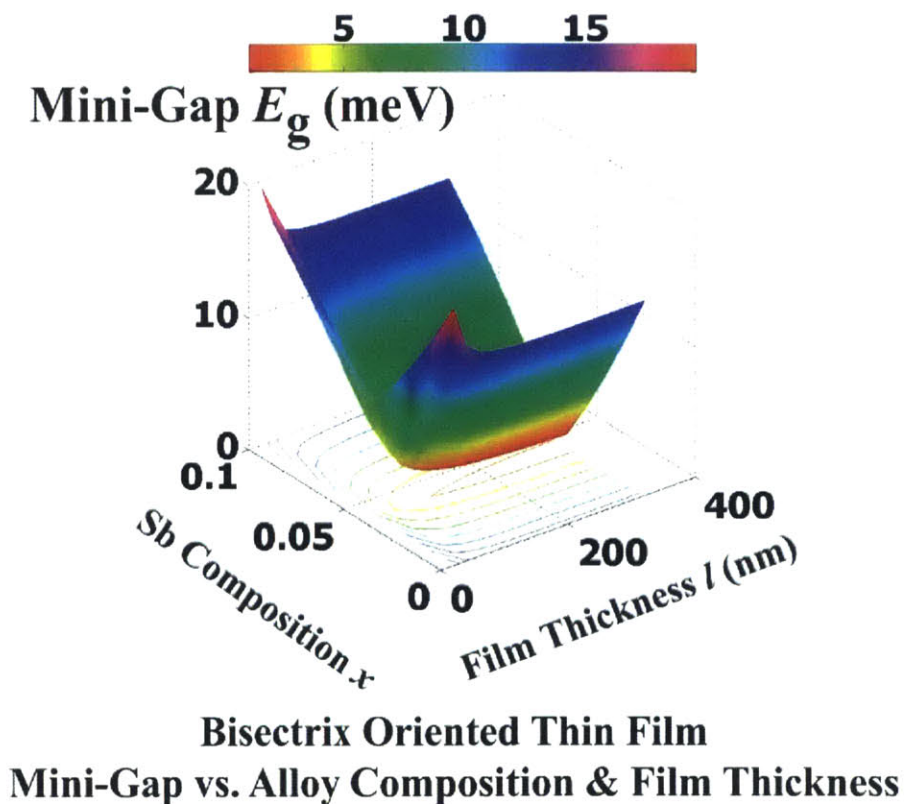
Figure 5.3: The $L^{(1)}$-point mini-gap vs. film thickness l and Sb composition x for the $Bi_{1-x}Sb_x$ thin films grown along the bisectrix axis.

5.2.4 Constructing Semi-Dirac Cones

If a Dirac cone is relativistically (linearly) dispersed along one direction and classically (parabolically) dispersed along its perpendicular direction, this Dirac cone is called a semi-Dirac cone. In the $Bi_{1-x}Sb_x$ thin films system, if we carefully choose the film synthesis condition, semi-Dirac cones can also be constructed as illustrated in Figure 5.4 [75].

Bi$_{0.9}$Sb$_{0.1}$ Thickness=100 nm, Oriented 40° to the trigonal
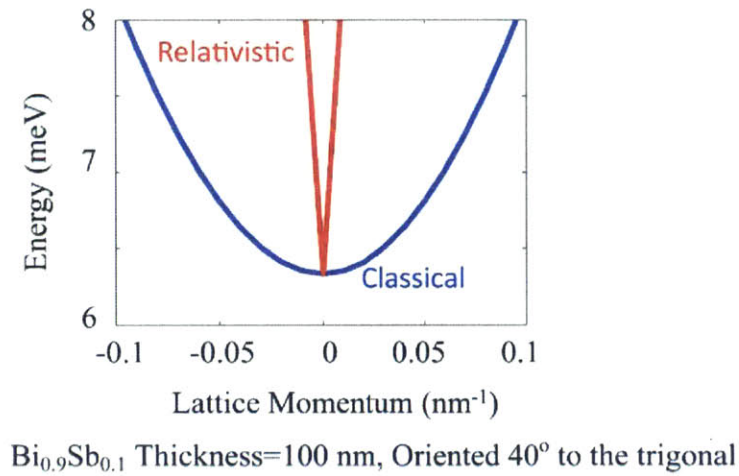
Figure 5.4: Example of a semi-Dirac cone in the $Bi_{1-x}Sb_x$ thin film system (x=0.10 and l=100 nm). It can be seen that around the $L^{(1)}$ point, the fermions are linearly dispersed along the $\mathbf{v}_{max}$ direction, and parabolically dispersed along the $\mathbf{v}_{min}$ direction.

5.3 Chapter Summary

In this chapter, the construction of various kinds of Dirac cone materials were discussed based on the $Bi_{1-x}Sb_x$ thin films materials system, including Dirac cone materials with different numbers of scattering valleys, Dirac cones with different degrees of anisotropy, quasi-Dirac cones with controllable mini-band-gaps and semi-Dirac cones.

Chapter 6

Anisotropic Transport for Parabolic, Non-Parabolic and Linear Bands of Different Dimensions

Anisotropic thermoelectrics is a very interesting topic among recent researchers. The transport distribution function plays the central role on modeling the anisotropic thermoelectrics. The methodology of numerical integrations is used in previous literature on anisotropic transport, which does not capture the sharp change of transport distribution function and density of states at the band edges that we will show later in this chapter. However, the sharp change of transport distribution function and density of states at band edges are very important in enhancing the thermoelectric performance. Thus, an analytical methodology that is robust on modeling the sharp change of transport distribution function and density of states at a band edges is needed. To our best knowledge, there has not been a paper giving the systematic study on the analytical models of anisotropic transport distribution function for different kinds of band valleys in different dimensions under different assumptions. Therefore, the main focus of this chapter is to develop such a robust analytical methodology on modeling the anisotropic transport distribution function. So the main content in this chapter will be 1) a systematic method is developed to model the anisotropic transport distribution function, for 3D, 2D and 1D systems, in parabolic, non-parabolic and linear dispersion relations, under both the relaxation time approximation and the mean free path approximation; 2) it is found that the Onsage's relation of transport can be

violated under certain conditions; 3) the newly developed methodology is compared with the traditional used numerical methodology.

As a matter of fact, most good thermoelectric materials are electronically anisotropic, such as Bi_2Te_3 and $Bi_{1-x}Sb_x$. Even isotropic thermoelectric/electronic materials, such as $Si_{1-x}Ge_x$, PbTe, PbS, also have anisotropic carrier-pockets. Thus, to calculate the electronic transport quantities associated anisotropic carrier-pockets in a simple physical way is very important for the research of optimizing thermoelectric/electronic performance. Good efforts have been made using numerical integrations for specific materials systems. However, the thermoelectric/electronic optimization problem requires closed-formed and physical expression of these transport quantities, such that the materials-searching and the conditions-optimization can be carried out among the huge number of material candidates and the various parameters, such as temperature T and Fermi level E_f.

6.1 Basics of Anisotropic Transport

We recall that under the relaxation time approximation of anisotropic Boltzmann equation,

$$\boldsymbol{\sigma} = e^2 \mathbf{I}_{[l=0]}, \tag{6.1}$$

$$\mathbf{S} = \frac{k_B}{e} \frac{\mathbf{I}_{[l=1]}}{\mathbf{I}_{[l=0]}}, \tag{6.2}$$

$$\boldsymbol{\kappa}_e = \boldsymbol{\kappa}_0 - T\mathbf{S}^\dagger \boldsymbol{\sigma} \mathbf{S} \tag{6.3}$$

and

$$\boldsymbol{\kappa}_0 = T \cdot k_B^2 \mathbf{I}_{[l=2]}, \tag{6.4}$$

where

$$I_{[l]} = \int \left(-\frac{\partial f_0}{\partial E} \right) \Xi(E) \left(\frac{E - E_f}{k_B T} \right)^l dE \qquad (6.5)$$

and

$$\Xi(E) = \sum_{\mathbf{k}} \delta(E - E_{\mathbf{k}}) \mathbf{v} \otimes \boldsymbol{\tau}\mathbf{v} \qquad (6.6)$$

is the transport distribution tensor, and $\mathbf{v}$, $\boldsymbol{\tau}$ and f_0 are the carrier group velocity, the relaxation time tensor and the Fermi distribution, respectively. It is clear that the transport distribution tensor $\Xi(E)$ plays the central role in determining all these electronic transport quantities. However, the complex calculations of inner- and outer-product between different ranks of tensors have always been misunderstood and improperly assumed in literatures that make numerical calculations of the transport distribution tensor for anisotropic systems.

Scheidenmatel et al. [77], Lee et al. [78], and Yavorsky et al. [79], have calculated the anisotropic transport distribution tensor with numerical integrations based on first-principle results for the specific material of intrinsic bulk Bi_2Te_3 without doping, by assuming that the relaxation time is a constant, which has given important references for this bulk material of intrinsic bulk Bi_2Te_3. However, these numerical methodologies take heavy computations, and is not easy for implement in the materials-searching and the conditions-optimization problems of thermoelectric/electronics. Teramoto et al. [80, 81] have numerically calculated the anisotropic transport tensor in bulk Bi and bulk $Bi_{1-x}Sb_x$. However, a strong assumption is assumed that $\mathbf{v} \otimes \boldsymbol{\tau}\mathbf{v} = \boldsymbol{\tau}\mathbf{v} \otimes \mathbf{v}$, without further validation. Bies et al. [82] have made a remarkable progress on giving a relatively simpler expression for 3D and 2D parabolic bands with the dispersion in the form of $E(\mathbf{k}) = (\hbar^2/2)\mathbf{k}^T \mathbf{M}^{-1} \mathbf{k}$, assuming that $\boldsymbol{\tau}(\mathbf{k}) = \tau_0[E(\mathbf{k})]\mathcal{U}$, where τ_0 is a scalar function of E, and $\mathcal{U}$ is a dimensionless constant matrix. However, cases for the non-parabolic bands that happens at the L points of Bi, $Bi_{1-x}Sb_x$, PbTe, PbSe, and PbS, and at the bottom of

conduction band of Be_2Te_3, and $Si_{1-x}Ge_x$, and cases for linear bands that happens at the K point of graphene, the L point of certain $Bi_{1-x}Sb_x$, are not discussed. All these previous achievement are suitable for study the electronic transport of a certain material, but not suitable for the materials-searching and the conditions-optimization problems of thermoelectric/electronics.

In this chapter, I have derived the analytical form of anisotropic transport distribution tensor for a parabolic band in a three-dimensional materials system under the condition that the relaxation time tensor is only a function of energy at a certain temperature, i.e. $\boldsymbol{\tau}(\mathbf{k}) = \tau_0(E)\mathbf{T}$, where $\mathbf{T}$ is a constant tensor. I have found that the transport distribution tensor can be asymmetrical, i.e. exhibiting a deviation from the Onsager relation, which is usually not considered in previous literatures on modeling electronic transport. I have then developed the analytical form of anisotropic transport distribution tensor for a linear band, as well as a non-parabolic band of a more general form beyond the Lax model $E + E^2 / E_g = (\hbar^2 / 2)\mathbf{k}^T\mathbf{M}^{-1}\mathbf{k}$ [83], where E_g is the direct band gap. Then, I have generalized the results to two- and one-dimensional materials systems. Furthermore, I have derived the anisotropic distribution tensor under the condition that the relaxation time tensor is a function of not only energy, but also carrier velocity. Finally, I have done a comparison between the numerical method used in previous literatures and our analytical results reported in this chapter.

6.2 Anisotropic Transport for Three-Dimensional Parabolic Bands

For clarification of the problem, we will discuss the transport distribution tensor in the Cartesian coordinates system that coincide with the principal axes of the effective-mass tensor, e.g. for a parabolic band $E(\mathbf{k}) = (\hbar^2 / 2)\mathbf{k}^T\mathbf{M}^{-1}\mathbf{k}$, where $\mathbf{k}$ is the lattice momentum measured from the bottom/top of the conduction/valence band, and $\mathbf{M}$ has no off-diagonal components. $\Xi(E)$

expressed in other coordinates systems can be easily obtained by rotation matrixes. For an isotropic parabolic band, the dispersion reduces to $E(\mathbf{k}) = (\hbar^2/2m)\mathbf{k}^2$, where

$\mathbf{k}^2 = k_1^2 + k_2^2 + k_3^2$. By symmetry, we know that $\Xi(E)$ can only take the form of $\Xi(E) = \Xi_0(E)\mathscr{U}$, where $\Xi_0(E)$ is a scalar function of E, and $\mathscr{U}$ is the unitary matrix. Hence, we know

$$\Xi(E) = \sum_{\mathbf{k}} \delta(E - E_{\mathbf{k}})\tau_0(E) \begin{pmatrix} v_1^2 & & \\ & v_2^2 & \\ & & v_3^2 \end{pmatrix}. \tag{6.7}$$

By symmetry, we have

$$\Xi_0(E) = \Xi_{ii}(E) = \frac{1}{3}\sum_{\mathbf{k}} \delta(E - E_{\mathbf{k}})\tau_0(E)v^2 = \frac{2E}{3m}D(E)\tau_0(E), \tag{6.8}$$

where $v^2 = v_1^2 + v_2^2 + v_3^2$, i=1,2 or 3, and $D(E) = \sum_{\mathbf{k}} \delta(E - E_{\mathbf{k}})$ is the density of states, which

is $(1/4\pi^2)(2m/\hbar^2)^{3/2}E^{1/2}$ for a 3D isotropic parabolic band. Thus, we have

$$\Xi_0(E) = (2^{1/2}/3\pi^2\hbar^3)m^{1/2}E^{3/2}\tau_0(E). \tag{6.9}$$

For a general anisotropic parabolic dispersion expressed in the principal-axes coordinates,

$E(\mathbf{k}) = (\hbar^2/2)(k_1^2/m_1 + k_2^2/m_2 + k_3^2/m_3)$, the transport distribution tensor is

$\Xi(E) = \sum_{\mathbf{k}} \delta(E - E_{\mathbf{k}})\mathbf{v} \otimes \boldsymbol{\tau}\mathbf{v}$, which is generally not equal to $\sum_{\mathbf{k}} \delta(E - E_{\mathbf{k}})\boldsymbol{\tau}\mathbf{v} \otimes \mathbf{v}$, i.e.

$v_i \sum_l \tau_{jl}v_l \neq v_j \sum_l \tau_{il}v_l$ for $i \neq j$ in an anisotropic case. Thus, to get the transport distribution

tensor, we need to calculate each $\sum_{\mathbf{k}} \delta(E - E_{\mathbf{k}})v_i v_j \tau_{pq}$, which we define as $\Theta_{ijpq}(E)$, where

we have $\Xi_{ij}(E) = \sum_l \Theta_{iljl}(E) . \Theta_{ijpq}(E)$ can then be treated as the mean value of $v_i v_j \tau_{pq}$ at

the constant energy surface of E, multiplied by the density of states at E, i.e.

$\Theta_{ijpq}(E) = \tau_{pq}\langle v_i v_j \rangle_E D(E)$. According to $v_i = \hbar^{-1}\partial E / \partial k_i = \hbar k_i / m_i$, we have

$\langle v_i v_j \rangle_E = (\hbar^2 / m_i m_j)\langle k_i k_j \rangle_E = \delta_{ij} 2E / 3m_i$. Thus, $\Theta_{ijpq}(E) = \delta_{ij} 2\tau_{pq} D(E)E / 3m_i$ and

$\Xi_{ij}(E) = (2E / 3m_i)D(E)\tau_{ji}$.

Hence, we have found that if the relaxation time tensor $\boldsymbol{\tau}$ does not diagonalize in the same

coordinates as the dispersion relation $E(\mathbf{k})$ does, the off-diagonal components of the transport

distribution tensor $\Xi(E)$ will not be cancelled out, i.e. $\Xi_{ij}(E) = (2E / 3m_i)D(E)\tau_{ji}$, which is

an advanced explanation for the assumptions used in Ref. [82]. We also see that even if the

relaxation time tensor $\boldsymbol{\tau}$ is a symmetric tensor, the transport distribution tensor Ξ is not

necessarily symmetric, if $\boldsymbol{\tau}$ does not diagonalizes in the same coordinates system as $E(\mathbf{k})$, i.e.

$\Xi_{ij}(E) = (2E / 3m_i)D(E)\tau_{ji}$ is generally not equal to $\Xi_{ji}(E) = (2E / 3m_j)D(E)\tau_{ij} (i \neq j)$.

This possible deviation from the Onsager relation has not been considered in previous literatures

on anisotropic electronic transport, which simply assumed that if $\boldsymbol{\tau}$ is symmetrical, Ξ is

naturally symmetrical. Our finding of possible deviation from Onsager's relation here is

consistent with the work done by Truesdell [84] and Bies [82] through different approaches.

6.3 Anisotropic Transport for Low-Dimensional Parabolic Bands

For low-dimensional system, the transport distribution tensor can be derived in the similar way.

For a 2D isotropic parabolic band, the transport distribution can be obtained by the same

symmetry argument we did above for 3D case, except that $\sum\limits_{\mathbf{k}_{[2D]}} \delta(E - E_{\mathbf{k}_{[2D]}})\tau_{0,[2D]}(E)v_{[2D]}^2$

should be divided by 2 instead of 3. Thus, we have

$$\Xi_{0,[2D]}(E) = \Xi_{[2D],ii}(E) = \frac{1}{2}\sum\limits_{\mathbf{k}_{[2D]}} \delta(E - E_{\mathbf{k}_{[2D]}})\tau_{0,[2D]}(E)v_{[2D]}^2 = (E/m)D_{[2D]}(E)\tau_{0,[2D]}(E).$$

(6.10)

For a 2D anisotropic parabolic band, we have $\Xi_{[2D],ij}(E) = \sum\limits_l \Theta_{[2D],iljl}(E)$, where

$$\Theta_{[2D],ijpq}(E) = \sum\limits_{\mathbf{k}_{[2D]}} \delta(E - E_{\mathbf{k}_{[2D]}})v_{[2D],i}v_{[2D],j}\tau_{[2D],pq}.$$

(6.11)

$\Theta_{[2D],ijpq}(E)$ can also then be treated as the mean value of $v_{[2D],i}v_{[2D],j}\tau_{[2D],pq}$ at the constant

energy circle of E, multiplied by the density of states at E, in the 2D system, i.e.

$\Theta_{[2D],ijpq}(E) = \tau_{[2D],pq}\left\langle v_{[2D],i}v_{[2D],j}\right\rangle_E D_{[2D]}(E)$. Then we have

$$\left\langle v_{[2D],i}v_{[2D],j}\right\rangle_E = (\hbar^2/m_i m_j)\left\langle k_{[2D],i}k_{[2D],j}\right\rangle_E = \delta_{ij}E/m_i.$$

(6.12)

Thus, $\Theta_{[2D],ijpq}(E) = \delta_{ij}\tau_{[2D],pq}D_{[2D]}(E)E/m_i$ and $\Xi_{[2D],ij}(E) = (E/m_i)D_{[2D]}(E)\tau_{[2D],ji}$.
For the 1D parabolic band, we simply have,

$$\Xi_{[1D]}(E) = (2E/m)D_{[1D]}(E)\tau_{0,[1D]}(E).$$

(6.13)

101

6.4 Anisotropic Transport for Non-Parabolic Bands

To describe a non-parabolic band, the Lax model, i.e. $E + E^2 / E_g = (\hbar^2/2)\mathbf{k}^T\mathbf{M}^{-1}\mathbf{k}$ [63], is often used, e.g. the L-point band edges of bismuth and bismuth antimony. Instead of talking about this specific form of non-parabolic band, we discuss a general form of non-parabolic band defined as,

$$\tilde{E} = \sum_{N=0}^{\infty} c_N E^N = (\hbar^2/2)\mathbf{k}^T\mathbf{M}^{-1}\mathbf{k} , \tag{6.14}$$

where c_N are constants. In the principal-axes coordinates of $\tilde{E}(\mathbf{k})$, we have

$$\tilde{E} = \sum_{N=0}^{\infty} c_N E^N = (\hbar^2/2)(k_1^2/m_1 + k_2^2/m_2 + k_3^2/m_3) . \tag{6.15}$$

The transport distribution tensor can still be calculated as

$$\Xi_{ij}(E) = \sum_{l} \tau_{jl} \langle v_i v_l \rangle_E D(E) ,$$

except that

$$\langle v_i v_l \rangle_E D(E) = \langle v_i v_l \rangle_{E(E)} D(\check{E})\frac{d\tilde{E}}{dE} \tag{6.16}$$

and

$$v_i = \frac{1}{h}\frac{\partial E}{\partial k_i} = \frac{1}{h}\frac{\partial \tilde{E}}{\partial k_i}/\frac{d\tilde{E}}{dE} = \frac{hk_i}{m_i}/\frac{d\tilde{E}}{dE}.$$

(6.17)

Thus, we have

$$\left\langle v_i v_j \right\rangle_E D(E) = \delta_{ij}\frac{2\tilde{E}}{3m_i}D(\tilde{E})/\frac{d\tilde{E}}{dE}$$

(6.18)

and

$$\Xi_{ij}(E) = \sum_l \tau_{jl}\delta_{il}\frac{h^2}{m_i m_l}D(\tilde{E})/\frac{d\tilde{E}}{dE} = \tau_{ji}\frac{2\tilde{E}}{3m_i}D(\tilde{E})/\frac{d\tilde{E}}{dE}.$$

(6.19)

For a 2D non-parabolic band, where

$$\tilde{E} = \sum_{N=0}^{\infty} c_{[2D],N}E^N = (\hbar^2/2)(k_{[2D],1}^2/m_1 + k_{[2D],2}^2/m_2),$$

we have

$$\left\langle v_{[2D],i} v_{[2D],j} \right\rangle_E D_{[2D]}(E) = \delta_{ij}\frac{\tilde{E}}{m_i}D_{[2D]}(\tilde{E})/\frac{d\tilde{E}}{dE}$$

(6.20)

and

$$\Xi_{[2D],ij}(E) = \tau_{[2D],ji}\frac{\tilde{E}}{m_i}D_{[2D]}(\tilde{E})/\frac{d\tilde{E}}{dE}.$$

(6.21)

For a 1D non-parabolic band, where $\tilde{E} = \sum_{N=0}^{\infty} c_{[1D],N}E^N = (h^2/2)(k_{[1D]}^2/m)$, we have

$$\Xi_{[1D]}(E) = \frac{2\tilde{E}}{m_i} D_{[1D]}(\tilde{E})\tau_{[1D]}(E)/\frac{d\tilde{E}}{dE}.$$ (6.22)

The linear band case, e.g. the possible Dirac point in bismuth antimony, is included in our defined general form of non-parabolic dispersion, if we take $c_N = c_2\delta_{2,N}$, i.e.

$$E = (\hbar/\sqrt{2c_2})\sqrt{k_x^2/m_1 + k_y^2/m_2 + k_z^2/m_3}$$ (6.23)

and

$$\Xi_{ij}(E) = \frac{1}{6\pi^2\hbar^3}\frac{v_i^2}{v_1v_2v_3}E^2\tau_{ji},$$ (6.24)

where $v_i = 1/\sqrt{2c_2m_i}$ and m_i is a parameter defined in Equation (6.15), which does not mean mass anymore in the linear dispersion.

For 2D Dirac cones, we have

$$E = (\hbar/\sqrt{2c_{[2D],2}})\sqrt{k_1^2/m_1 + k_2^2/m_2}$$ (6.25)

and

$$\Xi_{[2D],ij}(E) = \frac{v_{[2D],i}^2}{4\pi\hbar^2 v_{[2D],1}v_{[2D],2}}\tau_{[2D],ji}E,$$ (6.26)

where $v_{[2D],i} = 1/\sqrt{2c_{[2D],2}m_i}$. The dispersion relation reduces to $E = \hbar k/\sqrt{2mc_{[2D],2}}$ in isotropic Dirac cones, e. g. in graphene and topological insulators, where the carrier group velocity is $v = 1/\sqrt{2mc_{[2D],2}}$ and the transport distribution tensor is

$\Xi_{[2D]}(E) = (E / 4\pi\hbar^2)\tau_{[2D]}$. Following the similar argument, we can obtain the transport distribution for a 1D system as

$$\Xi_{[1D]}(E) = v_{[1D]}\tau_{[1D]} / \pi\hbar . \tag{6.27}$$

6.5 Anisotropic Transport under Mean Free Path Regime

All the above discussions are valid for cases where τ is only a function of energy E, and not a function of velocity v. For some systems where semi-empirical constant mean free path approximation is preferred, especially in low-dimensional systems with ballistic scatterings [18, 20, 85, 86]. Thus, we will start from the low-dimensional systems. For an 1D system, the transport distribution is

$$\Xi_{[1D]}(E) = \sum_{k_{[1D]}} \delta(E - E_{k_{[1D]}})\mathbf{v}_{[1D]} \otimes \lambda_{[1D]}(E)(\mathbf{v}_{[1D]} / |\mathbf{v}_{[1D]}|), \tag{6.28}$$

where we assumed that the mean free path $\lambda_{[1D]}$ is only a function of E at a specific temperature. Everything reduces to scalar in a 1D system, i.e.

$$\Xi(E) = \sum_{k} \delta(E - E_k)|v|\lambda(E) = \lambda(E)\sqrt{2E/m}D_{[1D]}(E). \tag{6.29}$$

For a 2D system, the 2D transport distribution tensor is

$$\Xi_{[2D]}(E) = \sum_{k_{[2D]}} \delta(E - E_{k_{[2D]}})\mathbf{v}_{[2D]} \otimes \lambda_{[2D]}(\mathbf{v}_{[2D]} / |\mathbf{v}_{[2D]}|). \tag{6.30}$$

105

Thus, we want to calculate each $\displaystyle\sum_{\mathbf{k}_{[2D]}} \delta(E - E_{\mathbf{k}_{[2D]}}) v_{[2D],i} v_{[2D],j} (\lambda_{[2D],pq} / \sqrt{v_{[2D],1}^2 + v_{[2D],2}^2})$

By calculation, we have found that

$$
\begin{aligned}
&\sum_{\mathbf{k}_{[2D]}} \delta(E - E_{\mathbf{k}_{[2D]}}) v_{[2D],i} v_{[2D],i} \frac{\lambda_{[2D],pq}}{\sqrt{v_{[2D],1}^2 + v_{[2D],2}^2}} \\
&= \lambda_{[2D],pq} \frac{4\sqrt{2E}}{\sqrt{m_i}} \frac{m_i \cdot EK(\sqrt{1 - \dfrac{m_i}{m_j}}) - m_j \cdot EE(\sqrt{1 - \dfrac{m_i}{m_j}})}{m_i - m_j} D_{[2D]}(E)
\end{aligned}
\tag{6.31}
$$

and

$$
\sum_{\mathbf{k}_{[2D]}} \delta(E - E_{\mathbf{k}_{[2D]}}) v_{[2D],i} v_{[2D],j} \frac{\lambda_{[2D],pq}}{\sqrt{v_{[2D],1}^2 + v_{[2D],2}^2}} = 0 \ (i \neq j),
\tag{6.32}
$$

where EK and EE are the first type and second type elliptical integrations. Thus, we have

$$
\Xi_{[2D],ij}(E) = \lambda_{[2D],ji} \frac{4\sqrt{2E}}{\sqrt{m_i}} \frac{m_i \cdot EK(\sqrt{1 - \dfrac{m_i}{m_j}}) - m_j \cdot EE(\sqrt{1 - \dfrac{m_i}{m_j}})}{m_i - m_j} D_{[2D]}(E).
\tag{6.33}
$$

For 3D system, we have $\Xi(E) = \displaystyle\sum_{\mathbf{k}} \delta(E - E_{\mathbf{k}}) \mathbf{v} \otimes \lambda(\mathbf{v}/|\mathbf{v}|)$, this is used for systems such as Bi_2Te_3 and Sb_2Te_3 [79]. We need to calculate,

$$
\sum_{\mathbf{k}} \delta(E - E_{\mathbf{k}}) v_i v_j \frac{\lambda_{pq}}{\sqrt{v_1^2 + v_2^2 + v_3^2}} = \lambda_{pq} \left\langle \frac{v_i v_j}{\sqrt{v_1^2 + v_2^2 + v_3^2}} \right\rangle_E D(E).
\tag{6.34}
$$

By calculations, we have,

$$\left\langle \frac{v_i v_j}{\sqrt{v_1^2 + v_2^2 + v_3^2}} \right\rangle_E = \delta_{ij} \frac{\sqrt{2E}}{m_i} \sqrt{\tilde{m}}, \tag{6.35}$$

where we defined

$$\sqrt{\tilde{m}} = \left\langle \frac{\sin^2 \theta \cos^2 \varphi}{\sqrt{\dfrac{\sin^2 \theta \cos^2 \varphi}{m_1} + \dfrac{\sin^2 \theta \sin^2 \varphi}{m_2} + \dfrac{\cos^2 \theta}{m_3}}} \right\rangle_E \tag{6.36}$$

$$= \int_{\varphi=0}^{2\pi} \int_{\theta=0}^{\pi} \frac{\sin^2 \theta \cos^2 \varphi}{\sqrt{\dfrac{\sin^2 \theta \cos^2 \varphi}{m_1} + \dfrac{\sin^2 \theta \sin^2 \varphi}{m_2} + \dfrac{\cos^2 \theta}{m_3}}} \sin \theta \, d\theta \, d\varphi$$

which turns out to have non-elementary functions in the analytical form. Putting Equation (6.35) into Equation (6.34) we have

$$\lambda_{pq} \sum_k \delta(E - E_k) \frac{v_i v_j}{\sqrt{v_1^2 + v_2^2 + v_3^2}} = \delta_{ij} \lambda_{pq} \frac{\sqrt{2E}}{m_i} \sqrt{\tilde{m}} D(E), \tag{6.37}$$

which gives

$$\Xi_{ij}(E) = \lambda_{ji} \frac{\sqrt{2E}}{m_i} \sqrt{\tilde{m}} D(E). \tag{6.38}$$

6.6 Applications to Different Materials

Up to now we have considered most of the situations for anisotropic transport distribution tensor, including parabolic, non-parabolic and linear dispersions, including three-, two- and one-dimensional systems, and also including relaxation time approximation and mean free path approximation in the present work. We now compare the numerical method used in previous literature and the analytical method we have developed here in this chapter in some specific materials. The numerical method basically uses a normalized quasi-delta function $\sigma^{-1}\tilde{\delta}(E/\sigma)$ to mimic the delta function in Equation (6.6) [87-89]. $\sigma^{-1}\tilde{\delta}(E/\sigma)$ is a smeared convolution of $\delta(E)$ and σ is the smearing, i.e. $\int_{-\infty}^{\infty}\sigma^{-1}\tilde{\delta}(E/\sigma)dE = 1$ and $\lim_{\sigma\to 0}\sigma^{-1}\tilde{\delta}(E/\sigma) = \delta(E)$.

Usually, the Gaussian smearing function $\sigma^{-1}\tilde{\delta}(E/\sigma) = (1/\sqrt{2\pi}\sigma)\exp(-E^2/2\sigma^2)$ is chosen for its simplicity and special integral properties, and the smearing is set to be equal to the thermal smearing of $\sigma = k_B T$. A grid of points in the k-space are sampled. Thus, the density of states and the transport distribution tensor can be approximated as [87-89],

$$D(E) = \sum_{\mathbf{k}\in\{\text{Sampled Grid}\}} \sigma^{-1}\tilde{\delta}[(E-E_{\mathbf{k}})/\sigma] \tag{6.39}$$

and

$$\Xi(E) = \sum_{\mathbf{k}\in\{\text{Sampled Grid}\}} \sigma^{-1}\tilde{\delta}[(E-E_{\mathbf{k}})/\sigma]\mathbf{v}\otimes\tau\mathbf{v} \tag{6.40}$$

We consider the situation under relaxation time approximation. For the case of a 3D anisotropic parabolic band valley, we illustrate the T-point valence band valley of bulk bismuth [90], as shown in Figure 6.1.
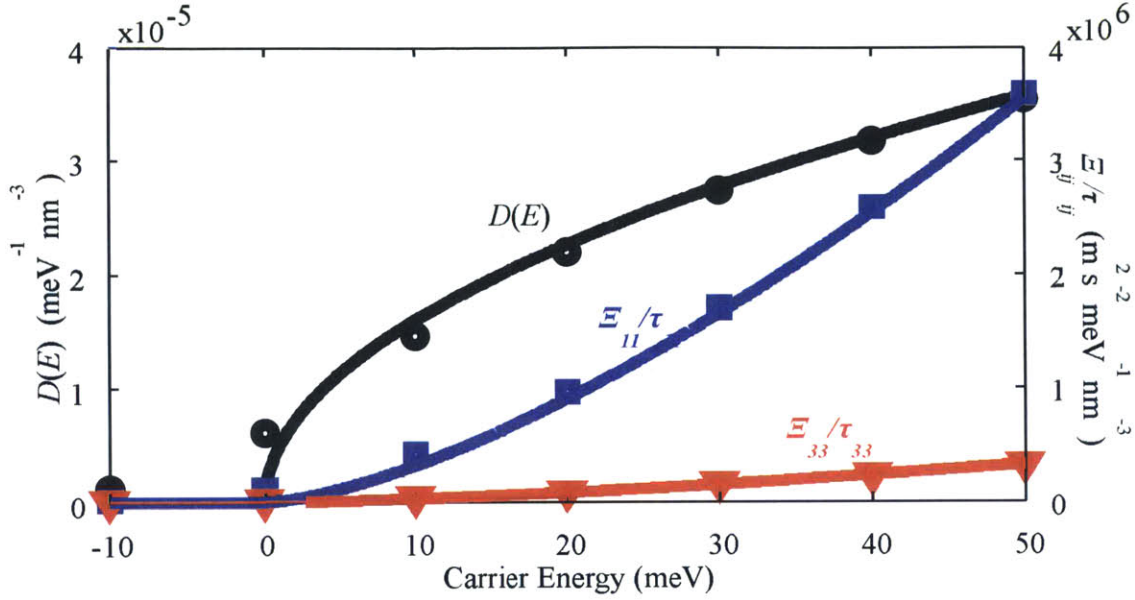
Figure 6.1: Comparison between the density of states (black), principal components of transport distribution tensor (blue and red), calculated from the analytical method developed in this chapter (solid lines) and the numerical method used in previous literatures (dots). The valence band valley at the T point of bulk bismuth is illustrated as an example. The principal effective masses used for calculations are $m_1 = m_2 = 0.059 m_e$ and $m_3 = 0.634 m_e$ [90], where m_e is the free electron mass. The components of transport distribution tensor are normalized by corresponding components of the relaxation time tensor for generality. In the numerical integration, the Gaussian form of $\sigma^{-1} \tilde{\delta}(E / \sigma) = (1 / \sqrt{2\pi} \sigma) \exp(-E^2 / 2\sigma^2)$ [87-89] is used to be the quasi-delta function, and the smearing is set to be $k_B T$, where $T = 100$ K. The sampled k-space grid is evenly distributed in the k-space, and set to have a density of $(2.5 \times 10^6)^3 / m^3$.

We see that for both density of states and the components of transport distribution tensor, the results from our analytical method are consistent with the results from numerical methods used by previous literatures. Furthermore, the numerical method become less trustable when it is close to a band-edge, because the density of states and the transport distribution are broadened by the smeared quasi-delta function, which can barely capture the sudden change of density of states or

transport distribution at the band edge. However, the discontinuity of density of states and transport distribution at band edges is very essential for thermoelectrics and electronics [21]. Thus, we propose that we should use the analytical method as much as possible to increase the accuracy of thermoelectric modeling. For the case of a 3D anisotropic non-parabolic band valley and linear band valley, we illustrate the L-point electron valley of bulk PbTe [91] and the Dirac point of bulk $Bi_{0.96}Sb_{0.04}$ [76], respectively, as shown in Figure 6.2 (a) and (b).
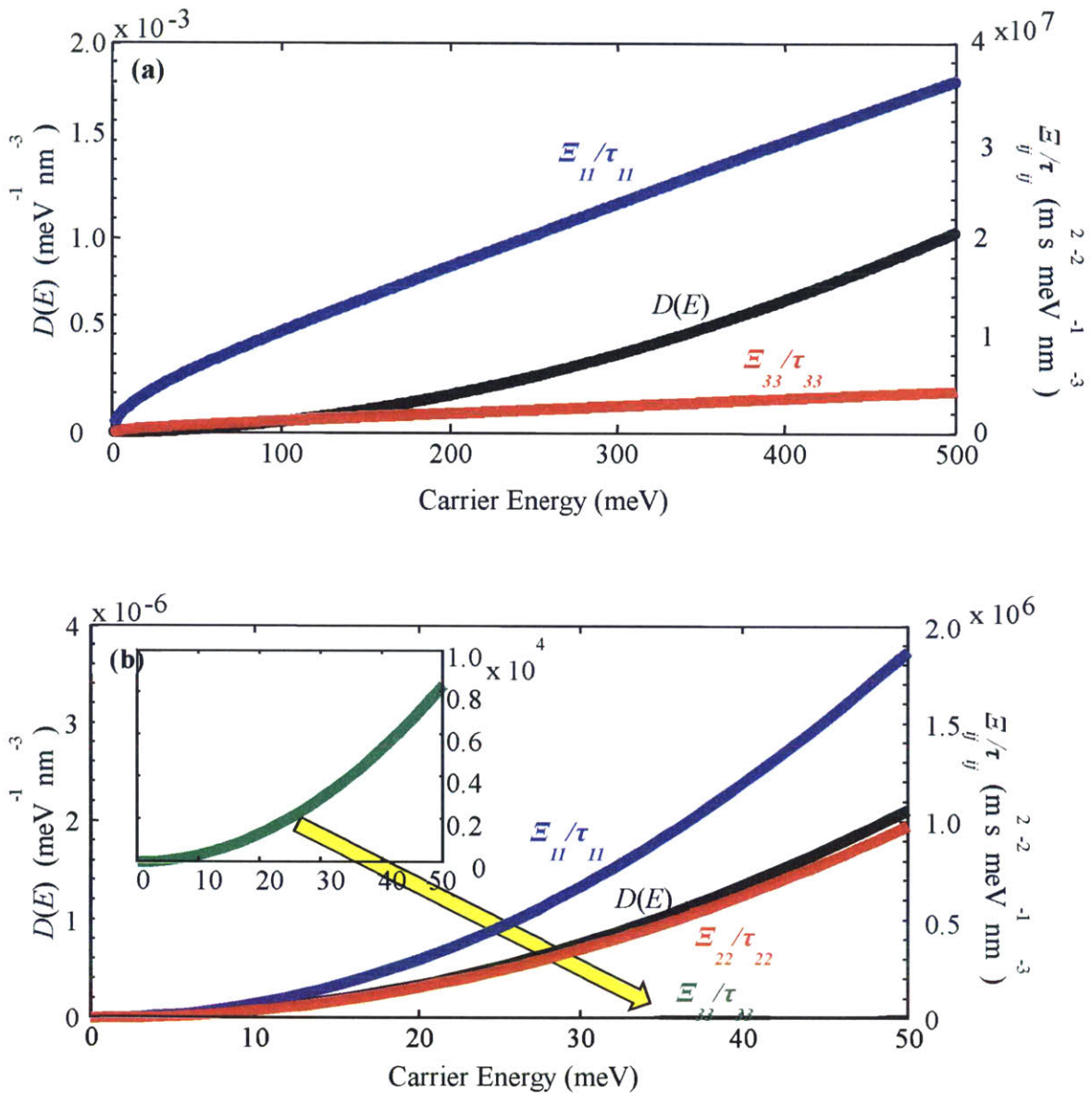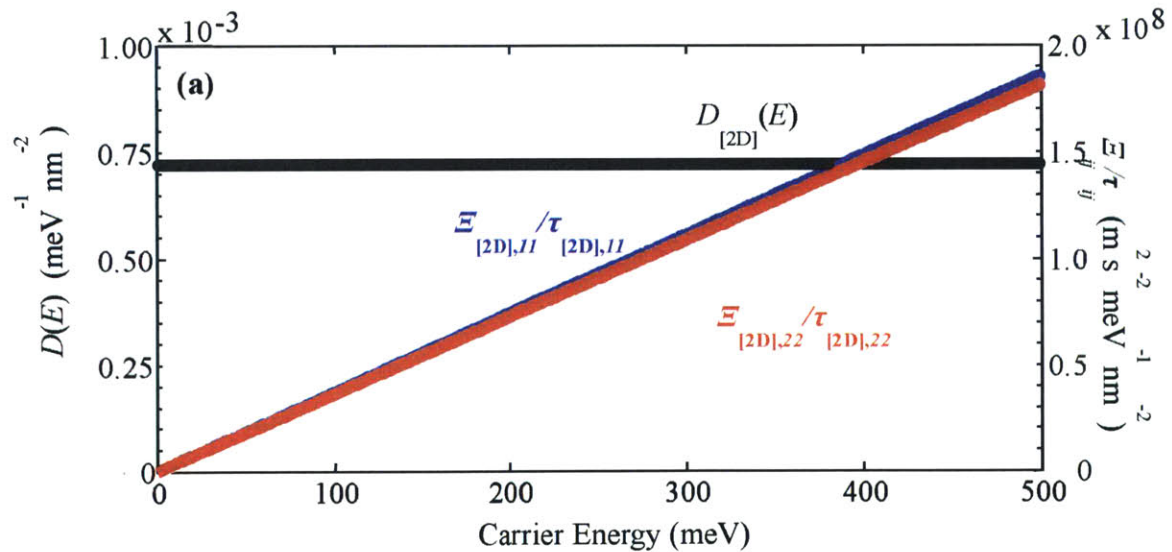
Figure 6.2: Density of states and principal components of transport distribution tensor of (a) the non-parabolic conduction band valley at the L point of bulk PbTe, and (b) the Dirac point in bulk Bi$_{0.96}$Sb$_{0.04}$. (a) The principal effective masses used for calculations are $m_1=m_2=0.06m_e$ and $m_3=0.505m_e$ [91], and the non-parabolic form $E + E^2 / E_g = \tilde{E}$ is used, where $E_g=189.7$ meV [91]. (b) The principal group velocities used for calculations are $v_1= 1.63\times10^6$ m/s, $v_2= 1.18\times10^6$ m/s and $v_3= 1.09\times10^5$ m/s [76].

For 2D materials, we illustrate the 2D parabolic conduction band valley at the K point of MoS$_2$ [92], as shown in Figure 6.3 (a). Researchers have studied anisotropic Dirac cones in graphene superlattice and in Bi$_{1-x}$Sb$_x$ thin films. We illustrate the anisotropic Dirac cone in graphene supperlattice studied in Ref. [93, 94], and the anisotropic Dirac cone in bisectrix oriented Bi$_{0.96}$Sb$_{0.04}$ thin film studied in Ref. [75, 76], as shown in Figure 6.3 (b) and (c), respectively.
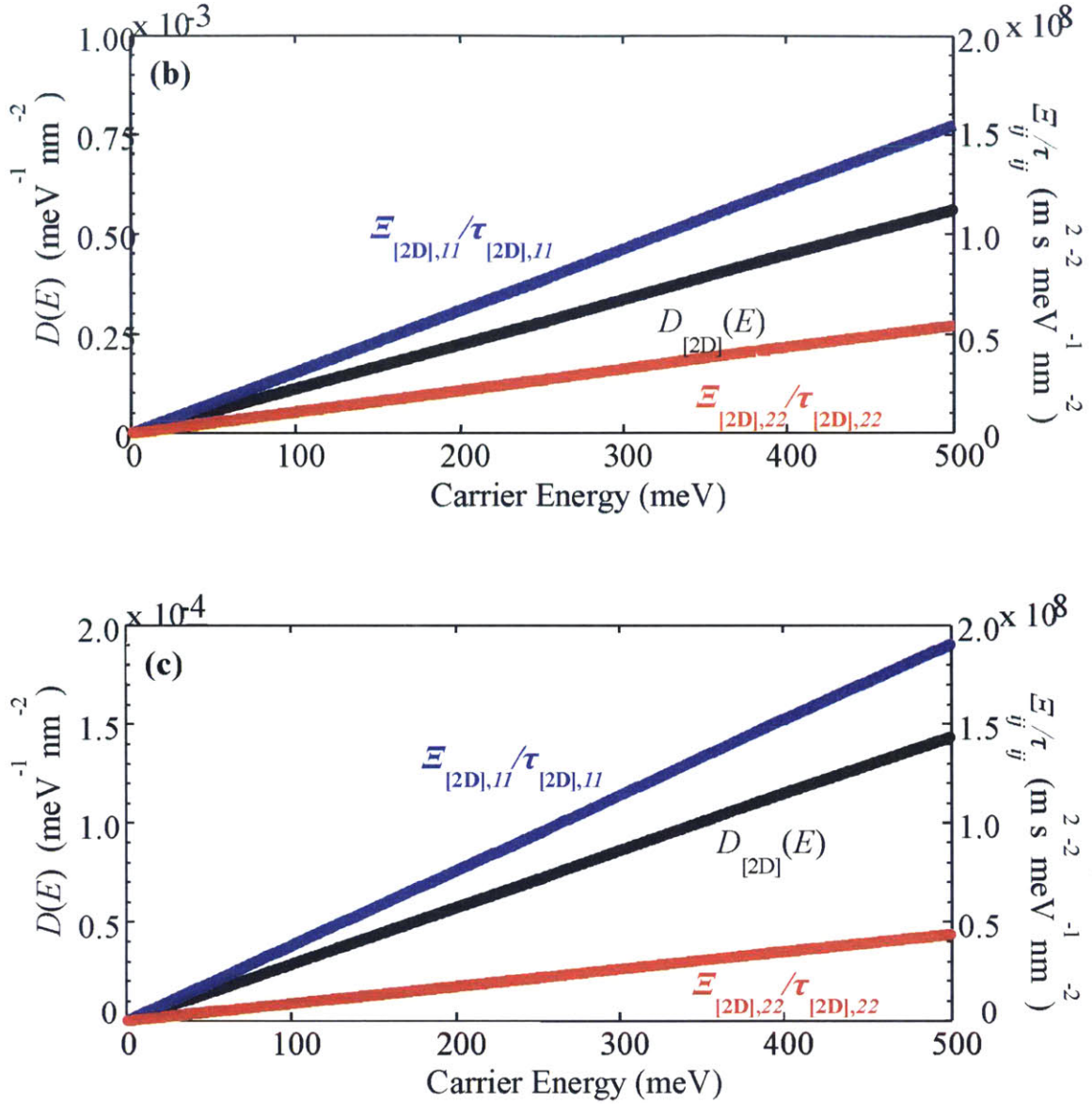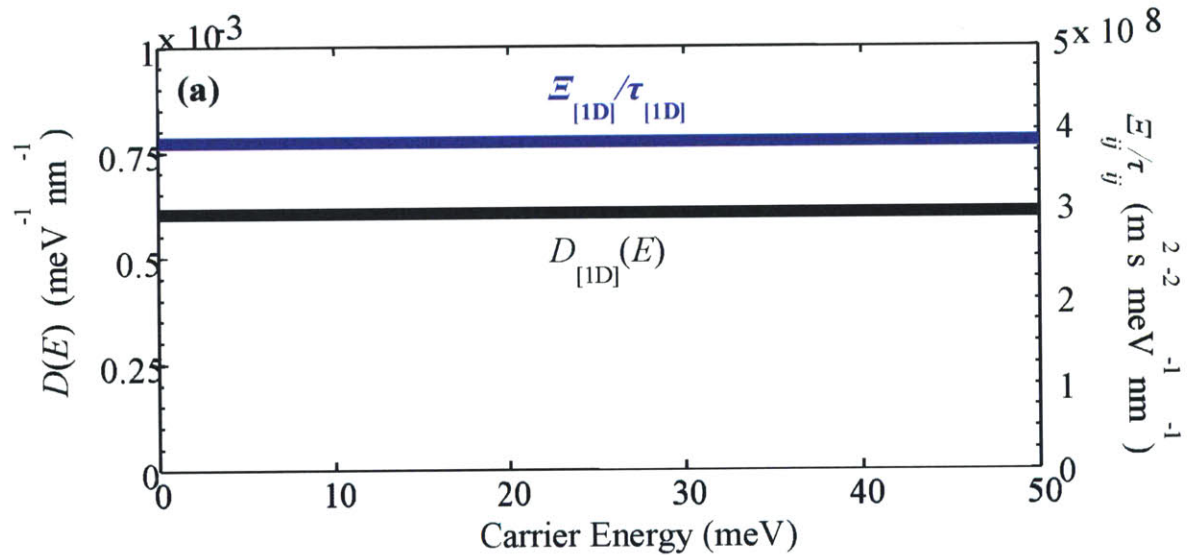
Figure 6.3: Density of states and principal components of transport distribution tensor for two-dimensional systems. (a) The parabolic conduction band valley at the K point of MoS_2 [92]. (b) The anisotropic Dirac cone in graphene supperlattice [93, 94]. (c) The anisotropic Dirac cone in bisectrix oriented $Bi_{0.96}Sb_{0.04}$ thin films [75, 76].

112

Lastly, we illustrate the single valley in carbon nanoribbon for 1D systems. For a semiconducting carbon nanoribbon, the band edge is parabolic with an effective mass. We illustrate the metallic armchar carbon nanoribbon with a width of 6.02 nm and Dirac fermion group velocity of 8×10^5 m/s [95, 96], as shown in Figure 6.4 (a), where the 1D density of states and the 1D transport distribution function remains a constant when the carrier energy is greater than zero. For a semiconducting carbon nanoribbon, there might form a 1D linear dispersion relation at the band edge, e.g. a metallic armchair nanoribbon with a width of 21 nm, a band gap of 0.65 eV and an effective mass of $0.05m_e$ [95, 97], as show in Figure 6.4(b). We noticed that for the semiconducting carbon nanoribbon, though the density of states diverges at the band edge, the transport distribution converges to 0, which is why the electrical conductivity is still finite.
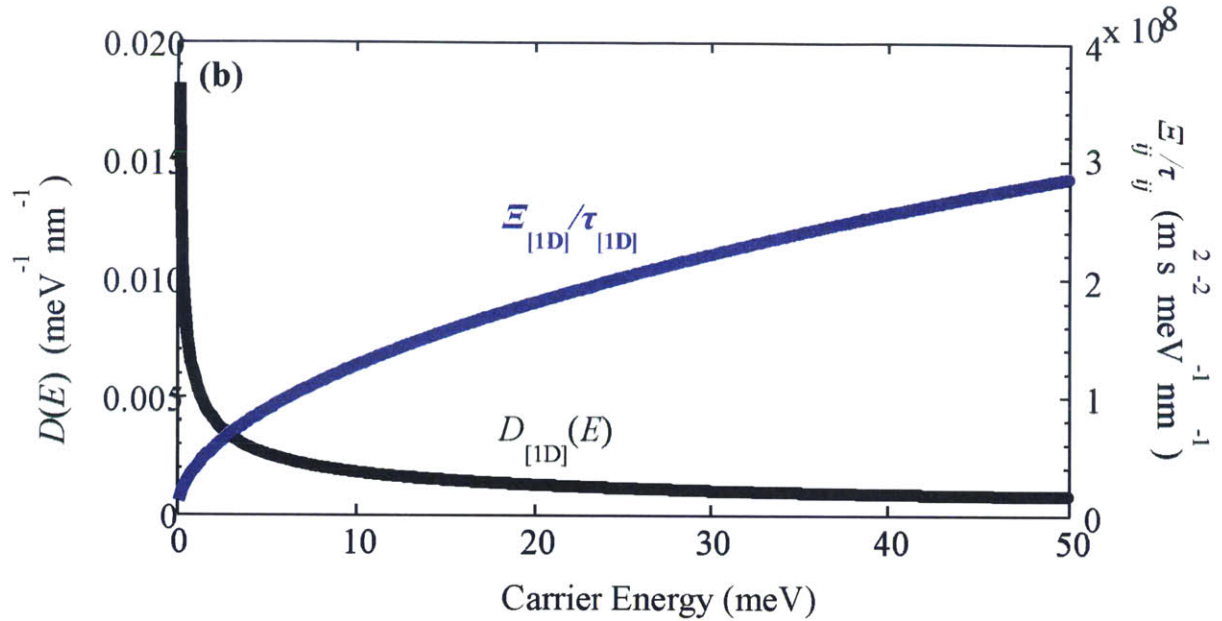
Figure 6.4: Density of states and principal components of transport distribution tensor for one-dimensional systems. (a) Metallic armchair carbon nanoribbon with a width of 6.02 nm and Dirac fermion group velocity of 8×10^5 m/s [95, 96]. (b) Semiconducting armchair nanoribbon with a width of 21 nm, a band gap of 0.65 eV and an effective mass of $0.05 m_e$ [95, 97].

6.7 Chapter Summary

In conclusion, we have derived the analytical forms of anisotropic transport distribution tensor for parabolic, non-parabolic, and linear valleys, in 3D, 2D and 1D materials systems, under both the relaxation time approximation and the mean free path approximation. We have found that the Onsager relation for electronic transport can be deviated, if the relaxation time tensor does not diagonalize in the same coordinates frame which diagonalizes the effective mass tensor. We then calculated the transport distribution function for some band valleys of several interesting materials systems, including the T-point hole valley of bulk bismuth, the L-point electron valley of bulk PbTe, the anisotropic Dirac point in bulk $Bi_{0.96}Sb_{0.04}$, the K point electron valley of

MoS$_2$, the anisotropic Dirac cones in graphene superlattice and Bi$_{1-x}$Sb$_x$ thin films, and also the single valley in semiconducting and metallic carbon nanoribbons [28].

Chapter 7

Suggestions for Future Directions

There are several directions opened for future research interests based on the work described in this thesis.

For high temperature waste heat recovery applications, this thesis has discussed the new direction of thermoelectrical power generation. Traditional thoughts have been concentrated on pursuing high thermoelectric ZT in narrow-gap materials, while here we see that wide-gap materials can also be promising. First, through the pseudo-ZT framework of thermoelectrics proposed here, we can see cases where the band gap will increase the maximum zt_e and maximum zt_L at the same time. Second, in wide-gap materials the Seebeck coefficient is usually larger than that for narrow-gap materials, because the positive entropy carried by the holes and the negative entropy carried by the electrons do not cancel each other in a notable way. This is especially important for high temperature waste heat recovery, because the power density is a very crucial parameter in engineering practice for thermoelectricity generating devices to be compatible with industrial thermal processes. The challenge of thermoelectrics of wide gap materials lies in: 1) how to change the Fermi level through doping and 2) how to reduce the lattice thermal conductivity. The proposed approaches will be using nanostructures, amorphous structures and polycrystals to build up a network of amorphous grain boundaries, which can scatter the phonons effectively without jeopardizing the electronic transport notably.

For low temperature thermoelectric cooling, this thesis has suggested the approach of trying to find materials with higher asymmetry for carrier scatterings between electrons and holes. Meanwhile, a divide-and-conquer strategy is proposed to change the scattering mechanism(s) and the materials dimensions based on the magnitude of the geometrically normalized lattice thermal conductivity. This thesis has also provided a tool to infer the specific

scattering mechanism(s) within a certain materials system, as well as a method on how to increase the possible maximum Seebeck coefficient by changing the carrier scattering order. The most relatively efficient thermoelectric cooling materials that have been found so far are narrow-gap materials. Based on the new model for nanostructured narrow-gap materials provided by this thesis, the materials search and design task will be accelerated. In future research, detailed first principle calculations can be carried out to study the band structures and the carrier scattering mechanism(s), in order to search for high performance thermoelectric cooling materials.

With the miniaturization trend of electronic devices, conventional research based on classical physics is no longer suitable and advanced quantum mechanics must be employed. Along this line, relativistic-effect devices provide feasible approach to largely advance a wide range of applications in information technology and energy fields, aiming ultra-high running speed and frequency, and ultra-low energy consumption. Such devices can be based on materials where the carriers' energy-momentum relation is not classic, but relativistic. This materials class includes graphene, topological insulators, and certain $Bi_{1-x}Sb_x$, which exhibit linear energy-momentum relations (Dirac cones) and lead to massless carriers. This materials class also includes phosphorene, MoS_2, and WS_2, where the carriers have non-zero masses.

An interesting future direction will be the study of novel transport phenomena based on such relativistic-effect materials for the next IT revolution. This thesis provided both the systematic method of constructing various conventional and unconventional anisotropic Dirac cones, and the method of detecting Dirac carrier scattering mechanisms by the maximum values of the Seebeck coefficient. It will be interesting to study the quantum transport of massive relativistic particles using MoS_2, WS_2 and phosphorene, and massless relativistic particles using graphene, topological insulators and $Bi_{1-x}Sb_x$. Such novel quantum transport studies of energy, entropy and charge may pave the way for the next-generation energetic, electronic and photonic devices. Further, the traditional study of relativistic particles is mainly limited to isotropic Dirac cones. The work on anisotropic Dirac cones, anisotropic transport and quantum effect in this thesis enables the future study of highly anisotropic novel transport to potentially attract significant attention. In addition, the transition of charge, energy, mass and entropy from the photon-like to the golf-ball-like regime is attractive for developing novel devices.

Bibliography

[1]   US Department of Energy Report 2007
[2]   US Energy Information Administration Report 2010
[3]   D. M. Rowe, Renewable energy 16 (1999) 1251.
[4]   S. B. Riffat and X. Ma, Applied Thermal Engineering 23 (2003) 913.
[5]   C. J. Vineis, A. Shakouri, A. Majumdar, and M. G. Kanatzidis, Advanced Materials 22 (2010) 3970.
[6]   K. Biswas, J. He, I. D. Blum, C.-I. Wu, T. P. Hogan, D. N. Seidman, V. P. Dravid, and M. G. Kanatzidis, Nature 489 (2012) 414.
[7]   C. B. Vining, Nature Materials 8 (2009) 83.
[8]   M. G. Kanatzidis, Chemistry of Materials 22 (2009) 648.
[9]   T. M. Tritt, H. Böttner, and L. Chen, MRS Bulletin 33 (2008) 366.
[10]   T. M. Tritt, Science 272 (1996) 1276.
[11]   C. Uher, Semiconductors and semimetals 69 (2001) 139.
[12]   D. Rowe, Applied Energy 40 (1991) 241.
[13]   P. Pichanusakorn and P. Bandaru, Materials Science and Engineering: R: Reports 67 (2010) 19.
[14]   G. Mahan, Journal of Applied Physics 65 (1989) 1578.
[15]   D. J. Bergman and L. G. Fel, Journal of Applied Physics 85 (1999) 8205.
[16]   G. G. Nestorova and E. J. Guilbeau, Lab on a Chip 11 (2011) 1761.
[17]   H. J. Goldsmid, Introduction to thermoelectricity, Springer, 2009.
[18]   L. Hicks and M. Dresselhaus, Physical Review B 47 (1993) 12727.
[19]   A. Minnich, M. Dresselhaus, Z. Ren, and G. Chen, Energy & Environmental Science 2 (2009) 466.
[20]   L. Hicks and M. Dresselhaus, Physical Review B 47 (1993) 16631.
[21]   G. Mahan and J. Sofo, Proceedings of the National Academy of Sciences 93 (1996) 7436.
[22]   Y. Lin and M. Dresselhaus, Physical Review B 68 (2003) 75304.
[23]   J. P. Heremans, V. Jovovic, E. S. Toberer, A. Saramat, K. Kurosaki, A. Charoenphakdee, S. Yamanaka, and G. J. Snyder, Science 321 (2008) 554.
[24]   C.-H. Park, L. Yang, Y.-W. Son, M. L. Cohen, and S. G. Louie, Physical Review Letters 101 (2008) 126804.
[25]   N. W. Ashcroft and N. D. Mermin, Solid state physics, Saunders College, 1976.
[26]   http://thermoelectrics.matsci.northwestern.edu/thermoelectrics/index.html
[27]   S. Tang and M. Dresselhaus, arXiv preprint arXiv:1406.1842 (2014)
[28]   S. Tang and M. S. Dresselhaus, Applied Physics Letters 105 (2014) 033907.

[29] K. Dolui, I. Rungger, C. D. Pemmaraju, and S. Sanvito, Physical Review B 88 (2013) 075420.

[30] M. S. Fuhrer and J. Hone, Nature Nanotechnology 8 (2013) 146.

[31] X. Gu and R. Yang, Applied Physics Letters 105 (2014) 131903.

[32] Y. Ding, Y. Wang, J. Ni, L. Shi, S. Shi, and W. Tang, Physica B: Condensed Matter 406 (2011) 2254.

[33] W. Zhang, Z. Huang, W. Zhang, and Y. Li, Nano Research 7 (2014) 1731.

[34] L. Liu, S. Bala Kumar, Y. Ouyang, and J. Guo, IEEE Transactions on Electron Devices 58 (2011) 3042.

[35] A. Kumar and P. Ahluwalia, The European Physical Journal B-Condensed Matter and Complex Systems 85 (2012) 1.

[36] R. K. Ghosh and S. Mahapatra, IEEE Journal of the Electron Devices Society 1 (2013) 175.

[37] N. Peimyoo, J. Shang, W. Yang, Y. Wang, C. Cong, and T. Yu, Nano Research 8 (2015) 1210.

[38] A. Molina-Sanchez and L. Wirtz, Physical Review B 84 (2011) 155413.

[39] Y. Cai, J. Lan, G. Zhang, and Y.-W. Zhang, Physical Review B 89 (2014) 035438.

[40] J.-Y. Kim, S. M. Choi, W.-S. Seo, and W.-S. Cho, Bull. Korean Chem. Soc 31 (2010) 3225.

[41] R. Yan, J. R. Simpson, S. Bertolazzi, J. Brivio, M. Watson, X. Wu, A. Kis, T. Luo, A. R. Hight Walker, and H. G. Xing, ACS Nano 8 (2014) 986.

[42] S. Aminorroaya-Yamini, C. Zhang, X. Wang, and I. Nevirkovets, Journal of Physics D: Applied Physics 45 (2012) 125301.

[43] B. Y. Yavorsky, N. Hinsche, I. Mertig, and P. Zahn, Physical Review B 84 (2011) 165208.

[44] S. Lepkowski, I. Gorczyca, K. Stefanska-Skrobas, N. Christensen, and A. Svane, Physical Review B 88 (2013) 81202.

[45] S. M. Thahab, ed., Characterization Parameters of (InGaN/InGaN) and (InGaN/GaN) Quantum Well Laser Diode, Semiconductor Laser Diode Technology and Applications, Intechopen, 2012.

[46] M. Farahmand, C. Garetto, E. Bellotti, K. F. Brennan, M. Goano, E. Ghillino, G. Ghione, J. D. Albrecht, and P. P. Ruden, IEEE Transactions on Electron Devices 48 (2001) 535.

[47] C. Guthy, C.-Y. Nam, and J. E. Fischer, Journal of Applied Physics 103 (2008) 064319.

[48] M. Lundstrom, Fundamentals of carrier transport, Cambridge University Press, 2009.

[49] Y. I. Ravich, B. Efimova, and V. Tamarchenko, Physica Status Solidi (b) 43 (1971) 11.

[50] J. Singh, Physics of Semiconductors and their Heterostructures, McGraw-Hill New York, 1993.

[51] D. Rode, Physical Review B 2 (1970) 1012.

[52] D. Oberli, D. Wake, M. Klein, J. Klem, T. Henderson, and H. Morkoc, Physical Review Letters 59 (1987) 696.

[53] S. Tang and M. S. Dresselhaus, arXiv preprint arXiv:1410.4907 (2014)

[54] K. S. Novoselov, A. K. Geim, S. Morozov, D. Jiang, Y. Zhang, S. Dubonos, I. Grigorieva, and A. Firsov, Science 306 (2004) 666.

[55] K. S. Novoselov, A. K. Geim, S. V. Morozov, D. Jiang, M. I. Katsnelson, I. V. Grigorieva, S. V. Dubonos, and A. A. Firsov, Nature 438 (2005) 197.

[56] Y. M. Zuev, W. Chang, and P. Kim, Physical Review Letters 102 (2009) 096807.

[57] A. D. Liao, J. Z. Wu, X. Wang, K. Tahy, D. Jena, H. Dai, and E. Pop, Physical Review Letters 106 (2011) 256801.

[58] H. Goldsmid, British Journal of Applied Physics 14 (1963) 271.

[59] H. Goldsmid, Physica Status Solidi (a) 1 (1970) 7.

[60] S. Golin, Physics Review 176 (1968) 830.

[61] S. Golin, Physics Review 166 (1968) 643.

[62] X. Gonze, J.-P. Michenaud, and J.-P. Vigneron, Physical Review B 41 (1990) 11827.

[63] B. Lax and J. G. Mavroides, Solid State Physics, Academic Press, New York, 1960.

[64] B. Lax, J. G. Mavroides, H. J. Zeiger, and R. J. Keyes, Physical Review Letters 5 (1960) 241.

[65] O. Rabin, Vol. PhD, Massachusettes Institute of Technology, 2004.

[66] O. Rabin, Y. Lin, and M. Dresselhaus, Applied Physics Letters 79 (2001) 81.

[67] E. E. Mendez, Vol. PhD, Massachusetts Institute of Technology, 1979.

[68] E. E. Mendez, A. Misu, and M. S. Dresselhaus, Physical Review B 24 (1981) 639.

[69] S. Tang and M. S. Dresselhaus, Physical Review B 86 (2012) 075436.

[70] S. Tang and M. S. Dresselhaus, Physical Review B 89 (2014) 045424.

[71] S. Tang and M. S. Dresselhaus, Journal of Materials Chemistry C 2 (2014) 4710.

[72] D. Morelli, D. Partin, and J. Heremans, Semiconductor Science and Technology 5 (1990) S257.

[73] L. Fu, C. L. Kane, and E. J. Mele, Physical Review Letters 98 (2007) 106803.

[74] B. Buttner, C. X. Liu, G. Tkachov, E. G. Novik, C. Brune, H. Buhmann, E. M. Hankiewicz, P. Recher, B. Trauzettel, S. C. Zhang, and L. W. Molenkamp, Nature Physics 7 (2011) 418.

[75] S. Tang and M. S. Dresselhaus, Nanoscale 4 (2012) 7786.

[76] S. Tang and M. S. Dresselhaus, Nano Letters 12 (2012) 2021.

[77] T. Scheidemantel, C. Ambrosch-Draxl, T. Thonhauser, J. Badding, and J. Sofo, Physical Review B 68 (2003)

[78] S. Lee and P. von Allmen, Applied Physics Letters 88 (2006) 022107.

[79] B. Y. Yavorsky, N. Hinsche, I. Mertig, and P. Zahn, Physical Review B 84 (2011) 165208.

[80] T. Teramoto, T. Komine, M. Kuraishi, R. Sugita, Y. Hasegawa, and H. Nakamura, Journal of Applied Physics 103 (2008) 043717.

[81] T. Teramoto, T. Komine, S. Yamamoto, M. Kuraishi, R. Sugita, Y. Hasegawa, and H. Nakamura, Journal of Applied Physics 104 (2008) 053714.

[82] W. Bies, R. Radtke, H. Ehrenreich, and E. Runge, Physical Review B 65 (2002) 085208.

[83] B. Lax and J. G. Mavroides, eds., Solid State Physics, Vol. 11, Academic Press, New York, 1960.

[84] C. Truesdell, Rational Thermoelectrics: A Course of Lectures on Selected Topics, McGraw-Hill, New York, 1969.

[85] V. Sandomirskii, Soviet Journal of Experimental and Theoretical Physics 25 (1967) 101.

[86] E. Rogacheva, S. Grigorov, O. Nashchekina, S. Lyubchenko, and M. Dresselhaus, Applied Physics Letters 82 (2003) 2628.

[87] C.-L. Fu and K.-M. Ho, Physical Review B 28 (1983) 5480.

[88] R. J. Needs, R. M. Martin, and O. H. Nielsen, Physical Review B 33 (1986) 3778.

[89] N. Mazari, in Cavendish Laboratory, Vol. PhD, University of Camridge, Cambridge, 1996.

[90] R. J. Dinger and A. W. Lawson, Physical Review B 7 (1973) 5215.

[91] S. Yuan, G. Springholz, G. Bauer, and M. Kriechbaum, Physical Review B 49 (1994) 5476.

[92] T. Cheiwchanchamnangij and W. R. Lambrecht, Physical Review B 85 (2012) 205302.

[93] C.-H. Park, L. Yang, Y.-W. Son, M. L. Cohen, and S. G. Louie, Nature Physics 4 (2008) 213.

[94] S. Rusponi, M. Papagno, P. Moras, S. Vlaic, M. Etzkorn, P. M. Sheverdyaeva, D. Pacil, H. Brune, and C. Carbone, Physical Review Letters 105 (2010) 246803.

[95] H. Raza and E. C. Kan, Physical Review B 77 (2008) 245434.

[96] A. Naeemi and J. D. Meindl, in Interconnect Technology Conference, 2008. IITC 2008. International, IEEE, 2008, p. 183.

[97] G. Liang, N. Neophytou, D. E. Nikonov, and M. S. Lundstrom, IEEE Transactions on Electron Devices 54 (2007) 677.